Computer modeling of oxygen migration in $HgBa_2CuO_{4+\delta}$

N. V. Moseev

Institute of Metal Physics, Russian Academy of Sciences, Ekaterinburg
(Submitted January 29, 1999)
Pis'ma Zh. Tekh. Fiz. **25**, 1–4 (August 12, 1999)

A molecular statics method is used to calculate the energy barriers for the migration of oxygen ions. Vacancy and interstitial diffusion mechanisms are considered. The lowest migration barrier is obtained for the vacancy mechanism. © *1999 American Institute of Physics.*
[S1063-7850(99)00108-1]

Superconducting compounds having the composition $HgBa_2Ca_{n-1}Cu_nO_{2n+2+\delta}$ ($n=1,2,3$) have a high superconducting transition temperature and a comparatively simple crystal structure (P4/mmm space group). They are therefore convenient objects for studying the relationship between superconducting and structural (defect) properties. Experimental investigations of the structure of these compounds have shown that the superconductivity appears as a result of the formation of interstitial oxygen ions. It was established in diffraction experiments that interstitial oxygen ions are located at positions [1/2 1/2 0] (in the center of the plane formed by the Hg ions).[1,2] In addition, defects consisting of substitutions of Hg ions by Cu ions and interstitial oxygen ions in positions [1/2 0 0] (between Hg or Cu ions) were also observed experimentally.[1,2]

Computer modeling has been used for theoretical calculations of the energy and structural properties of these defects.[3,4] However, very few studies have been made of the diffusion properties of oxygen. We are not aware of any experimental investigations of oxygen diffusion in these oxides. Islam and Winch[3] only calculated the energy barriers for two possible paths of oxygen ion migration in $HgBa_2Ca_2Cu_3O_{8+\delta}$. The aim of the present study was to investigate all possible paths of oxygen ion migration to determine the most probable diffusion mechanism.

The oxide $HgBa_2CuO_{4+\delta}$ was selected for the calculations which were made using the MOLSTAT computer program[5] in which the molecular statics method is used to calculate the properties of defects in ionic crystals. The migration energy was defined as the difference between the energies of a defect at the saddle point and the equilibrium position. The parameters of the ion–ion interaction potentials were taken from Ref. 3. By using these potentials we accurately reproduced the experimentally determined[6] structure of $HgBa_2CuO_{4+\delta}$: after relaxation of the model crystallite, the ion coordinates of the unit cell corresponded to those determined experimentally.

The crystal structure of $HgBa_2CuO_{4+\delta}$ is shown in Fig. 1. The unit cell is tetragonal and contains two nonequivalent oxygen ion positions: O1 and O2. Also shown in the figure are the experimentally determined positions of the interstitial oxygen ions O3 and O4. We first investigated the vacancy diffusion mechanism. We calculated the energy barriers for the migration of oxygen ions between the nearest positions O1–O1, O2–O2, and O1–O2. The results of the calculations are given in the first four columns of Table I. It can be seen that for the vacancy diffusion mechanism, the minimum energy barrier exists for the migration of an oxygen ion in the Cu–O1 plane. We then studied the interstitial diffusion mechanism. We determined the energy barriers for hopping of O3 and O4 interstitial ions between nearest positions. The calculated migration energies are given in the fifth and sixth columns of the table. Note that the minimum barrier for migration by the interstitial mechanism was higher than the minimum migration barrier for the vacancy mechanism. We also studied how the substitution of Hg by Cu influenced the

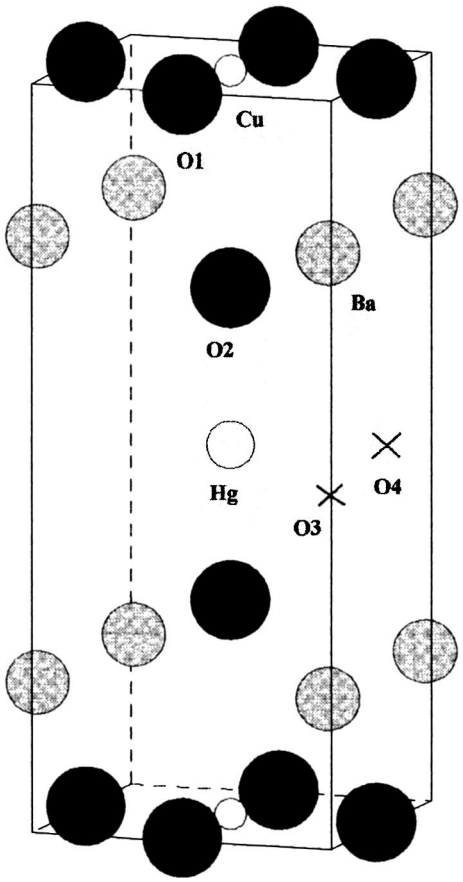

FIG. 1. Structure of $HgBa_2CuO_{4+\delta}$.

TABLE I. Migration energies of oxygen ions in $HgBa_2CuO_{4+\delta}$.

Migration path	Vacancy O1–O1	Vacancy O2–O2	Vacancy O1–O2	Vacancy O2–O1	Interstitial ion O3–O3	Interstitial ion O4–O4	O3–O3 Cu→Hg	O4–O4 Cu→Hg
E_M, eV	0.3	1.4	3.2	1.4	3.0	0.9	2.4	1.8

migration energy of the interstitial ions. For this purpose a single Hg ion was substituted by a Cu ion and the migration barriers for O3 and O4 were calculated near this substitution. The results are given in the last two columns of the table. It was found that a substitutional defect reduces the migration energy of the interstitial O3 ion and increases that of the interstitial O4 ion.

An analysis of the data given in Table I shows that the lowest barrier is obtained for vacancy migration in the Cu–O1 plane. Thus, from the energy point of view, the vacancy mechanism of oxygen diffusion is the most probable in the oxide $HgBa_2CuO_{4+\delta}$. This result differs from the results of calculating the migration properties of oxygen ions in $HgBa_2Ca_2Cu_3O_{8+\delta}$ (Ref. 3). Islam and Winch[3] calculated the energy barriers for oxygen ion migration by the vacancy mechanism in the Cu–O plane and by the interstitial mechanism in the Hg plane. The energy barrier for the interstitial diffusion mechanism $E_M = 0.68$ eV was found to be the lowest. In our calculations for the migration of a similar interstitial ion the barrier was found to be ~ 3 eV. The reason for this difference is unclear since we used the ion–ion interaction potentials from Ref. 3. However, the theoretical calculations showed that the vacancy mechanism of oxygen diffusion is energetically favorable in La_2CuO_4 (Refs. 7 and 8), $YBa_2Cu_3O_7$ (Refs. 9 and 10), $Bi_2Si_2CaCu_2O_8$ (Ref. 11), and $Tl_2Ba_2CaCu_2O_8$ (Ref. 12). This property may well be a common feature of all superconducting oxides containing Cu–O planes.

[1] O. Chmaissem, Q. Huang, S. N. Putilin *et al.*, Physica C **212**, 259 (1993).
[2] J. L. Wagner, B. A. Hunter, D. G. Hinks *et al.*, Phys. Rev. B **51**, 15 407 (1995).
[3] M. S. Islam and L. J. Winch, Phys. Rev. B **52**, 10 510 (1995).
[4] X. Zhang, S. Y. Xu, and C. K. Ong, Physica C **262**, 13 (1996).
[5] J. L. Gavartin, C. R. A. Catlow, A. L. Shluger *et al.*, Modell. Simul. Mater. Sci. Eng. **1**, 29 (1992).
[6] V. L. Aksenov, A. M. Balagurov, V. V. Sikolenko *et al.*, Phys. Rev. B **55**, 3966 (1997).
[7] N. L. Allan and W. C. Mackrodt, Philos. Mag. A **64**, 1129 (1991).
[8] N. V. Moseev, Sverkhprovodimost' **7**, 22 (1994).
[9] M. S. Islam, Supercond. Sci. Technol. **3**, 531 (1990).
[10] N. V. Moseev, A. N. Varaksin, and B. N. Goshchitskiĭ, *Abstracts of papers presented at Third All-Union Conference on High-Temperature Superconductors*, Kharkov, 1991 [in Russian], FTINT AN USSR, p. 51.
[11] N. V. Moseev, Fiz. Tverd. Tela (St. Petersburg) **37**, 2987 (1995) [Phys. Solid State **37**, 1646 (1995)].
[12] N. V. Moseev, Modell. Simul. Mater. Sci. Eng. **6**, 1 (1998).

Translated by R. M. Durham

Catalytic plasma anodization of single-crystal 6H–SiC structures

A. P. Bibilashvili, A. B. Gerasimov, R. É. Kazarov, and Z. D. Samadashvili

Javakhishvili State University, Tbilisi
(Submitted March 19, 1999)
Pis'ma Zh. Tekh. Fiz. **25**, 5–7 (August 12, 1999)

The use of catalytic plasma anodization to obtain oxides on the surface of SiC is an original method, hitherto unused. This method can significantly reduce the process temperature, increase the oxide growth rate, and improve the properties of the structures, giving a low density of surface states and a small fixed charge in the oxide. © *1999 American Institute of Physics.* [S1063-7850(99)00208-6]

An important requirement for the widespread application of SiC in high-temperature electronics, optoelectronics, and the manufacture of radiation-resistant devices is the development of a relatively simple technology, with a low process temperature and high growth rate of high-quality oxide.

The high-temperature thermal oxidation in ''dry'' and ''wet'' oxygen atmospheres used to fabricate SiC devices and integrated circuits is characterized by a very low oxide growth rate.[1,2] The use of plasma-chemical deposition of SiO_2 on SiC followed by thermal annealing in various gases was recently reported.[3] The deposition temperature was maintained at 473 K and the oxide growth rate was 18 Å/min, which is fifteen times higher than that reported in Refs. 1 and 2.

In the present paper we report results of an alternative process for obtaining SiO_2 oxide films by catalytic plasma anodization on 6H–SiC crystal structures.

The substrates were (100)-oriented single-crystal *n*-SiC of polytype 6H having the concentrations $N_d - N_a \sim 10^{18}\,\mathrm{cm}^{-3}$. The catalyst for the plasma anodizing process is a layer of yttrium deposited by an electron-beam method on the chemically pure SiC surface.

The plasma anodizing process was accomplished by applying a positive potential to the Y–SiC structures relative to the plasma. The anodizing temperature was 573 K, the forming current density was constant, and the increase in the voltage drop at the growing oxide film indicated an increase in its thickness. It was observed experimentally that the voltage increases linearly with time, and the oxide growth rate depends on the forming current density. This indicates that the migration of negative oxygen ions and plasma electrons plays a decisive role in the oxidation mechanism. The oxide growth rate at a forming current density of $30\,\mathrm{mA/cm}^2$ was ~42 Å/min, which is 2.5 times higher than that obtained in Ref. 3.

After the plasma anodizing process had been completed, the Y_2O_3 oxide was removed chemically without damaging the surface of the SiO_2 oxide.

In order to fabricate an MIS structure on the SiO_2 surface, Al was deposited by a vacuum resistive method in the form of 1.2 mm diameter dots.

Figure 1 gives the normalized capacitance–voltage characteristics of the Al–SiO_2–SiC structures before and after annealing. The structures were annealed in a nitrogen atmosphere at 623 K for 30 min. It can be seen that after thermal annealing the flat-band voltage and the fixed charge in the oxide were lower. The disappearance of the hysteresis indicates that the concentration of mobile ions in the oxide is reduced sharply. Estimates showed that the fixed charge density in the oxide was $Q_0 \approx 1.4\times10^{12}\,\mathrm{cm}^{-2}$ before annealing and $Q_0' \approx 4.2\times10^{11}\,\mathrm{cm}^{-2}$ after annealing, and the density of surface states was $N_{ss} \approx 2\times10^{11}\,\mathrm{cm}^{-2}\cdot\mathrm{eV}^{-1}$ in both cases.

The presence of a catalyst in the anodizing process sharply increases the growth rate of the SiO_2, lowers its formation temperature, and protects against radiation damage and contamination from the plasma, which makes this process simpler and more economical compared with other known methods of forming oxides.[1–3]

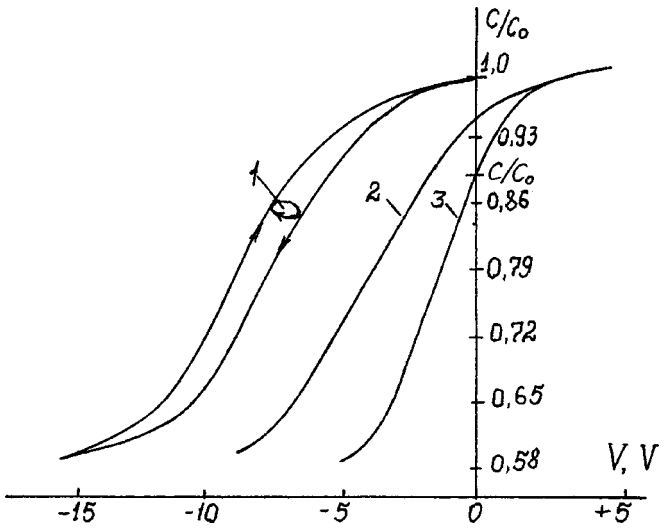

FIG. 1. Normalized capacitance–voltage characteristics of Al–SiO_2–SiC structures before (*1*) and after (*2*) thermal annealing; *3* — theoretical characteristic; C/C_0 is the normalized capacitance for the flat bands.

[1] D. M. Brown and G. Cati, in *Transactions of the Second International High Temperature Electronics Conference*, Vol. 1, 1994, pp. XI-17–XI-20.
[2] J. W. Palmour, R. F. Davis, H. S. Kong, S. F. Corcoran, and D. P. Griffis, J. Electrochem. Soc. **136**, 502 (1989).
[3] A. Golz, S. Gros, R. Janssen, E. Stein von Kamienski, and H. Kuzz, in *Proceeding of the Symposium on Frontiers in Electronics: High Temperature and Large Area Applications* Vol. 59, 1997, pp. 364–365.

Translated by R. M. Durham

Use of high-purity $Al_xGa_{1-x}As$ layers in epitaxial structures for high-power microwave field-effect transistors

K. S. Zhuravlev, A. I. Toropov, T. S. Shamirzaev, A. K. Bazarov, Yu. N. Rakov, and Yu. B. Myakishev

Institute of Semiconductor Physics, Siberian Branch of the Russian Academy of Sciences, Novosibirsk; Oktava Scientific Industrial Organization, Novosibirsk

(Submitted March 25, 1999)
Pis'ma Zh. Tekh. Fiz. **25**, 8–15 (August 12, 1999)

The fabrication of high-purity layers of $Al_xGa_{1-x}As$ solid solutions in the range $0 \leqslant x \leqslant 0.38$ by molecular beam epitaxy is reported. The low-temperature photoluminescence spectra of these layers reveal predominantly the free exciton recombination line (X). The narrow width of the X line, the high intensity ratio of this line to that of the band–acceptor transition line, and the linear dependence of the X line intensity on the excitation power density in the range between 1×10^{-4} and $100\ \mathrm{V \cdot cm^{-2}}$ indicate a low concentration of background impurities in these layers. Using this material in pseudomorphic AlGaAs/InGaAs/GaAs heterostructures for high-power microwave transistors produced devices with a specific saturated output power of 0.9 W/mm at 18 GHz. © *1999 American Institute of Physics.* [S1063-7850(99)00308-0]

The development of communications devices, electromagnetic weapons, radar, and other microwave devices incorporating high-power gallium arsenide microwave transistors requires improvements in the main characteristics of microwave transistors: the specific output power (P), the power gain (K), the efficiency, the specific slope of the current–voltage characteristics, and the operating frequency range.[1] The most important overall parameter of a transistor is its specific output power.[2] The specific output power achieved so far in domestic mass-produced Schottky-barrier microwave field-effect transistors using gallium arsenide structures is 0.5–0.6 W/mm at 18 GHz (Ref. 3). In order to increase the specific power of these transistors, it is necessary to increase both the source–drain current density (I_1) and the breakdown drain–gate voltage (U_2). However, we know that in the gallium arsenide structures with a uniformly doped channel now used for the commercial manufacture of microwave transistors, it is impossible to increase both U_2 and I_1 (Refs. 2 and 4). An analysis of published data showed that the highest current densities and breakdown voltages are obtained for transistors fabricated using pseudomorphic AlGaAs/InGaAs/GaAs heterostructures[5,6] in which the gate is positioned on the wide-gap material and the channel is a highly doped InGaAs ternary solution. The breakdown voltage U_2 in these structures is determined by the concentration of background impurities in AlGaAs and by the depth of the AlGaAs/InGaAs/GaAs quantum well.

In the present paper we report the preparation of high-purity layers of $Al_xGa_{1-x}As$ solid solutions containing AlAs in the range $0 \leqslant x \leqslant 0.38$. A low concentration of background impurities in the layers is indicated by the narrow widths of the exciton recombination lines, which are almost 1.5 times smaller than the lowest experimental values quoted in the literature[7,8] and are no greater than the values calculated theoretically assuming a random distribution of Ga and As atoms in the crystal lattice of the $Al_xGa_{1-x}As$ layers.[9] Another factor is the high intensity ratio of the exciton recombination line to that of the band–acceptor transition line. By using this high-purity material in pseudomorphic AlGaAs/InGaAs/GaAs heterostructures for high-power microwave transistors, it was possible to increase U_2 up to 25 V, which is 25% higher than the values obtained using AlGaAs doped to around $n = 1 \times 10^{16}\ \mathrm{cm^{-3}}$ and to fabricate transistors having a specific saturated output power $P = 0.9$ W/mm at 18 GHz, which is comparable with the power of similar foreign transistors.[10]

The layers being studied and the pseudomorphic AlGaAs/InGaAs/GaAs heterostructures for the microwave transistors were grown in a Riber 32P molecular beam epitaxy system with a three-inch substrate holder on semi-insulating GaAs(001) wafers. The sequence of layers in the structure is given in Table I. The initial materials were ultrapure arsenic containing $<10^{-5}$% (7N) residual impurities supplied by Furukawa Co. Ltd, ultrapure gallium containing $<10^{-6}$% (8N) residual impurities, and ultrapure indium containing $<10^{-5}$% (7N) residual impurities prepared at the IPTM of the Russian Academy of Sciences, and ultrapure aluminum containing $<10^{-4}$% (6N) residual impurities supplied by Vacuum Metallurgical Co. Ltd. After annealing the system at 200 °C for two weeks and cooling the cryopanels with liquid nitrogen, a residual gas pressure better than 10^{-11} Torr was achieved in the growth chamber when the molecular sources were in arc-sustaining regimes. These heterostructures were used to fabricate Schottky-barrier field-effect transistors with a gate length of 0.5 μm and a channel width of 180 and 300 μm. The microwave parameters of the transistors were measured using a Polyana probe system at frequencies of 12 and 17.7 GHz.

Figure 1 shows photoluminescence spectra of intentionally undoped GaAs and $Al_xGa_{1-x}As$ layers of different composition, measured at 4.2 K. The dominant line in the spectrum of the GaAs layer is the FX line, having its energy peak

TABLE I. Sequence of layers in a pseudomorphic AlGaAs/InGaAs/GaAs heterostructure for microwave transistors.

Layer	Thickness, nm
n^+ GaAs (Si : 6×10^{18} cm^{-3})	40
i GaAs	5
i-$Al_{0.38}Ga_{0.62}As$	30
$n^+In_{0.15}Ga_{0.85}As$ channel (Si : 2.8×10^{18} cm^{-3})	15
*i*GaAs	10
i-$Al_{0.38}Ga_{0.62}As$	100
i GaAs	100
CP $(AlAs)_5(GaAs)_{10}\times20$	
i GaAs	300
AGChP-10 (100) substrate	

at 1.5151 eV, which is ascribed to the recombination of free excitons.[11] A band–acceptor (e, A) recombination line between levels of the shallow background carbon acceptor is also observed. The intensity of the (e, A) line is thirty times lower than that of the FX line.

The spectra of the $Al_xGa_{1-x}As$ solid solutions reveal a dominant asymmetric X line whose energy peak depends on the composition of the solid solution. The low-energy wing of this line is described by a Lorentz function while the high-energy wing decays exponentially. The intensity of the (e, A) line is between two and three orders of magnitude lower than that of the X line. When the measurement temperature T is varied between 4.2 and 30 K, the profile of the high-energy wing of the X line remains unchanged. The profile of the short-wavelength wing at various temperatures T is described by the function $-a\exp(-\hbar\omega/kT)$ where a is a constant, $\hbar\omega$ is the photon energy, and k is the Boltzmann constant. The profile of the X line and its temperature dependence indicate that this line can be attributed to the recombination of free excitons.[12]

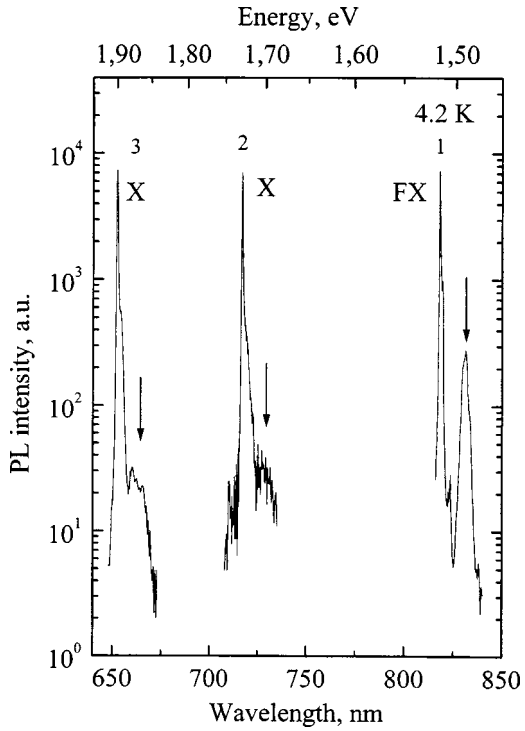

FIG. 1. Photoluminescence spectra of GaAs and $Al_xGa_{1-x}As$ layers measured at an excitation power density of 15 mW/cm^2 and 4.2 K. Composition of $Al_xGa_{1-x}As$ layers, *x*: *1* — $x=0$; *2* — $x=0.17$; *3* — $x=0.27$. The arrows indicate the energy positions of the band–acceptor transition lines.

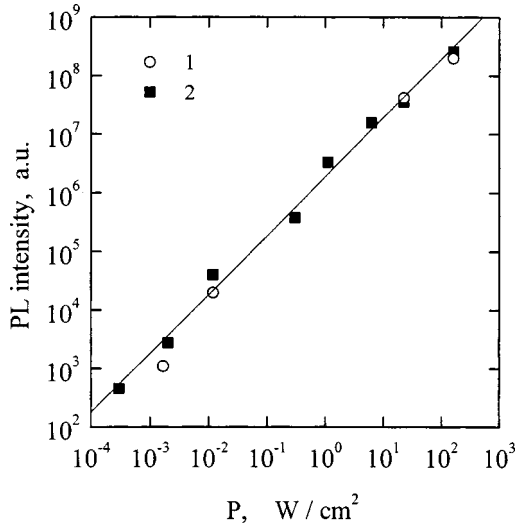

FIG. 2. Integral intensity of the free exciton line in $Al_xGa_{1-x}As$ (with *1* — $x=0.17$; *2* — $x=0.24$) as a function of the laser excitation power density.

Figure 2 gives the integral intensity of the X line $f=I_x(P)$ as a function of the excitation power density for layers containing Al fractions $x=0.17$ and $x=0.24$. It can be seen that as the power varies between 1×10^{-4} and 100 W $\cdot$ cm^{-2}, the dependence $f=I_x(P)$ is a straight line. This indicates that free exciton recombination is the dominant channel for recombination of nonequilibrium carriers in the $Al_xGa_{1-x}As$ layers, and the concentration of nonradiative recombination centers is low. We know that the dominant nonradiative recombination centers in $Al_xGa_{1-x}As$ layers are background impurities, oxygen, and intrinsic point defects.[8,13] Hence, the low concentration of nonradiative recombination centers indicates a low concentration of these impurities and defects.

The widths of the X line obtained in the present study at an excitation power density of 3×10^{-3} W$\cdot$cm^{-2} are 30–50% lower than the lowest values given in the literature[17] and do not exceed the calculated line widths in an impurity-free $Al_xGa_{1-x}As$ solid solution with a random distribution of Ga and Al atoms in the crystal lattice.[9] This suggests that the main mechanism for broadening of the exciton recombination lines in the spectra of these layers is the influence of the random electric fields generated as a result of the random distribution of Al and Ga atoms in the solid solution, and the concentration of ionized impurities in this material is low.

The low concentration of background carbon and oxygen impurities in these $Al_xGa_{1-x}As$ layers is evidently caused by the high degree of segregation of these impurities at the surface of layers grown under conditions to sustain (3×1) As superstructures at their surface. Segregation of carbon and oxygen was observed previously in $Al_xGa_{1-x}As$ during the growth of multilayer quantum-well structures and is one of the reasons for the deterioration in the quality of the

TABLE II. Results of measurements of the static and dynamic characteristics of field-effect transistors fabricated using pseudomorphic AlGaAs/InGaAs/GaAs heterostructures.

Static parameter of transistors	Value	
Specific maximum saturated drain current (at gate voltage +1.5 V), mA/mm	600	
Specific saturated drain current, mA/mm	333	
Specific slope, mS/mm	122	
Drain current saturation voltage, V	1.1−1.3	
Gate cutoff voltage, V	−2.7	
Gate–drain breakdown voltage at gate current 1 mA/mm, V	25	
Dynamic parameters of transistors		
Measurement frequency, GHz	12	17.7
Small-signal gain, dB	7.6	6.8
Specific output power under compression K at 1 dB (P-1), W/mm	0.62	0.78
Specific saturated power, W/mm	0.77	0.91
Efficiency in terms of supplied power, %	41	60

[a]*Note*: The dynamic characteristics of the transistor were measured at a source–drain voltage of 7.0 V, source–gate voltage −1.3 V, and source–drain current 220 mA/cm at 12 GHz and at a source–drain voltage of 7.0 V, source–gate voltage −2.0 V, and source–drain current 160 mA/mm at 17.7 GHz.

reverse GaAs/AlGaAs heterojunction compared with that of the forward AlGaAs/GaAs junction.[14,15]

The statistical and dynamic characteristics of transistors fabricated using these pseudomorphic heterostructures are given in Table II. It can be seen that the values of P and K for our heterostructures are between 1.5 and two times higher than those for mass-produced Russian devices, and are comparable with the parameters of similar transistors manufactured abroad.[10]

To sum up, we have reported the fabrication of ultrapure $Al_xGa_{1-x}As$ solid solutions by molecular beam epitaxy in the range $0 \leqslant x \leqslant 0.38$, having a low concentration of background carbon and oxygen impurities. The incorporation of layers of ultrapure $Al_xGa_{1-x}As$ as the insulator beneath the gate of a microwave field-effect transistor increased the breakdown voltage U_2 to 25 V. The specific output power achieved for these transistors using pseudomorphic heterostructures is 1.5–2.0 times higher than that of Russian mass-produced GaAs transistors, and is comparable with the specific output power of transistors manufactured abroad.

[1] O. Sergeeva, Élektronika No. 2, 39 (1997).
[2] M. S. Shur, *Gallium Arsenide Devices and Circuits* (Plenum Press, New York, 1987; Mir, Moscow, 1991, 632 pp.).
[3] Novosti SVCh Tekh., No. 10, 7 (1995)
[4] A. B. Pashkovskiĭ, Élektronnaya Tekhnika Ser. Élektronika SVCh. No. 4, 14 (1986).
[5] S. Cooper, K. Anderson, K. Salzman, R. Culbertson, J. Mason, D. Bryant, and P. Saunier, in *GaAs IC Symposium*, 1992, p. 183.
[6] D. R. Greenberg, J. A. del Alamo, J. P. Harbison, and L. T. Florez, IEEE Electron Device Lett. **12**, 436 (1991).
[7] D. C. Reynolds, K. K. Bajaj, C. W. Litton, P. W. Yu, J. Klem, C. K. Peng, H. Morkoc, and J. Singh, Appl. Phys. Lett. **48**, 727 (1986).
[8] L. Pavesi and M. Guzzi, J. Appl. Phys. **75**, 4779 (1994).
[9] S. M. Lee and K. K. Bajaj, J. Appl. Phys. **73**, 1788 (1993).
[10] K. Matsunaga, IEEE Microwave Guid. Wave Lett. **5**, 402 (1995).
[11] B. S. Elman, E. S. Koteles, S. A. Zemon, and Y. J. Chi, J. Vac. Sci. Technol. **5**, 757 (1987).
[12] K. Aoki, Y. Okuyama, T. Kobayashi, and K. Yamamoto, J. Phys. C **12**, 647 (1979).
[13] N. Chand, S. N. G. Chu, A. S. Jordan, and M. Geva, J. Vac. Sci. Technol. B **10**, 807 (1992).
[14] N. Chand, S. N. G. Chu, and M. Geva, Appl. Phys. Lett. **59**, 2874 (1991).
[15] D. H. Zhang, C. Y. Li, and S. F. Yoon, J. Cryst. Growth **181**, 1 (1997).

Translated by R. M. Durham

High-power broad-band single-mode InGaAsP/InP superluminescent diode

N. A. Pikhtin, Yu. V. Il'in, A. Yu. Leshko, A. V. Lyutetskiĭ, A. L. Stankevich, I. S. Tarasov, and N. V. Fetisova

A. F. Ioffe Physicotechnical Institute, Russian Academy of Sciences, St. Petersburg, Russia
(Submitted April 29, 1999)
Pis'ma Zh. Tekh. Fiz. **25**, 16–22 (August 12, 1999)

An InGaAsP/InP separate-confinement double heterostructure having a broad gain profile was used to fabricate superluminescent diodes having high optical power (40 mW), a broad radiation spectrum (65 nm at half-width), and low percent modulation ($<1\%$). Using a cw pump current of 150 mA, 1 mW of superluminescence radiation was obtained at the exit from a single-mode optical fiber. © *1999 American Institute of Physics.* [S1063-7850(99)00408-5]

Superluminescent diodes are optimum light sources for low-coherence reflectometry[1] and fiber gyroscopes[2] because of their short coherence length, low internal noise, and broad emission spectrum. In this context, the development of superluminescent diodes emitting in the range 1300–1550 nm with high optical output power and efficient coupling into a single-mode optical fiber is quite a topical issue.

The main problem in obtaining superluminescence emission is to achieve a high gain in the diode without feedback. The most effective methods of suppressing Fabry–Perot modes are: depositing an antireflection coating on the front face of the diode,[3] incorporating an unpumped absorbing rear section,[4,5] and forming an oblique mesastripe.[6]

The aim of the present study was to determine the optimum design of superluminescent diode to obtain superluminescent single-mode emission having maximum power, a broad spectrum, and low percent modulation. The design was based on a mesastripe laser diode[7] using an InGaAsP/InP separate-confinement double heterostructure grown by a modified liquid-phase epitaxy technique.[8] The thickness of the active region and the waveguides in this structure was 800 Å and 1 μm, respectively. The mesastripe laser design with stripe width $W=4$ μm provides efficient coupling of the radiation into a single-mode fiber with a coupling efficiency higher than 50% (Ref. 7). Lasers based on this type of structure, emitting at 1300–1550 nm, have a low threshold current, high internal and external quantum efficiency, and high cw powers when operated in the zeroth transverse mode.[7] Our previous investigations[9] showed that these lasers have an anomalously broad spontaneous radiation and lasing spectrum. The fact that this structure has a broad gain profile makes it very attractive for fabricating a high-power, broad-band superluminescent diode.

In order to obtain superluminescence using the design of separate-confinement double-heterostructure InGaAsP/InP laser diode describe above, we gradually introduced some modifications to suppress the lasing regime. We examined the influence of each modification on the diode operating regime, particularly on characteristics such as the threshold lasing current, the power and efficiency of the superluminescence, the width of the emission spectrum, and the percent modulation of the spectrum.

By studying the radiative characteristics of mesastripe superluminescent diodes having different angles of inclination α of the stripe to the normal (between 0 and 14°) and different cavity lengths L, we determined the optimum values of these quantities (Figs. 1 and 2) which were 10° and 1 mm, respectively. It can be seen from Fig. 1 that as the inclination of the stripe increases, the current at which the diode goes over to the lasing regime increases as does the fraction of the stimulated emission before the lasing threshold. The half-width of the diode stimulated emission spectrum decreases with increasing pump current and this dependence is stronger, the smaller the angle of inclination of the stripe. Moreover, the percent modulation of the spectrum $m=(P_{\max}-P_{\min})/(P_{\max}+P_{\min})$ increases, where $P_{\max}$ and $P_{\min}$ are the maximum and minimum intensities of the peaks in the emission spectrum. The value $m=0.1$ was taken as the threshold point for the transition of the superluminescent diode to the lasing regime (Fig. 1).

It should be noted that the dependence of the differential quantum efficiency η_d of the stimulated emission on the diode length (Fig. 2) is fairly steep compared with the similar dependence for a laser diode[11] because of the single-pass operating regime of this diode (η_d decreases for small L) and the increased internal optical losses (η_d decreases for large L). The value of η_d was measured on the straight section of the watt-ampere characteristic of the diode.

The maximum superluminescence power determined for $m=0.1$ percent modulation was 15 mW at the optimum values of $\alpha=10°$ and $L=1$ mm.

It was possible to increase the range of currents in which the stimulated emission increases by incorporating an additional section into the diode which acts as an absorber. This diode design is similar to the two-section laser whose fabrication technology was described in detail in Ref. 10. In this case, the optimum length of the pumping and absorbing sections was 1000 and 300 μm, respectively. Figure 3 gives the light–current characteristics of a two-section superluminescent diode with an inclined stripe ($\alpha=10°$). By using this diode design we achieved cw superluminescence powers of 40 mW (1300 nm range) and 30 mW (1550 nm range). The half-width of the spectrum was 60 nm with $m=0.03$ percent modulation at maximum power $P_{\max}$ and 65 nm and

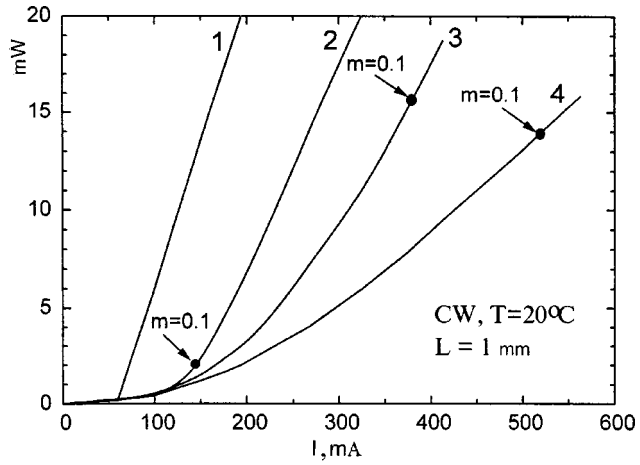

FIG. 1. Watt-ampere characteristics in cw regime of separate-confinement InGaAsP/InP double-heterostructure ($\lambda = 1.55\ \mu$m) superluminescent diode ($L = 1$ mm) with the angle of inclination of the mesastripe α: *1* — $\alpha = 0°$ (laser diode), *2* — $\alpha = 5°$, *3* — $\alpha = 10°$, and *4* — $\alpha = 14°$.

$m = 0.01$, respectively, at the operating power $(1/2P_{\max})$. The far-field pattern of the superluminescent diode has a single-lobed profile with half-widths $\Theta_{\parallel} = 25°$ and $\Theta_{\perp} = 40°$ and does not change over the entire range of pump currents, ensuring that the radiation is efficiently coupled into the single-mode optical fiber. Here the intensity maximum is shifted from the normal by the angle $\Theta_0 = \arcsin(n_{\text{eff}} \sin\alpha)$, where

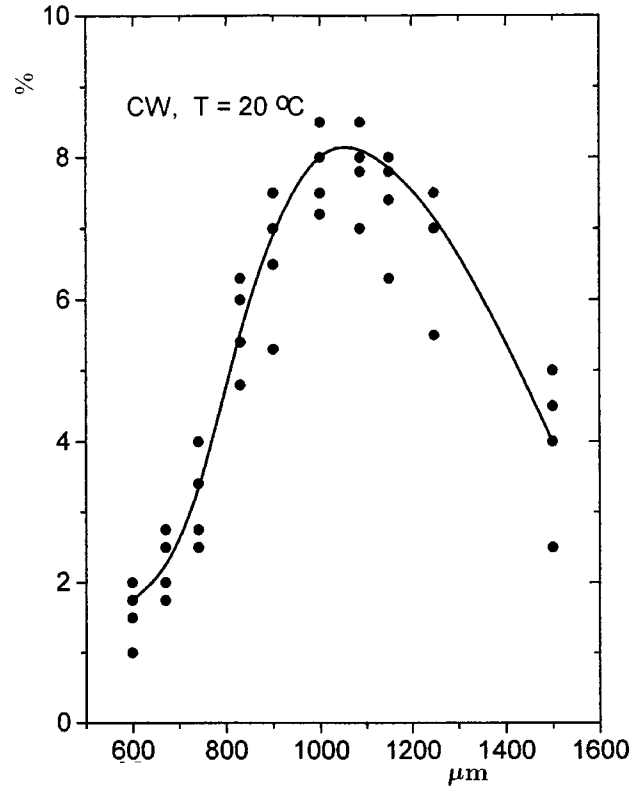

FIG. 2. Differential quantum efficiency from the exit end as a function of the length of a superluminescent diode based on a separate-confinement InGaAsP/InP double heterostructure ($\lambda = 1.55\ \mu$m) with the angle of inclination of the mesastripe $\alpha = 10°$.

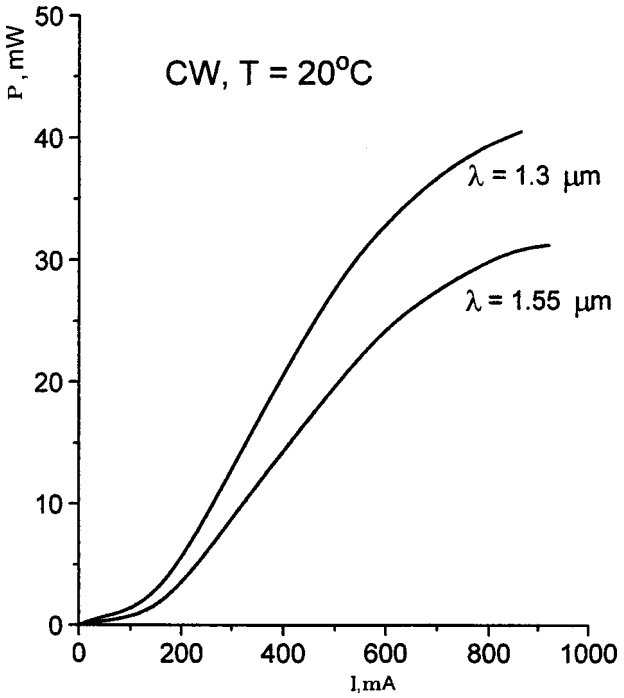

FIG. 3. Watt-ampere characteristics in cw regime of separate-confinement InGaAsP/InP double-heterostructure superluminescent diode ($L = 1$ mm) with 10° inclined mesastripe and an absorbing section ($L = 300\ \mu$m).

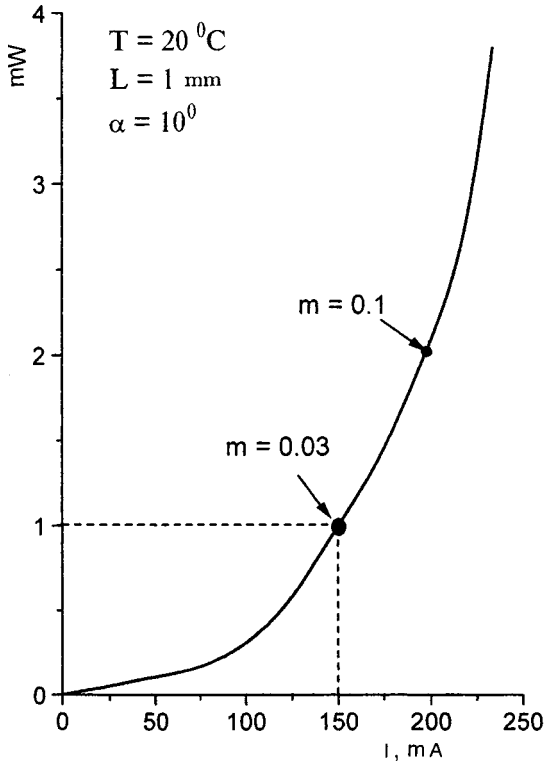

FIG. 4. Output power from single-mode optical fiber as a function of cw Pump current of InGaAsP/InP superluminescent diode ($\lambda = 1.55\ \mu$m) with an inclined mesastripe.

n_{eff} is the effective refractive index of the waveguide (in our case $\Theta_0 = 37°$ for $\alpha = 10°$).

Depositing an antireflection coating with 1% reflection coefficient on the rear face of the diode did not give any appreciable increase in the stimulated emission power.

Experiments to study the coupling of superluminescence into a single-mode fiber (core diameter 9 μm) were carried out using a superluminescent diode ($\lambda = 1.55\ \mu$m) for which the angle of inclination of the mesastripe was 10° and the length $L = 1$ mm. An elongated cone with a fused microlens (fokon) was formed at the end of the optical fiber to achieve efficient matching between the superluminescent diode and the fiber. The crystals were soldered onto a copper heat sink at an angle of $\sim 37°$ to the end of the sink. Figure 4 gives the optical power measured at the exit from the single-mode optical fiber as a function of the diode pump current. At the join with the fiber we measured the output optical characteristics of the superluminescent diode directly from the rear end of the diode. We observed an increase in the optical radiation power of the diode and a narrowing of the stimulated emission spectrum of the superluminescent diode. Moreover, the transition to lasing occurred at lower pump currents. At a constant pump power of 150 mA, the power at the fiber exit was 1 mW, the half-width of the emission spectrum was 40 nm, and the percent modulation $m = 0.03$. The coupling-in efficiency allowing for the influence of the optical fiber on the diode radiation power was 55%.

Further optimization of the electrical and optical characteristics of the superluminescent diode envisages reducing the internal optical losses in the heterostructure used to fabricate the diode and also depositing an antireflection coating of reflection coefficient $< 0.1\%$ on the front face of the diode.

[1] R. C. Youngquist, S. Carr, and D. E. N. Davies, Opt. Lett. **12**, 158 (1987).
[2] W. K. Burns, C. L. Chen, and P. P. Moeller, IEEE J. Lightwave Technol. **LT-1**, 98 (1983).
[3] I. P. Kaminow, G. Eisenstein, and L. W. Stulz, IEEE J. Quantum Electron. **19**, 493 (1983).
[4] N. S. K. Kwong, N. Bar-Chaim, and T. Chen, Appl. Phys. Lett. **54**, 298 (1989).
[5] H. Nagai, Y. Noguchi, and S. Sudo, Appl. Phys. Lett. **54**, 1719 (1989).
[6] C. F. Lin, Electron. Lett. **27**, 968 (1991).
[7] M. A. Ivanov, N. D. Il'inskaya, Yu. V. Il'in, Yu. A. Korsakova, A. Yu. Leshko, A. S. Lunev, A. V. Lyutetskiĭ, A. V. Murashova, N. A. Pikhtin, and I. S. Tarasov, Pis'ma Zh. Tekh. Fiz. **21**(5), 70 (1995) [Tech. Phys. Lett. **21**, 198 (1995)].
[8] Zh. I. Alferov, D. Z. Garbuzov, S. V. Zaĭtsev *et al.*, Fiz. Tekh. Poluprovodn. **21**, 824 (1987) [Sov. Phys. Semicond. **21**, 503 (1987)].
[9] N. A. Pikhtin, I. S. Tarasov, and M. A. Ivanov, Fiz. Tekh. Poluprovodn. **28**, 1983 (1994) [Semiconductors **28**, 1094 (1994)].
[10] N. A. Pikhtin, A. Yu. Leshko, A. V. Lyutetskiĭ, V. B. Khalfin, N. V. Shuvalova, Yu. V. Il'in, and I. S. Tarasov, Pis'ma Zh. Tekh. Fiz. **23**(6), 10 (1997) [Tech. Phys. Lett. **23**, 214 (1997)].
[11] D. Z. Garbuzov, A. V. Ovchinnikov, N. A. Pikhtin, Z. N. Sokolova, I. S. Tarasov, and V. B. Khalfin, Fiz. Tekh. Poluprovodn. **25**, 928 (1991) [Sov. Phys. Semicond. **25**, 560 (1991)].

Translated by R. M. Durham

Elastic properties of gallium and aluminum nitrides

S. Yu. Davydov and A. V. Solomonov

St. Petersburg State Electrotechnical University
(Submitted April 12, 1999)
Pis'ma Zh. Tekh. Fiz. **25**, 23–26 (August 12, 1999)

The Keating model is used to calculate the elastic constants of GaN and AlN for sphalerite and wurtzite structures. The following values of the elastic constants (in gigapascals) were obtained for cubic gallium and aluminum nitride: $C_{11}=325$ and 322, $C_{12}=142$ and 156, $C_{44}=147$ and 138. © *1999 American Institute of Physics.* [S1063-7850(99)00508-X]

In view of the increasing interest being directed toward gallium and aluminum nitrides and the lack of experimental information on their properties,[1] theoretical estimates of the physical characteristics of these compounds are of undoubted interest. However, such estimates must be based on a well-proven theory, used to describe other semiconductor crystals, to provide some guarantee of their reliability. The elastic properties of cubic semiconductor crystals have been described with the best results using the Keating phenomenological theory (see, for instance, Refs. 2–4 and the literature cited therein) and we shall also apply this theory here.

We shall measure the elastic constants in units of $C_0=e^2/d^4$, where e is the electron charge and d is the distance between nearest neighbors. In accordance with the Keating theory, the dimensionless elastic constants of a cubic crystal $c_{ij}=C_{ij}/C_0$ have the form

$$c_{11}=(\alpha+3\beta)/4, \quad c_{12}=(\alpha-\beta)/2, \quad c_{44}=\alpha\beta/(\alpha+\beta), \tag{1}$$

where α and β are the dimensionless force constants of the central interaction, respectively. [Note that the dimensionless force constants can be converted to the dimensional ones introduced by Keating by multiplying the former by $C_0 d/\sqrt{3}$).]

The transition from the elastic constants of sphalerite crystals to those of the wurtzite modification was described in Ref. 5. Using the results obtained in Ref. 5 and the expressions (1), we obtain the following expressions for the dimensionless elastic constants of hexagonal crystals:

$$\begin{aligned}
c_{11}&=(\alpha+\beta)/4+\alpha\beta/(\alpha+\beta)-D,\\
c_{33}&=(3\alpha+\beta)/12+4\alpha\beta/3(\alpha+\beta),\\
C_{44}&=\beta[2\alpha+\beta-(\alpha-\beta)^2/(5\alpha+\beta)]/3(\alpha+\beta),\\
c_{66}&=\beta(5\alpha+\beta)/6(\alpha+\beta)-D,\\
c_{12}&=(3\alpha-\beta)/12-\alpha\beta/3(\alpha+\beta)+D,\\
C_{13}&=(3\alpha+\beta)/12-2\alpha\beta/3(\alpha+\beta),\\
D&\equiv\beta(\alpha-\beta)^2/6(\alpha+\beta)(2\alpha+\beta).
\end{aligned} \tag{2}$$

Thus, by using only two force constants we can describe not only the three elastic constants of cubic crystals, but also the six constants of hexagonal crystals.

These expressions can be used in two ways. If the elastic constants for a cubic crystal are known from the experiments, by determining the constants α and β using the formulas (1), we can find the values of C_{ij} for a hexagonal crystal. Moreover, we can calculate C_{ij} for any relationship between the wurtzite and sphalerite phases in a mixed crystal.[6] Conversely, if the elastic constants of a hexagonal crystal have been measured, by determining the constants α and β using the formulas (2), we can calculate the elastic constants of a cubic crystal.

The values of C_{ij} were recently measured for hexagonal gallium nitride.[7] By selecting the elastic constants C_{13} and C_{33} to use for fitting, we obtain the following values of the dimensionless elastic constants: $\alpha=4.61$ and $\beta=1.12$. The experimental and calculated values of C_{ij} for GaN are given in Table I. The maximum deviation ($\sim 10\%$) is observed for C_{12}. For cubic crystals with the values of the force constants determined above, we obtain the following values of the elastic constants (in gigapascals):

$$C_{11}=325, \quad C_{12}=142, \quad C_{44}=147.$$

Using the results of Ref. 6, we can show that on changing from a wurtzite to a sphalerite structure, the elastic constant C_{11} increases by approximately 2%, C_{44} and C_{66} increase by 5%, and C_{12} decreases by 5%. Table I also gives data for AlN. As for GaN, the elastic moduli C_{13} and C_{33} were used to determine the force constants, which yielded: $\alpha=4.36$ and $\beta=0.92$. Note that the experimental results for aluminum nitride were taken from Ref. 8, where polycrystal-

TABLE I. Experimental and theoretical values of the elastic constants (in gigapascals) for hexagonal GaN and AlN crystals.

		C_{11}	C_{33}	C_{44}	C_{66}	C_{12}	C_{13}
GaN	Exp.	390	398	105	123	145	106
	Theor.	373	398	105	123	130	106
AlN	Exp.	345	395	118	–	125	120
	Theor.	369	395	96	112	145	120

line films were studied. Thus, it is not surprising that the difference between the experimental and calculated data is far greater in this case: $\sim 7\%$ for C_{11}, 16% for C_{12}, and 19% for C_{44}. For cubic crystals of aluminum nitride we have (in gigapascals): $C_{11}=322$, $C_{12}=156$, and $C_{44}=138$.

It is interesting to note that the elastic modulus of compression for a cubic crystal $B=(C_{11}+2C_{12})/3$ is 203 GPa for GaN and 211 GPa for AlN. Calculations from first principles give 195 GPa for both crystals[9] which is in good agreement with our data. (Note that for hexagonal crystals the value of B given in Ref. 9 is also 195 GPa whereas Ref. 7 gives $B=210$ GPa. Therefore, the exaggerated value of the compression modulus obtained by us compared with that calculated in Ref. 9 is quite consistent.)

In conclusion we note that as before, the Keating phenomenological approach gives the most accurate results for estimates of the elastic characteristics of semiconductor crystals. Calculations from first principles are extremely laborious while the use of various strong coupling methods (see, for example, Refs. 3, 4, and 10–12) leads to fairly large discrepancies compared with the experiment, although they provide a better understanding of the nature of the elasticity.

[1] *Proceedings of the Seventh International Conference on Silicon Carbide, III-Nitrides and Related Materials*, Stockholm, Sweden, 1997, edited by G. Pensl, H. Morkoc, B. Monemar, and E. Janzen (Trans Tech, Switzerland, 1998).
[2] S. P. Nikanorov and B. K. Kardashov, *Elasticity and Dislocation Inelasticity of Crystals* [in Russian], Nauka, Moscow (1985), 250 pp.
[3] S. Yu. Davydov and S. K. Tikhonov, Fiz. Tekh. Poluprovodn. **30**, 834 (1996) [Semiconductors **30**, 447 (1996)].
[4] S. Yu. Davydov and S. K. Tikhonov, Fiz. Tekh. Poluprovodn. **30**, 1300 (1996) [Semiconductors **30**, 683 (1996)].
[5] R. M. Martin, Phys. Rev. B **6**, 4546 (1972).
[6] S. Yu. Davydov and S. K. Tikhonov, Fiz. Tverd. Tela (St. Petersburg) **37**, 2221 (1995) [Phys. Solid State **37**, 1212 (1995)].
[7] A. Polian, M. Grimsditch, and I. Grzegory, J. Appl. Phys. **79**, 3343 (1996).
[8] A. V. Dobrynin, I. P. Kazakov, and G. A. Naĭda, Zarub. Élektron. Tekh. **4**, 44 (1989).
[9] K. Miwa and A. Fukumoto, Phys. Rev. B **48**, 7897 (1993).
[10] W. A. Harrison, *Electronic Structure and Properties of Solids* [Russ. transl.], Nauka, Moscow (1983), 382 pp.
[11] M. Kitamura and W. A. Harrison, Phys. Rev. B **44**, 7941 (1991).
[12] M. Kitamura, S. Muramatsu, and W. A. Harrison, Phys. Rev. B **46**, 1351 (1991).

Translated by R. M. Durham

Recombination of preadsorbed oxygen atoms at the surface of solids

V. F. Kharlamov and K. M. Anufriev

Orlov State Technical University
(Submitted March 31, 1999)
Pis'ma Zh. Tekh. Fiz. **25**, 27–32 (August 12, 1999)

Relaxation measurements are used to establish that for a concentration of gas-phase oxygen atoms $n=10^{14}\,\mathrm{cm}^{-3}$ heterogeneous recombination of oxygen atoms at the surface of copper and zinc sulfide takes place by a mechanism involving recombination of preadsorbed (precursor state) atoms. A hypothesis is put forward for the existence of a universal mechanism for the catalytic acceleration of heterogeneous chemical reactions. © *1999 American Institute of Physics.* [S1063-7850(99)00608-4]

Chemical processes taking place at the interface between solids and active gases have been studied by us using a method of relaxation measurements which involves simultaneously recording the kinetic adsorption curves of the substances reacting at the surface $N(t)$ and the dynamic reaction effect $F(t)=P_r(t)-P=F_1+F_2+F_3$, where P_r is the gas pressure at the surface of the catalyst, P is the gas pressure at the vessel walls, F_1 is the momentum flow transferred by molecules of the reagents and reaction products diffusing in the gas, F_2 is the pressure force which is nonzero when the molecules, i.e., the products of the heterogeneous reaction which have left the surface, possess an epithermal excess of translational kinetic energy (recoil effect), and F_3 is the pressure force produced by the temperature difference of the gas and the catalyst (radiometric effect). The values of F_1 and F_2 depend linearly on the heterogeneous reaction rate J and when the reagent flux is modulated, they vary instantaneously in accordance with the change in reaction rate. The steady-state value of F_3 is proportional to the reaction rate and its rate of change as J varies depends on the rate of thermal relaxation of the system.[1,2]

In the experiments, gas at pressure $P=30\,\mathrm{Pa}$ was pumped continuously through a glass vacuum chamber *1* whose walls could be heated to 500 K (Fig. 1). Adsorption measurements were made using a piezoresonance quartz balance with a sensitivity of $\sim 10^{-3}$ ML. The material being studied was deposited as a layer of thickness $d\approx 0.1$ mm on both sides of a piezoelement *2* and the concentration N of chemisorbed particles was determined from the drop in the natural frequency of the piezobalance f, which was measured using a ChZ-54 frequency meter. The temperature coefficient of frequency of the quartz resonator was $10^{-1}\,\mathrm{Hz}\cdot\mathrm{K}^{-1}$ and the measurement error caused by heating of the piezoelement by the reaction taking place at its surface was less than 1%. It was established that the adsorption capacity of the natural surface of the piezoelement ($d=0$) was negligible.

The dynamic reaction effect was measured using an automatic balance with magnetic suspension. A 10 mg quantity of the sample was deposited as a layer of thickness $d\approx 0.1$ mm on the outer surface of a substrate *3* which was attached by means of a quartz thread *4* to a miniature magnet *5* suspended inside a glass tube in the magnetic field produced by a solenoid *6*. The substrate *3* was made of two horizontal mica plates of thickness 0.1 mm and diameter 15 mm, placed 0.2 mm apart. The gap between the plates served as thermal insulation so that the heat released as a result of the reaction taking place at the surface of the catalyst led to the establishment of a temperature difference between the upper and lower surfaces of the substrate *3*, which could be used to measure F_3. The position of the magnet *5* along the vertical axis was tracked using a differential photoelectric detector consisting of two light-emitting diodes *7* and two photodiodes *8*. The signal from the detector was fed to the control unit for the magnetic suspension, which varied the current in the solenoid *9* to automatically compensate for changes in the weight of the sample. The current in the solenoid *9* served as a measure of the dynamic reaction effect. This signal, digitized using an analog-to-digital converter, was fed to a PC which recorded the $F(t)$ curves. The sensitivity of the automatic balance, calibrated using a 1 mg load, was $2.5\times 10^{-8}\,N$ with a time constant 10^{-1} s.

The reaction $\mathrm{O}+\mathrm{O}\rightarrow\mathrm{O}_2$ was studied using spectrally pure oxygen obtained by decomposition of $KMnO_4$. The molecules were dissociated to form atoms using an rf electric discharge in the gas. The atomic concentration in the reaction vessel, measured by a thermal probe technique, was $n=10^{14}\,\mathrm{cm}^{-3}$. We used ultradispersed copper powder having spherical particles of mean diameter 100 nm and a finely dispersed ZnS–Cu phosphor having a specific surface area of $\sim 1\,\mathrm{m}^2\cdot\mathrm{g}^{-1}$. The samples were held in an atomic–molecular oxygen mixture at $T=350$ K for 1 h to purify their surfaces, and the sputtering of adsorbed and crystal-forming particles by O atoms was observed by using the piezobalance.

When the sample was heated by an incandescent lamp focused onto the substrate *3*, the force acting on the substrate from the gas increased smoothly (Fig. 2, curve *1*). After the steady-state flux of oxygen atoms was switched on, an abrupt increase in the dynamic reaction effect was observed, followed by a continuous increase in the force F caused by heating of the catalyst as a result of the exothermic reaction $\mathrm{O}+\mathrm{O}\rightarrow\mathrm{O}_2$ taking place at its surface (curves *2* and *3*). The initial jump on curves *2* and *3* can be used to determine: $F_1+F_2>0$. Since for heterogeneous reactions we find $\mathrm{R}+\mathrm{R}\rightarrow\mathrm{R}_2$ and $F_1>0$ (Refs. 1 and 2) this condition implies

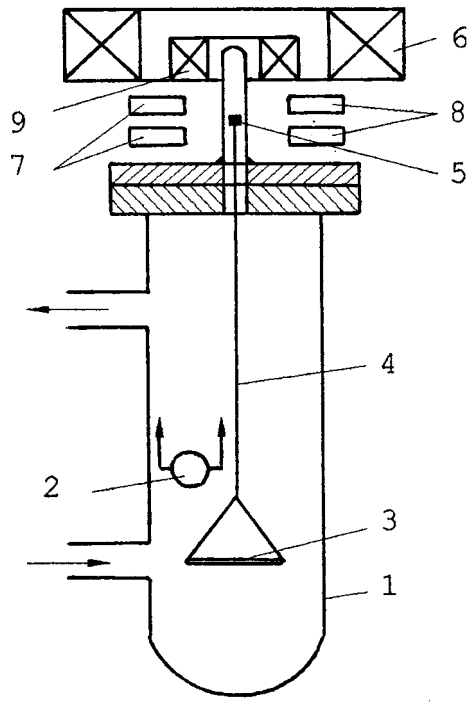

FIG. 1. Schematic of experiments.

that $F_2>0$, i.e., O_2 molecules formed during the reaction leave the surface of ZnS and Cu with excess kinetic translational energy (as a result of the repulsive interaction between the O_2 molecules and the surface).

After the source of oxygen atoms is switched on, the surface of the samples slowly fills with chemisorbed atoms and no initial sections of abrupt surface filling are observed on the adsorption curves; the initial rate of increase in J ($F \sim J$) is two orders of magnitude higher than the initial rate of filling of the surface with chemisorbed atoms $(N_{\max})^{-1}dN/dt=(\Delta f_{\max})^{-1}df/dt$. The oxygen atoms and molecules compete for adsorption sites on the surface; the atoms displace (Cu) or sputter adsorbed O_2 molecules in the reaction $O+O \rightarrow O_2$ (ZnS). This leads to the appearance of extrema on the $f(t)$ curves obtained after switching on or off the source of atoms (Fig. 2, curves *4* and *5*).

When the heterogeneous reaction $R + R \rightarrow R_2$ takes place involving chemisorbed atoms and atoms escaping from the gas phase R (Eley–Rideal and Langmuir–Hinshelwood mechanisms), the following conditions should be satisfied:

$$\tau<N_{\max}(j\gamma)^{-1}, \quad J(t)=aN(t)+bN^2(t), \tag{1}$$

where τ is the time taken to establish adsorption equilibrium after switching on the atomic flux j, γ is the coefficient of heterogeneous atomic recombination, a and b are coefficients.[2,3] In our experiments we have $j=10^{18}\,\mathrm{cm}^{-2}\cdot\mathrm{s}^{-1}$, $\gamma=10^{-3}$–10^{-2}, and $N_{\max}=10^{14}\,\mathrm{cm}^{-2}$ (Refs. 2 and 4) which gives $\tau<10^{-2}$–10^{-1} s, which does not agree with the experimental values $\tau\sim 10$ s (Fig. 2, curves *4* and *5*). Judging by the initial jumps on the $F(t)$ curves when the source of atoms is switched on and off, the reaction rate does not increase with increasing concentration of chemisorbed atoms. Violation of the conditions (1) implies that the reaction takes place via a mechanism involving recombination of preadsorbed (weakly bound to the surface) atoms whose concentration N_1 is low: $N_1 \ll N$. An alternative hypothesis, that the reaction takes place by an impact mechanism $2R+Z\rightarrow R+(RZ)\rightarrow R_2+Z$ at Z active centers having the concentration $N_2<10^{12}\,\mathrm{cm}^{-2}$, is ruled out by its requiring physically meaningless values of the reaction cross sections: $\sigma=\gamma N_2^{-1}>(10^{-15}$–$10^{-14})\,\mathrm{cm}^2$.

In all the cases studied by us the heterogeneous reactions involve preadsorbed particles.[3,5–7] On this basis, taking into account experience gained throughout the world,[8,9] we can put forward a hypothesis on a universal law of heterogeneous catalysis: catalytic acceleration of any chemical process taking place at a solid–gas interface is caused by preadsorbed particles participating in chemical conversions (in other words, trapping of incoming gas-phase molecules of a particular species by the surface of a solid in the preadsorption

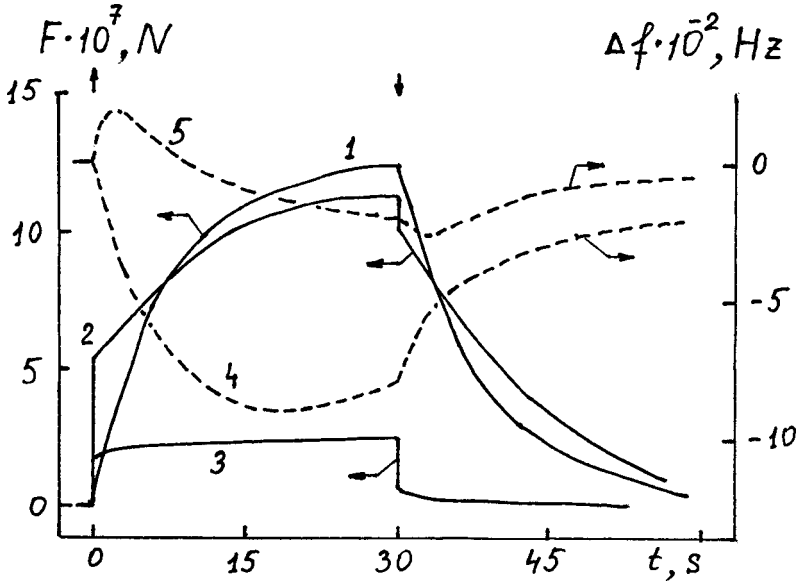

FIG. 2. Force from the gas (oxygen) acting on the substrate with deposited copper (*1*, *2*) or zinc sulfide (*3*) as a function of the time after switching on (↑) or switching off (↓) the light source (*1*) or a flux of oxygen atoms (*2*, *3*): *4*, *5* — frequency of piezobalance with deposited layer of Cu (*4*) or ZnS (*5*) as a function of the time after switching on and off a source of O atoms.

state abruptly increases the effective cross section of the heterogeneous chemical process). In this case, the condition $J=n_1 q$ is satisfied, where J is the reaction rate, n_1 is the concentration of preadsorbed particles of a particular species involved in the reaction, and q is a quantity which depends on the rate constants of the surface reactions and the concentrations of chemisorbed and preadsorbed particles participating in the reaction.

[1] V. F. Kharlamov, Poverkhnost' No. 11, 122 (1993).
[2] V. F. Kharlamov, *Recombination of Atoms at the Surface of Solids and Accompanying Effects* [in Russian], Tomsk State University Press, Tomsk (1994), 207 pp.
[3] V. F. Kharlamov, Sh. L. Izmailov, and N. Ph. Vasil'ev, React. Kinet. Catal. Lett. **60**(1), 107 (1997).
[4] Sh. L. Izmaĭlov and V. F. Kharlamov, Kinet. Katal. **23**, 1183 (1982).
[5] V. F. Kharlamov, K. M. Anufriev, Yu. V. Mosin *et al.*, Pis'ma Zh. Tekh. Fiz. **24**(5), 23 (1998) [Tech. Phys. Lett. **24**, 176 (1998)].
[6] V. F. Kharlamov, V. N. Lisetskiĭ, and O. A. Ivashchuk, Zh. Fiz. Khim. **72**(2), 297 (1997).
[7] V. F. Kharlamov, N. F. Vasil'ev, O. A. Ivashchuk *et al.*, Pis'ma Zh. Tekh. Fiz. **24**(3), 54 (1998) [Tech. Phys. Lett. **24**, 105 (1998)].
[8] M. W. Roberts and C. S. McKee, *Chemistry of the Metal-Gas Interface* (Clarendon Press, Oxford, 1978; Mir, Moscow, 1981, p. 317).
[9] O. V. Krylov and B. R. Shub, *Nonequilibrium Processes in Catalysis* [in Russian], Moscow (1990), 288 pp.

Translated by R. M. Durham

Multiplication of runaway electrons in discharges with repeated fuel pellet injection

B. V. Kuteev and A. Yu. Kostryukov

St. Petersburg State Technical University
(Submitted April 21, 1999)
Pis'ma Zh. Tekh. Fiz. **25**, 33–40 (August 12, 1999)

An analysis is made of an effect involving increased evaporation and toroidal acceleration of pellets during their repeated injection in a tokamak, caused by an avalanche-like growth in the population of runaway electrons additionally stimulated by the pellet injection. © *1999 American Institute of Physics.* [S1063-7850(99)00708-9]

Injection of fuel pellets, consisting frozen hydrogen isotopes,[1] is being developed to achieve an efficient system for injecting fuel into the central part of a tokamak plasma. In a reactor the injection will be a repetitive process, at a frequency of 1–10 Hz. Very few experimental or theoretical studies have been made of the effects taking place in a plasma in this regime. The first experiments on repeated pellet injection carried out in ASDEX-Upgrade[2] revealed an unexpected reduction in the depth of penetration and increased twisting of the pellet trajectory for those injected at the end of a series. The observed increase in the rate of evaporation and toroidal acceleration (blowing) of the pellets from the first to the subsequent ones cannot be explained in terms of standard models, which accurately describe evaporation and toroidal acceleration of pellets for single injection.[3,4] In the present study we analyze the change in the conditions of evaporation and toroidal acceleration of pellets when these are injected repetitively in tokamaks. The main reason for the increased evaporation and toroidal acceleration of the pellets is assumed to be an avalanche-like growth in the population of runaway electrons, additionally stimulated by the pellet injection, caused by close collisions between runaway and thermal electrons, i.e., collisions in which a thermal electron receives an energy comparable with the critical energy for transition to the runaway regime.

The rate of generation of runaway electrons as a result of diffusion in velocity space S is determined by the Dreicer parameter $\varepsilon = E/E_{\text{crit}}$, where E is the longitudinal electric field in the plasma and E_{crit} is the critical electric field.[5] During pellet injection the plasma temperature T_e falls, while the density n_e increases. The plasma conductivity is $\sigma \sim T_e^{3/2}$, i.e., $E \sim T_e^{-3/2}$. As a result $\varepsilon \sim n_e^{-1} T_e^{-1/2}$ decreases and the generation of runaway electrons is suppressed.

A second well-known mechanism for the generation of runaway electrons is associated with the so-called avalanche multiplication of runaways as a result of isolated close collisions.[6] Avalanche multiplication can take place if the plasma already contains runaway electrons having the density n_r before the onset of pellet injection. The experimentally measured energy limit $W_{\max}$ for runaway electrons is usually a few tens of mega-electronvolts. The cross section for Coulomb collision between a relativistic electron and a thermal electron of velocity $v \ll c$ may be written[6] as $(d\sigma/dW_s) = (e^4/8\pi\varepsilon_0^2 m_e c^2 W_s^2)$, where W_s is the energy acquired by the thermal electron. The increase n_r in the number of secondary runaway electrons as a result of these collisions may be expressed as $(dn_r/dt) = n_r n_e c \int_0^{W_{\max}} (d\sigma_s/dW_s) P_r \times (W_s) dW_s$. Here n_r and $W_{\max}$ are the density and maximum energy of the runaway electrons, and $P_r(W_s)$ is the probability that an electron, having acquired the energy W_s will be converted to the runaway regime. Following Ref. 6, we shall assume that an electron which has acquired above-critical energy becomes a runaway, while an electron which has acquired a lower energy returns to a Maxwellian distribution, i.e., we assume that $P_r(W_s) = 0$ for $W_s < W_{\text{crit}}$ and $P_r(W_s) = 1$ for $W_s > W_{\text{crit}}$. Then, using the well-known expression for the critical energy,[6] $W_c = (mV_c^2/2)$, $V_c^2 = ((2 + Z_{\text{eff}}) \pi e^3 n_e \ln \Delta / mE)$, and integrating over energies, we can estimate the rate of generation of secondary runaway electrons as in Ref. 6:

$$\frac{dn_r}{dt} = \frac{n_r eEc}{2m_e c^2 \ln \Lambda (2 + Z_{\text{eff}})} = \frac{n_r}{t_0},$$

$$t_0 = \frac{2m_e c \ln \Lambda (2 + Z_{\text{eff}})}{eE}. \tag{1}$$

It is important to note that the runaway electron multiplication time does not depend on the density and is inversely proportional to the electric field in the plasma. Since injection leads to an increase in the electric field at constant current and decreasing temperature, avalanche-like multiplication of runaway electrons is stimulated.

In discharges with high plasma density the rate of multiplication of runaway electrons should be estimated slightly differently. When the plasma density is $n_e \geqslant 10^{14}\,\text{cm}^{-3}$, we find that $\varepsilon = E/E_{\text{crit}}$ is of similar order of magnitude to the parameter $T_e/m_e c^2$. In this case, the electrons converted to the runaway regime are relativistic.[7] Thus, instead of the classical expression for the critical energy for the transition to the runaway regime, we need to use a relativistic expression for the critical energy: $W_c = \sqrt{p_c^2 c^2 + m_e^2 c^4}$, where p_c is the critical momentum for transfer to the runaway regime: $p_c^2 = m_e^2 V_e^2 (1 - (V_e^2/c^2))^{-1}$. As a result, we obtain the following expression for the critical energy:

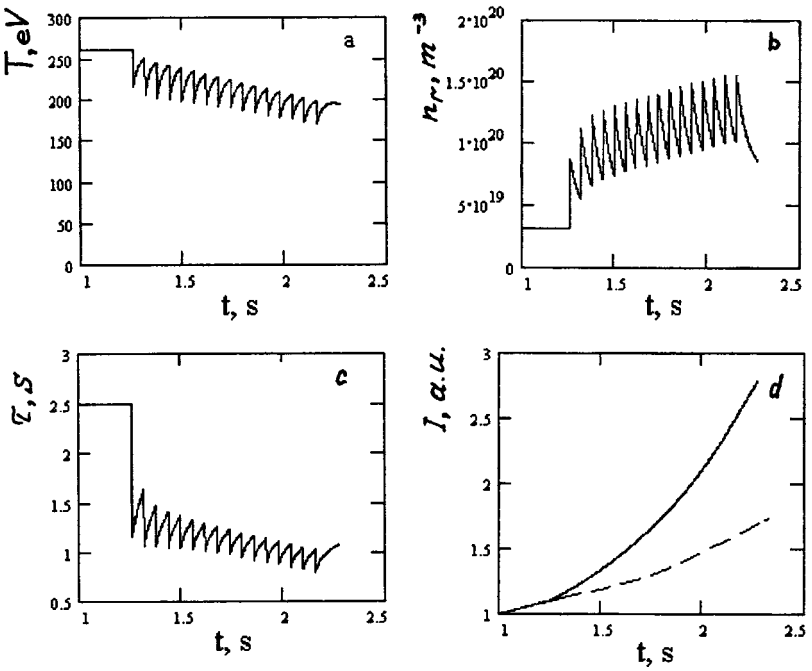

FIG. 1. Model evolution of temperature (a), model evolution of density (b), characteristic time for runaway electron multiplication (c), and number of runaway electrons: dashed curve — multiplication without injection, solid curve — multiplication with multiple injection (d).

$$W_c = m_e c^2 \sqrt{\frac{1}{(\alpha-1)}+1},$$

where

$$\alpha = \frac{E m_e c^2}{E_{\text{crit}} T} = 1.1\times 10^{21}\frac{E[\text{V/m}]}{n_e[\text{m}^{-3}]}. \tag{2}$$

Neglecting any losses of secondary runaway electrons, we can use the following equation to estimate the increase in their number:

$$\frac{dn_r}{dt} = \frac{n_r c n_e \pi e^4}{2 m_e c^2 W_c} = \frac{n_r}{t_1}, \quad t_1 = \frac{2 m_e c^2 W_c}{c n_e \pi e^4}. \tag{3}$$

In the relativistic case, the critical energy (2) depends weakly on the electric field and density. Nevertheless, after the beginning of injection the runaway electron multiplication time becomes shorter because of an increase in the plasma density.

We used a model evolution of the plasma temperature and density (Figs. 1a and 1b), typical of an experiment with multiple fuel pellet injection, to calculate the increase in the density n_r.

Figure 1c shows the calculated evolution of the time constant for exponential multiplication of the runaway electron population and population growth (Fig. 1d) for the case of constant density and temperature (dashed curve) and for the values typical of an experiment with multiple fuel pellet injection (solid curve). The characteristic times for exponential growth of the runaway electron population is $\tau = 2.5$ s before the onset of injection, and reduces to $\tau = 1$ s after the onset of injection.

We shall now analyze the influence of runaway electrons on the rate of pellet blowing.

Electrons whose energies far exceed the thermal level interact with a pellet as follows. Electrons having energies higher than 10 keV lose very little energy as they pass through the neutral cloud.[4] Electrons having energies higher than 300 keV, impinging on the pellet in the direction of the magnetic field, pass through the pellet, which has a transverse dimension of 1.6 mm. They lose approximately 150 keV as they pass through and cause additional isotropic evaporation of the pellet.[4] This evidently does not cause any additional pellet blowing. Thus the additional blowing may be caused by electrons having energies W_{sth} between 10 and 150 keV (''superthermal'' electrons), not by runaway electrons.

In the presence of runaway electrons, superthermal electrons having energies much higher than the average thermal energy but below the critical energy are also generated by close collisions between runaways and thermal electrons. Thus, the discharge contains three groups of electrons: Maxwellian electrons having the average velocity $u = j/en_e \ll V_T$, relativistic runaway electrons, and superthermal electrons having energies between the average thermal energy and the critical energy for transition to the runaway regime. The growth in the runaway electron population causes an increase in the number of superthermal electrons which may affect the evaporation and blowing of the pellets.

We shall estimate the density of runaway electrons in the discharge which would be sufficient to double the toroidal displacement. For this purpose we estimate $f_{\text{sth}}(V)$ which is the velocity distribution of superthermal electrons in a plasma having a given runaway electron density n_r, thermal electron temperature T_e, and density n_e.

The rate of generation of superthermal electrons having velocities between V and $V+dV$ can be calculated by analogy with the rate of runaway electron generation as

$$I = n_r n_e v_r \frac{d\sigma_s}{dW_s}\frac{dW_{\text{sth}}}{dV} = n_r n_e c \frac{e^4}{2\pi\varepsilon_0^2 m_e^2 c^2 V^3}. \tag{4}$$

Since we are interested in superthermal electrons having energies up to $W_{\text{sth max}}=150\,\text{keV}$, we used the classical expression for the energy $W_{\text{sth}}=(1/2)m_eV^2$. Relaxation of the superthermal electrons to form a Maxwellian distribution takes place as a result of a large number of distant electron–electron collisions having the effective frequency

$$\nu_{\text{sth}}(V)=\frac{1}{3(\pi)^{3/2}}\frac{n_e e^4\ln\Lambda}{\varepsilon_0^2 m_e^2 V^3}.$$

The superthermal electrons increase their energy, being accelerated by the electric field. However since for electrons having energies $W_{\text{sth}}<W_{\text{sth max}}=150\,\text{keV}<W_c$ the force of friction with thermal electrons is much greater than the accelerating electric force $F(V)=m_eV\nu_{\text{sth}}(V)\gg eE$, we neglect the acceleration of the superthermal electrons by the electric field. The superthermal electrons are distributed over velocity directions, depending on their energy. Low-energy electrons are generated as a result of tangential collisions[8] and can initially fly off almost perpendicular to the magnetic field. They then relax to form an isotropic Maxwellian distribution. For a rough estimate we shall assume that all the superthermal electrons fly off in the opposite direction to the electric field, and in this velocity half-space their distribution is isotropic.

The kinetic equation for the velocity distribution of the superthermal electrons has the following form:

$$I(V)=-\frac{1}{V^2}\frac{d}{dV}(V^2 f_{\text{sth}}(V)\nu_{\text{sth}}(V)V). \tag{5}$$

Here I is a source of superthermal electrons (4). The term on the right-hand side is the difference between the fluxes of superthermal electrons entering and leaving an element of velocity space as a result of Coulomb collisions between superthermal electrons and Maxwellian ones. Substituting Eq. (4) into Eq. (5) gives

$$\frac{df}{dV}=-\frac{3(\pi)^{1/2}n_r}{2c\ln\Lambda}\frac{1}{V}. \tag{6}$$

The solution of Eq. (6) will be a logarithmically decreasing distribution of superthermal electrons:

$$f_{\text{sth}}(V)=\frac{3(\pi)^{1/2}n_r}{2c\ln\Lambda}\ln\left(\frac{V_c}{V}\right). \tag{7}$$

The integration constant in the numerator of the logarithm is selected so that the distribution function vanishes at critical velocity. The density of superthermal electrons having energies between $W_{\text{sth min}}=10\,\text{keV}$ and $W_{\text{sth max}}=150\,\text{keV}$ can be estimated as $n_{\text{sth}}=\int_{V_{\min}}^{V_{\max}} f_{\text{sth}}dV \approx n_r(3(\pi)^{1/2}/2\ln\Lambda)(V_{\max}/c)\approx(n_r/10)$.

The distribution functions of Maxwellian, runaway, and superthermal electrons are shown schematically in Fig. 2. We estimate the heat flux of the superthermal electrons $Q_{\text{sth}}=\int_{V_{\min}}^{V_{\max}}(m_eV^2/2)\,Vf_{\text{sth}}dV\approx n_r(3(\pi)^{1/2}/2c\ln\Lambda)\times(m_e/2)(V_{\max}^4/4)$. The additional rate of evaporation caused by the superthermal electrons can be estimated as the heat flux incident on half the pellet surface directed along the magnetic field, divided by the sublimation energy:

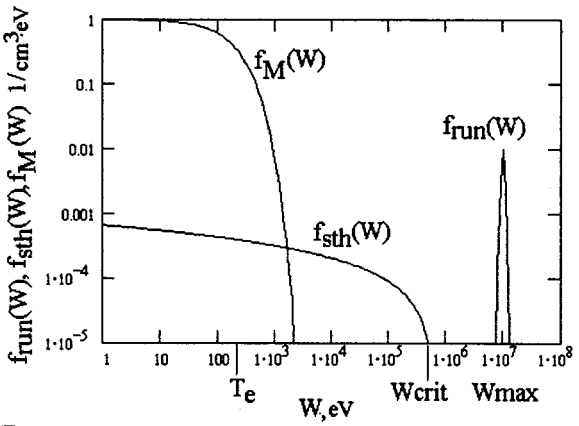

FIG. 2. Distribution functions: f_M — thermal electrons, f_{run} — runaway electrons, f_{sth} — superthermal electrons, $T_c=200$ eV, $n_e=10^{14}\,\text{cm}^{-3}$, and $n_r=3\times10^8\,\text{cm}^{-3}$.

$$\frac{dN_{\text{sth}}}{dt}=\frac{Q_{\text{sth}}\pi r_p^2}{\lambda_m/_2}.$$

Here $\lambda_m=15.2\times10^{-3}$ eV/molecule is the sublimation energy of deuterium. The additional toroidal acceleration of the pellet can be estimated using the reactive acceleration equation:[4]

$$M(t)(dv_z/dt)=\langle=\cos^2\theta\rangle Um_i\frac{dN_{\text{sth}}}{dt},$$

where $M(t)$ is the pellet mass, dv_z/dt is the toroidal acceleration, $\langle\cos^2\theta\rangle=1/2$ (θ is the angle between the direction of emission of the atoms from the pellet surface and the toroidal direction), and $U\approx10^6$ cm/s is the escape velocity of the atoms, estimated as the gas velocity for transition of the flux to supersonic. The density of runaway electrons needed to achieve appreciable toroidal displacement is extremely low. For instance, a runaway electron density of around $3\times10^8\,\text{cm}^{-3}$ in a layer several centimeters thick is sufficient to describe the local enhanced pellet blowing effect observed in ASDEX-Upgrade.[2]

The observed doubling of the pellet toroidal displacement can only be explained in terms of existing models by assuming a sixfold increase in current density and a 30% increase in T_e in the pellet evaporation zone, which cannot be attributed to the negligible expulsion of current from the plasma periphery cooled by the pellet injection. An estimate of the pellet stopping by the radial temperature and plasma density gradients showed that under existing experimental conditions this effect is also negligible.

To sum up, we have shown that multiple injection of fuel pellets in a plasma creates conditions for accelerated avalanche-like multiplication of runaway electrons. At low plasma densities, when the critical energy for runaway is much lower than the rest energy, electron multiplication is accelerated by an increase in the electric field in the plasma, which is in turn caused by a drop in temperature after injection. At high densities when the critical energy is comparable

with the rest energy, runaway electron multiplication is also accelerated but as a result of an increase in the plasma density.

[1] S. L. Milora, W. A. Houlberg, L. L. Lenguel *et al.*, Nucl. Fusion **35**, 657 (1995).
[2] P. T. Lang, M. Alexander, K. Buchl *et al.*, in *Abstracts of the 21st Europhys Conference*, Vol. 18B, Part 1, p. 306.
[3] P. B. Parks and R. J. Turnbull, Phys. Fluids **21**, 1945 (1978).
[4] B. V. Kuteev, Nucl. Fusion **35**, 431 (1995).
[5] H. Dreicer, Phys. Rev. **115**, 238 (1959).
[6] R. Jayakumar, H. H. Fleischmann, and S. J. Zweben, Phys. Lett. A **172**, 447 (1993).
[7] J. W. Connor and R. J. Hastie, Nucl. Fusion **15**, 415 (1975).
[8] N. T. Besedin and I. M. Pankratov, Nucl. Fusion **26**, 807 (1986).

Translated by R. M. Durham

Characteristic time for the evolution of instability of a droplet charged to the Rayleigh limit

D. F. Belonozhko and A. I. Grigor'ev

Yaroslavl State University
(Submitted April 21, 1999)
Pis'ma Zh. Tekh. Fiz. **25**, 41–45 (August 12, 1999)

The nonlinear problem of the capillary oscillations of a charged droplet is solved to estimate the characteristic time for the evolution of instability of a droplet carrying critical charge. It is observed that breakup is delayed because of the hydrodynamic inertia of the droplet. © *1999 American Institute of Physics.* [S1063-7850(99)00808-3]

Studies of the capillary oscillations and stability of charged droplets are of considerable interest for numerous applications in geophysics, scientific instrument manufacture, technical physics, and technology.[1] However, most theoretical investigations have been made using a linearized system of hydrodynamic equations, and

studies taking into account the real nonlinearity of the phenomenon have only started to appear comparatively recently.[2,3] Bearing in mind the nonlinearity of the problem of calculating the shape of an oscillating droplet at any point in time, we shall solve the problem of the capillary oscillations of a charged droplet, i.e., the Rayleigh problem[4] but, unlike Ref. 4, we shall use a linear formulation in the second order of smallness for the amplitudes of various modes.

Let us assume that a droplet of ideal, perfectly conducting liquid, having the density ρ and surface tension γ, carries the charge Q. Linear theory[4] assumes that there is a time, which may be taken to be the initial time $t=0$, when the droplet shape is described by the second mode of linear capillary oscillations of small finite amplitude ε and the velocity field is zero. The initial droplet is equivalent to a spherical droplet of radius R.

Using a spherical coordinate system with its origin at the center of the droplet, the mathematical formulation of the problem in terms of dimensionless variables in which the liquid density $\rho\equiv 1$, surface tension $\gamma\equiv 1$, and radius of the equivalent spherical droplet $R\equiv 1$ are taken as unity, is given by

$$\Delta\psi=0, \quad \mathbf{U}=\nabla\cdot\psi,$$

$$\Delta\Phi=0, \quad \mathbf{E}=-\nabla\cdot\Phi,$$

$$r\to\infty: \quad |\nabla\Phi|\to 0,$$

$$r=0: \quad |\nabla\Psi|<\infty,$$

$$-\frac{1}{4\pi}\oint\frac{\partial\Phi}{\partial n}dS=Q, \quad S(r,Q,\varphi)\equiv\begin{cases} r=1+\xi(\theta,t),\\ 0\leqslant Q\leqslant\pi,\\ 0\leqslant\varphi<2\pi.\end{cases}$$

$$r=1+\xi(\theta,t): \quad \Phi=\text{const},$$

$$\frac{\partial\psi}{\partial r}=\frac{\partial\xi}{\partial t}+\frac{1}{r^2}\frac{\partial\xi}{\partial\theta}\frac{\partial\psi}{\partial\theta},$$

$$\Delta\mathcal{F}-\frac{\partial\psi}{\partial t}-\frac{1}{2}(\nabla\cdot\psi)^2+\mathcal{F}_E=\mathcal{F}_\gamma, \quad \mathcal{F}_E=\frac{E^2}{8\pi},$$

$$t=0: \quad r=1+\xi_*+\varepsilon P_2(\cos(\theta)), \quad \psi=0,$$

$$\int_V dv=\frac{4}{3}\pi,$$

$$V(r,\theta,t)\equiv\begin{cases} 0\leqslant r\leqslant 1+\xi_*+\varepsilon P_2(\cos(\theta)),\\ 0\leqslant\theta\leqslant\pi, \quad 0\leqslant\varphi<2\pi.\end{cases}$$

The solution of this problem, which determines the droplet shape at any time to within terms of the second order of smallness with respect to the parameter ε, has the form:

$$\begin{aligned} r=1&-\frac{\varepsilon^2}{5}\cos^2(\omega_2 t)+\varepsilon\cos(\omega_2 t)P_2(\cos(\theta))\\ &+\frac{\varepsilon^2}{\omega_2^2}(\chi_1-(\chi_1+\chi_2)\cos(\omega_2 t)\\ &+\chi_2\cos(2\omega_2 t))P_2(\cos(\theta))+\frac{18}{35}\varepsilon^2(\chi_3-(\chi_3\\ &+\chi_4)\cos(\omega_4 t)+\chi_4\cos(2\omega_2 t))P_4(\cos(\theta)), \end{aligned} \tag{1}$$

$$\chi_1\equiv\frac{44-5W}{14}, \quad \chi_2\equiv\frac{23W-116}{42}, \quad \chi_3\equiv\frac{36-5W}{\omega_4^2},$$

$$\chi_4\equiv\frac{12+W}{4(10-W)}, \quad W\equiv\frac{Q^2}{4\pi},$$

$$\omega_2^2\equiv 2(4-W), \quad \omega_4^2\equiv 12(6-W).$$

In formula (1) the correction of the second order of smallness to the second mode of the capillary oscillations has an infinitely small denominator for $W\to 4$, $\omega_2^2\to 0$. Hence for $W=4$ it is impossible to calculate the shape of the droplet surface directly using formula (1). Interestingly, for finite t the limiting form of expression (1) for $W\to 4$ is nontrivial.

This is because $\lim_{W\to 4}\omega_2=0$ and consequently, for finite t when $W\to 4$ we have: $\cos(\omega_2 t)=1-\omega_2^2t^2/2+o(\omega_2^2t^2)$ and $\cos(2\omega_2 t)=1-2\omega_2^2t^2+o(\omega_2^2t^2)$.

Thus, for near-critical values of W the numerator of the coefficient of $P_2(\cos(\theta))$ has the same order of smallness $\sim o(\omega_2^2)$, as the denominator and this term tends to the finite value

$$\varepsilon^2t^2(\chi_1-3\chi_2)P_2(\cos(\theta))=\frac{12}{7}\varepsilon^2t^2P_2(\cos(\theta)).$$

Since no singularities occur in the other terms (1) for $W=4$, we find:

$W=4$:

$$r=1+\varepsilon P_2(\cos(\theta))-\frac{\varepsilon^2}{5}+\varepsilon^2\frac{18}{35}\sin^2(t\sqrt{6})P_4(\cos(\theta))+\frac{12}{7}\varepsilon^2t^2P_2(\cos(\theta)). \quad (2)$$

It can be seen that for $W=4$ in the linear approximation [the first two terms in formula (2)], the droplet has an elongated, nonoscillating profile. A slight increase in the parameter W above the critical value $W_c=4$ causes exponential elongation of the droplet with time. For $W<4$ the droplet oscillates stably.

Linear terms with respect to ε (2) in the small left-hand semineighborhood of $W=4$ are bounded and the correction of the first order of smallness does not exceed the principal term of the expansion for any t. This implies that the asymptotic approximation of the first order of smallness is dimensional with respect to t.

For the expansion of the second order of smallness, the small left-hand semineighborhood of $W=4$ is a region of nonuniform asymptotic expansion: for near-critical values $W\to 4$ the correction of the second order of smallness with respect to ε in formula (2) is only small compared with the preceding terms of the expansion at zero time. Within the characteristic time $t\sim o(\varepsilon^{-1/2})$ this correction becomes comparable to the preceding term of the expansion and with further increase in t, exceeds this. In accordance with general perturbation theory, this means that it is only permissible to use the expansion (2) for small $t=o(\varepsilon^{-1/2})$.

The expansion (2) cannot be transformed into a uniform expansion using a renormalization method, which can identify temporally periodic solutions of a problem. Thus, for $W=4$ the motion of the charged droplet surface cannot be periodic. Aperiodic undamped motion can be interpreted as instability.

Millimeter water droplets can be considered to have low viscosity and good conductivity.[1] For a water droplet ($\rho=1$ g/cm^3) of radius $R\sim 10^{-1}$ cm, capillary oscillations having an amplitude of the order of an angstrom, i.e., $\sim 10^{-8}$ cm have the amplitude $\varepsilon\sim 10^{-7}$ in dimensionless variables. Thus, the dimensionless time is $t\sim\varepsilon^{-1/2}\sim 3\times 10^3$. In the selected dimensionless variables the time scale unit is $t_*=((\rho R^3)/\gamma)^{1/2}\sim 4\times 10^{-3}$ s, so that the real physical time is $t_p=t\times t_*\sim 10$ s. This is the time during which the expansion (2) can be used to describe the time evolution of the surface profile after critical charge has been imparted to the droplet. It is clear from physical concepts that a critically charged droplet should be unstable. Therefore this value of t_p may be interpreted as an estimate of the time between the droplet becoming charged and the time when it begins to dump some of the charge in order to become stable. This delay in the onset of instability is caused by hydrodynamic inertia.

It should be noted that this estimate of the characteristic time for the buildup of instability of a critically charged droplet agrees with the estimate using the results of theoretical calculations[5] where a nonlinear integral equation whose solution yields an estimate similar to that given above, was derived and solved to describe the time evolution of an unstable droplet using a spherical approximation for its shape (using qualitative data from Ref. 6). Both sets of calculations made using completely different methods not only give the same numerical value of the characteristic time t_p for the buildup of instability of a critically charged droplet but the analytic dependences of t_p on the droplet radius R, liquid density ρ, and surface tension of its free boundary γ are also the same, in both cases having the form

$$t_p\sim R^2\rho^{1/2}\gamma^{-1/2}.$$

This agreement between the estimates confirms the validity of the calculations made in Ref. 5 and in the present analysis [beyond the asymptotic limits of expression (1)] and indicates that the results obtained in Ref. 6 making extensive use of qualitative reasoning are also correct.

To conclude, a millimeter water droplet carrying a charge which is critical in the sense of stability, undergoes deformation according to the law (2) within times of the order of a tenth of a second. Such a large time interval can easily be identified experimentally and the effect can be recorded. In experiments to check the Rayleigh criterion and study the breakup behavior of a highly charged droplet (see the review presented in Ref. 1 and the literature cited therein), experimenters used droplets an order of magnitude smaller and because of the inertia of the system with using electrostatic suspension of the droplet to allow free evaporation, no attention was paid to this delay. The observed delay in the breakup of a highly charged droplet may play an important role in devices using charged ion-cluster-droplet beams.

[1] A. I. Grigor'ev and S. O. Shiryaeva, Izv. Ross. Akad. Nauk Ser. Mekh. Zhidk. Gaza No. 3, 3 (1994).
[2] J. A. Tsamopoulos and R. A. Brawn, J. Fluid Mech. **147**, 373 (1984).
[3] T. G. Wang, A. V. Anilkumar, and C. P. Lee, J. Fluid Mech. **308**, 1 (1996).
[4] Lord Rayleigh (J. Strutt), Philos. Mag. **14**, 184 (1882).
[5] A. I. Grigor'ev and S. O. Shiryaeva, Zh. Tekh. Fiz. **65**(3), 39 (1995) [*sic*].
[6] A. I. Grigor'ev, Zh. Tekh. Fiz. **55**, 1272 (1985) [Sov. Phys. Tech. Phys. **30**, 736 (1985)].

Translated by R. M. Durham

Energy distributions of electrons emitted from a diamond film under the action of a strong field

S. A. Pshenichnyuk, Yu. M. Yumaguzin, and R. Z. Bakhtizin

Bashkir State University
(Submitted January 26, 1999)
Pis'ma Zh. Tekh. Fiz. **25**, 46–52 (August 12, 1999)

Results are presented of measurements of the total energy distributions of electrons emitted under the action of a strong external field from the surface of a thin diamond-like film, fabricated by ion-beam deposition on a tungsten tip. The data confirm that carriers are injected into the conduction band of the film and then emitted into vacuum. © *1999 American Institute of Physics*. [S1063-7850(99)00908-8]

The continuing interest being shown in the study of field electron emission from carbon materials derives from the unique emission properties of type IIb natural semiconducting diamond,[1] and various amorphous carbon and diamond-like films usually prepared by chemical vapor deposition.[2] It has been reliably established that the (111) surface of natural diamond exhibits negative electron affinity,[1] and also that the stability of the field emission current from the surface of metals coated with a diamond-like film is higher than for surfaces of pure metals.[3] This is because of the extremely high chemical inertia of a diamond surface and the low sputtering coefficient of carbon materials under ion bombardment.[4]

So far, however, the mechanisms responsible for the transport of carriers through a semiconducting diamond-like film under the action of a strong ($\sim 10^7$ V/cm) external emission field have not be accurately identified. Valuable information on the band structure of a diamond-like coating and the emission process may be obtained by studying the energy distributions of the emitted electrons, for which no reliable data are available. The aim of the present study is to determine the energy distributions of electrons emitted from the surface of a diamond film measured under high vacuum conditions from a local emitting section. In the present paper we report results obtained using tungsten-tip field emitters coated with a thin diamond-like film.

The tip emitters studied were prepared as follows. A thin tip having radius of curvature $\leqslant 1$ μm at the apex was fabricated from 0.08 mm diameter tungsten wire by electrochemical etching in an aqueous solution of KOH. The tip was then rinsed in distilled water, mounted on a tungsten bridge for heating, and transferred to a high-vacuum chamber to deposit the diamond film. The residual vacuum in the chamber (better than 10^{-9} Torr) was obtained using oil-free pumping systems based on a TRION NMTO-0.1-1 ion pump.

Before the film was deposited, the tip was heated in vacuum to $\sim 1500\,^{\circ}$C to remove adsorbed contaminants. The carbon film was deposited by an ion-beam deposition technique. The tip was first cleaned by bombardment with 0.5 keV C^+ ions for 5 min, the beam energy was then reduced to 100 eV, and carbon was deposited on the surface of the tip for 80 min. The ion beam current density was 0.04 μA/mm^2. The dose and time of exposure of the tip to the C^+ ions was used to estimate the thickness of the carbon film on the tungsten surface, which was ≈ 15 nm.

After the deposition process, the tip was transferred to the high-vacuum chamber to measure the energy distributions and the current–voltage characteristics of the field current. The working vacuum to study the emission properties was better than 10^{-10} Torr. In order to obtain the total energy distribution of the emitted electrons, we used a dispersion analyzer which could be tuned to a particular part of the total emission pattern. The energy distributions of the emitted electrons were measured and processed automatically using a computer (Am5×86-P75-S, 133 MHz) and CAMAC modules. The apparatus used to study the emission was described in Ref. 5.

Immediately after installing the tip and applying the emission voltage, we observed an unstable emission pattern. In order to stabilize this, the tip with the deposited film was heated to around 500°, after which the emission was stabilized but the pattern showed no signs of symmetry.

Figure 1a shows the Fowler–Nordheim characteristic of the total current for the tip with the deposited film. It can be seen that the graph exhibits the nonlinearity typical of the emission from semiconducting or insulating surfaces.[6] The total energy distribution of the emitted electrons obtained after the weak heating noted above is shown in Fig. 2a for several values of the emission voltage. A characteristic feature of this graph is that it has two peaks: the first at ≈ -4.5 eV is not displaced as the applied voltage varies, which is typical of the energy distributions for pure metal tips. As an example Fig. 2b shows the energy distribution obtained for a tungsten tip not coated with a film. Thus, this high-energy peak may be ascribed to electrons which tunnel through the thin diamond film into vacuum from the Fermi level of the metal, which is also confirmed by the position of this peak and its half-width.

The broad peak having a maximum at around -5.9 eV can be ascribed to the diamond-like film. Its width is probably determined by the fact that for this particular coating

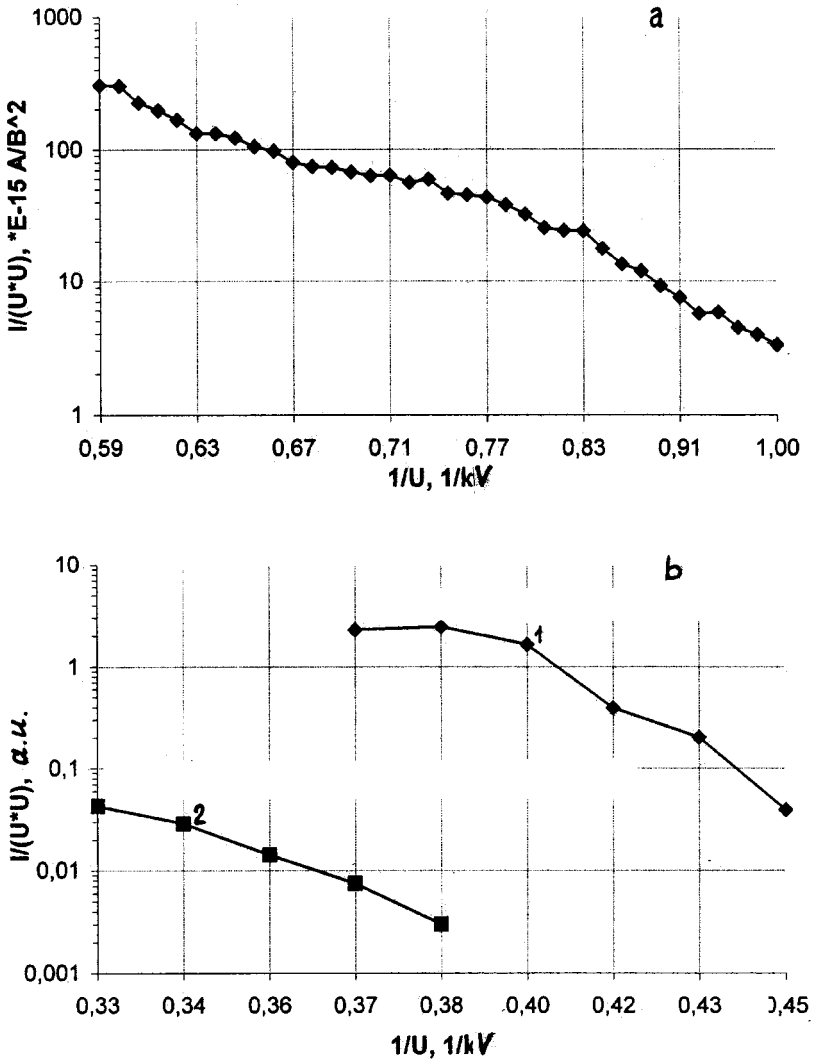

FIG. 1. Fowler–Nordheim characteristics: a — total current from tungsten tip with diamond film, b — tungsten tip before (*1*) and after (*2*) evaporation of diamond film, measured for a small section.

thickness and the existence of a high emission voltage at the surface, the field penetrates completely into the film, causing tilting of the energy bands over the entire thickness of the film. When emission takes place from the conduction band of the carbon layer, the width of the spectrum increases with increasing applied field since the tilt of the bands increases, as is observed experimentally (Fig. 2a). This peak also shifts appreciably as the emission voltage varies, which is typical of semiconductor emitters. The observed fine structure of the broad peak in the spectra may be attributable to emission from electronic states associated with structural defects in the diamond film.[7]

The emitting tip was then heated to 1300 °C to remove the deposited coating. The energy distribution then obtained is shown in Fig. 2b. It can be seen that the half-width, position, and only slight shift of the peak with increasing emission voltage are consistent with metal behavior. The broad peak ascribed to the film has completely disappeared. The Fowler–Nordheim characteristic (Fig. 1b) obtained from the same small section as the energy distribution, also indicates that the carbon film has been removed. Note that after the tip was heated, the emission voltage increased. Assuming that the geometric profile of the tip remains constant because of the low heating temperature compared with the melting point of tungsten, we can postulate that the work function of the field emitter surface decreases when it is covered with a diamond film.

It is interesting to note that after the carbon film was removed, the emission pattern acquired symmetry which does not, however, correspond to the generally accepted image of a ''smoothed'' pure tungsten tip. A similar image, described in Ref. 8 as ''ribbed'' or ''dirty carbon'' is consistent with a tungsten tip with adsorbed vapor of high-vacuum oil formed as a result of using oil-vapor pumps, as in Ref. 8. Thus, in this case a certain amount of carbon remains on the tip and does not evaporate at fairly high temperatures (up to 2500 °C) and applied fields, as was noted in Ref. 8.

To conclude, we have fabricated field emission cathodes consisting of a tungsten tip coated with a diamond-like film obtained by an ion-beam deposition method. Measurements of the energy distributions and current–voltage characteristics have shown that a thin semiconducting layer exists on the surface which reduces the emitter work function and increases the stability of the emission. This layer can only be

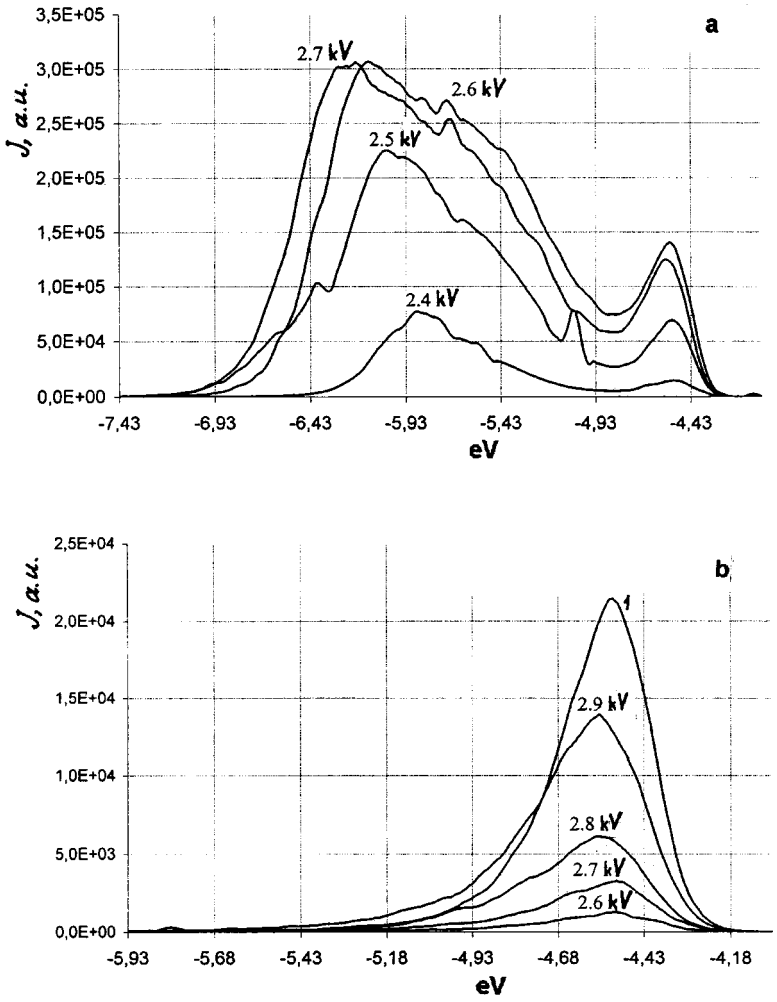

FIG. 2. Energy distributions of field emission electrons: a — emitted from a tip coated with a diamond film, obtained at various emission voltages; b — after evaporation of the film at various emission voltages (the spectrum for a pure tungsten tip (*1*) is given for comparison.)

removed at high temperature or by ''stripping'' the tip, although a small fraction of carbon remains on the surface.

[1] F. J. Himpsel, J. A. Knapp, J. A. Van Vechten *et al.*, Phys. Rev. B **20**, 624 (1979).
[2] W. Zhu, G. P. Kochanski, S. Jin, and L. Seibles, J. Vac. Sci. Technol. B **14**, 2011 (1996).
[3] W. B. Choi, J. Liu, M. T. McClure *et al.*, J. Vac. Sci. Technol. B **14**, 2050 (1996).
[4] V. S. Vavilov, A. A. Gippius, and E. A. Konorova, *Electronic and Optical Processes in Diamond* [in Russian], Nauka, Moscow (1985), 120 pp.
[5] R. Z. Bakhtizin, V. M. Lobanov, and Yu. M. Yumaguzin, Prib. Tekh. Éksp. No. 4, 246 (1987).
[6] A. A. Dadykin, A. G. Naumovets, V. D. Andreev *et al.*, Diamond Relat. Mater. No. 5, 771 (1996).
[7] S. Yoshiyki, M. Fumihiko, H. Masaharu *et al.*, J. Appl. Phys. **84**, 6351 (1998).
[8] A. P. Komar and Yu. N. Talanin, Izv. Akad. Nauk SSSR, Ser. Fiz. **20**, 1137 (1956).

Translated by R. M. Durham

Investigation of profiles of implanted Ti atoms over the depth of boron nitride nanocrystalline ceramic exposed to high radiation doses and fluxes with subsequent annealing

S. M. Duvanov and V. A. Baturin

Institute of Applied Physics, National Academy of Sciences of Ukraine, Sumy
(Submitted February 11, 1999)
Pis'ma Zh. Tekh. Fiz. **25**, 53–57 (August 12, 1999)

Results are presented of an investigation of distribution profiles of implanted Ti atoms at high implantation doses (fluence around $10^{17}\,\mathrm{cm}^{-2}$) over the depth of boron nitride (BN) nanocrystalline ceramic. It is observed that the concentration maxima of implanted impurities are shifted into the substrate under post-implantation annealing in vacuum at 950 °C. This behavior of the implanted impurities in BN is directly the opposite of that observed in earlier studies of polycrystalline aluminum oxide ceramic exposed to similar ion thermal treatment. The effective diffusion coefficient of titanium atoms in BN under thermal annealing is estimated. The Ti/O concentration ratio in the layer modified as a result of implantation and subsequent annealing at 950 °C is close to stoichiometric TiO_2. A simultaneous increase in the concentration of carbon and nitrogen atoms in the surface layers of BN samples was observed as a result of annealing at 830 and 950 °C.
[S1063-7850(99)01008-3]

High-dose, high-current implantation of multiply charged ions is a powerful method of modifying the initial structure of solids to form a state having a high concentration of defects and new metastable phases. Here, high-dose, high-intensity implantation is taken to mean implantation when the ion current density on the target is between a few and tens of milliamperes and the implanted impurity concentration is between a few and tens of atom percent. It is interesting to use this method to modify pyrolytic boron nitride (BN) ceramic because of the possibility of forming thermally stable, electrically conducting coatings[1] and compounds such as hard cubic boron nitride *c*-BN and the theoretically predicted superhard compound β-C_3N_4 (Ref. 2).

Prepolished samples of nanocrystalline ceramic (hexagonal prisms between 50 and 200 nm) were implanted with titanium ions and then annealed in vacuum. The implantation parameters were as follows: implantation energy 50–150 keV, pulsed ion current density 10^{-2}–$10^{-3}\,\mathrm{A/cm}^2$, pulse duration 250 μs, pulse repetition frequency $10-50\,\mathrm{s}^{-1}$, ion charge state $Ti^+ = 3\%$, $Ti^{++} = 80\%$, $Ti^{+++} = 17\%$, residual gas pressure in chamber 5×10^{-3} Pa, and fluence around $10^{17}\,\mathrm{cm}^{-2}$ (Ref. 1). The samples were annealed at 400, 830, and 950 °C using the apparatus described in Ref. 3. The annealing time was around 30 min. The concentration of the main elements forming the initial BN samples was determined by backscattering of helium ions. The composition of the BN ceramic is: 37 at.% B, 37 at.% N, 10 at.% C, and 5 at.% O.

The following set of complementary nondestructive methods was used to make a quantitative elemental analysis of the modified ceramic samples: Rutherford backscattering (RBS) of $^4He^+$ and $^1H^+$ ions, resonant elastic scattering of $^4He^+$ and $^1H^+$ ions, proton elastic recoil detection (ERD),[4] and scanning electron microscopy with energy-dispersive x-ray spectroscopy (SEM EDX). In order to enhance the sensitivity of analyzing the concentration of light elements, we used elastic and resonant elastic scattering of protons at B, C, N, and O isotopes.

The aim of the present study was to investigate profiles of implanted ions at high implantation doses and to determine the diffusion coefficient as a result of subsequent thermal annealing in vacuum.

The results of an SEM EDX analysis of the light elements (B, C, N) shows (Fig. 1) that the carbon peak on the EDX spectrum, measured for a sample implanted at room temperature, is approximately three times the intensity of the peak on the same spectrum for a sample which has undergone subsequent annealing at 830 °C. This indicates that carbon diffuses toward the surface of the sample as a result of annealing. This redistribution of the carbon atoms agrees with the results of measuring the depth concentration profiles of H, N, C, O, and Ti for the same samples by RBS and ERD. An ERD analysis showed that the surface layer of a sample 35 nm thick implanted at room temperature is enriched in hydrogen atoms. Subsequent annealing at 830 °C reduces the initial hydrogen concentration approximately 1.5 times.

An RBS analysis of the samples shows (Fig. 2) that the implanted titanium atoms are redistributed inside a sample which has undergone post-implantation thermal annealing at 950 °C. However, the distribution profile of the Ti concentration over the depth of the same sample annealed at 400

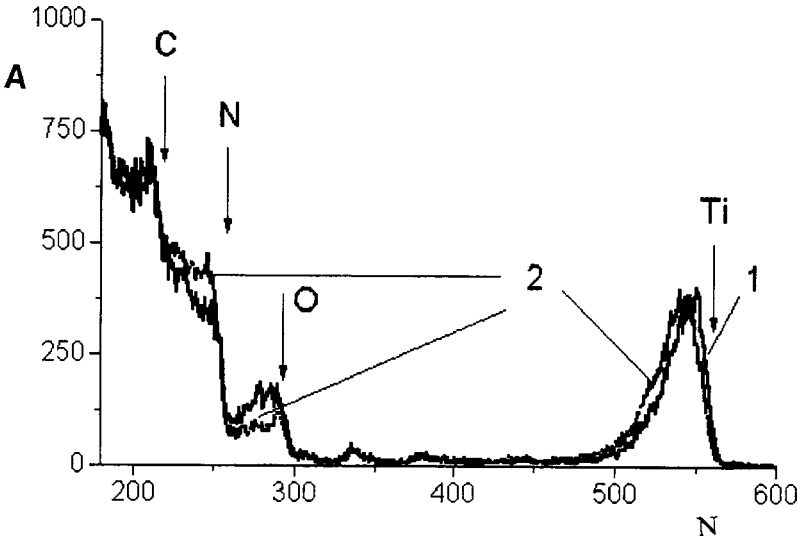

FIG. 1. Energy spectra of backscattered helium-4 ions having an initial energy of 2 MeV measured for BN samples implanted with Ti ions with a fluence of $10^{17}\,cm^{-2}$ and annealed at 400 (*1*) and 950 °C (*2*). The arrows indicate the kinematic boundaries of the spectra for the various elements: N — channel number, A — normalized output

and 830 °C differs negligibly from the profile measured for the nonannealed sample. Redistribution of the implanted Ti takes place in a fairly narrow temperature range between 830 and 950 °C. The effective titanium diffusion coefficient extracted from the experimental concentration profiles was around $8.5\times10^{-14}\,cm^2/s$ in the temperature range 830–950 °C. The distribution of implanted impurities in the BN samples is the opposite of our earlier result[1] where we observed that implanted titanium atoms migrated toward the surface of polycrystalline aluminum oxide (Al_2O_3) ceramic samples. These Al_2O_3 samples were exposed to similar ion thermal treatment.

The coefficient of Ti diffusion in BN suggests that the migration of the titanium atoms correlates with the migration of implantation-induced defects and is similar to radiation-enhanced diffusion.

Thus, we have obtained the following main results:

We observed that implanted titanium atoms in a BN sample are redistributed as a result of subsequent annealing at 950 °C;

We identified a narrow range of annealing temperatures 830–950 °C where redistribution of implanted atoms is observed;

The Ti/O concentration ratio in the layer modified as a result of implantation and subsequent annealing at 950 °C is close to stoichiometric TiO_2, which indicates that titanium dioxide is formed;

We observed a simultaneous increase in the concentration of carbon and nitrogen atoms in the surface layers of BN samples as a result of annealing at 830 and 950 °C;

The effective diffusion coefficient of implanted titanium was around $8.5\times10^{-14}\,cm^2/s$.

The authors are grateful to A. V. Kabyshev for assis-

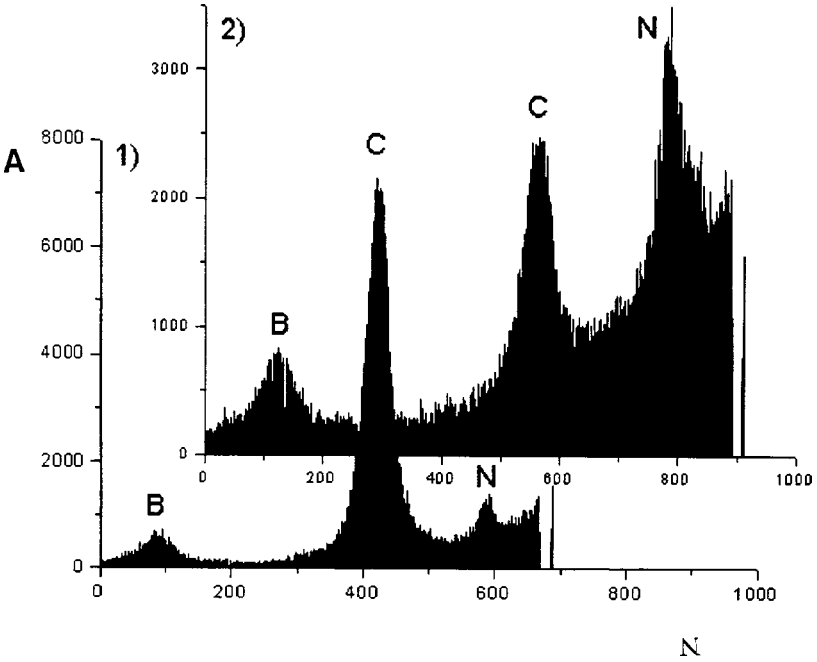

FIG. 2. EDX spectra of BN ceramic samples implanted with Ti ions at room temperature (*1*) and after annealing at 830° C for 30 min (*2*).

tance with preparing the samples and A. P. Kobzev for helping with the ion beam analysis.

This work was partly supported by the Ukraine Scientific Technological Center, Project No. 109.

[1] S. M. Duvanov, A. V. Kabyshev, and A. P. Kobzev, Mater. Sci. Forum **248**, 271 (1997).

[2] K. M. Yu, M. L. Cohen, E. E. Haller, V. L. Hansen, A. I. Liu, and I. C. Wu, Phys. Rev. B **49**, 5034 (1994).

[3] O. I. Buzhinskiĭ, V. A. Butenko, and V. V. Lopatin, Prib. Tekh. Éksp. No. 3, 236 (1981).

[4] S. M. Duvanov, A. P. Kobzev, A. M. Tolopa, and D. M. Shirokov, Nucl. Instrum. Methods Phys. Res. B **85**, 264 (1994).

Translated by R. M. Durham

Investigation of the entrainment of silicon atoms by ''vacancies'' formed in an aluminum melt when its surface is exposed to an ion–electron flux

V. A. Kolpakov and A. I. Kolpakov

Samara State Aerospace University
(Submitted March 26, 1998; resubmitted March 17, 1999)
Pis'ma Zh. Tekh. Fiz. **25**, 58–65 (August 12, 1999)

It is established that when a liquid-aluminum–silicon (Al–Si) structure is bombarded with ions and electrons having energies up to 6 keV, the process of Si dissolution in the aluminum is slowed. Mechanisms are put forward for the formation of an excess concentration of atomic-size voids (''vacancies''), the formation of a vacancy flux normal to the Si surface, and entrainment of impurity atoms by this flux. It is shown experimentally that zones completely free from Si atoms, where the silicon exhibits maximum solubility, in the aluminum may be formed in the bulk of the aluminum melt. The size of these zones can easily be controlled by the parameters of the ion–electron flux. © *1999 American Institute of Physics.*
[S1063-7850(99)01108-8]

In studies of the mechanisms for the dissolution of semiconductors in the liquid phase of metals, the problem arises of controlling the parameters of the diffusion process of the semiconductor atoms in the bulk of the melt. At present, no methods are available for correcting the melting regimes directly during the technological process. This problem can be solved by using a high-voltage discharge as the energy source, which has the distinguishing feature that fluxes of electrons and negative ions are formed almost independently of the gas-discharge device.[1]

A liquid-phase metal can be treated as a highly elongated body which retains the structure of a solid near the melting point.[2] Then, despite its instability, this structure can contain around 1% atomic-size voids which, like vacant sites in semiconductors, are called[2] ''vacancies'' and have an activation energy of the order of 0.93–1.2 eV (Ref. 3).

If the average velocity of the thermal motion of the liquid-metal atoms is many times lower than the velocity of the charged particles in the ion–electron flux,[4] the times taken for the establishment of the thermal regime in the melt and the annealing are 0.2 s (Ref. 5) and 2–20 s, respectively, so that a liquid-metal atom can justifiably be considered to be fixed relative to a charged particle, and convection processes can be neglected.[6] In the present study both conditions are satisfied and thus the Fick second-order equation can be used for the calculations.[7]

The samples were silicon–aluminum (Si–Al) structures consisting of KÉF-32 grade silicon and chemically pure aluminum. The structures were annealed using an electron–ion beam having a particle energy up to 6 keV, a cross-section diameter of 50 mm, and current up to 30 mA. The working gas was air. The uniformity of the particle energy distribution over the cross section was better than 98% and the electron and ion concentrations were $0.3\times10^{20}\,\mathrm{cm}^{-3}$ (Ref. 8) and $0.3\times10^{15}\,\mathrm{cm}^{-3}$ (Ref. 9), respectively.

The Al temperature was determined using a Promin' micropyrometer, the Si content in the Al was determined by weighing and using an MAR-2 x-ray microanalyzer, the resistivity was measured using a TsIUS-2 device, and the conductivity of the structure layers was determined from the magnitude and sign of the thermo-emf. The distribution of the Si atoms in Al was determined by a metallographic analysis of cross sections of the samples.

According to Kireev,[4] the average energy imparted to an aluminum atom by an electron is 0.23 eV and that imparted by an oxygen ion is 6.8 keV, which is quite sufficient to form vacancies.

Taking into account the energies of the oxygen ions and electrons imparted by them to the Al, and using Refs. 10 and 11, we can determine the vacancy concentration as $1\times10^{19}\,\mathrm{cm}^{-3}$. This is more than an order of magnitude higher than the vacancy concentration formed under the action of a purely thermal field ($1.6\times10^{18}\,\mathrm{cm}^{-3}$). From this it follows that a vacancy gradient forms in the Al surface layer,

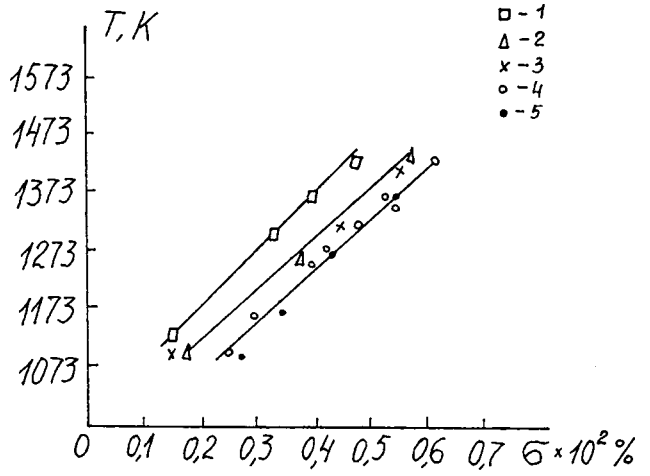

FIG. 1. Variation of Si solubility as a function of temperature for various durations of ion–electron irradiation: *1* — 2 s, *2* — 40 s, *3* — 60 s, *4* — 90 s, *5* — solubility determined from phase diagram $I=3$–30 mA, $U=6$ kV).

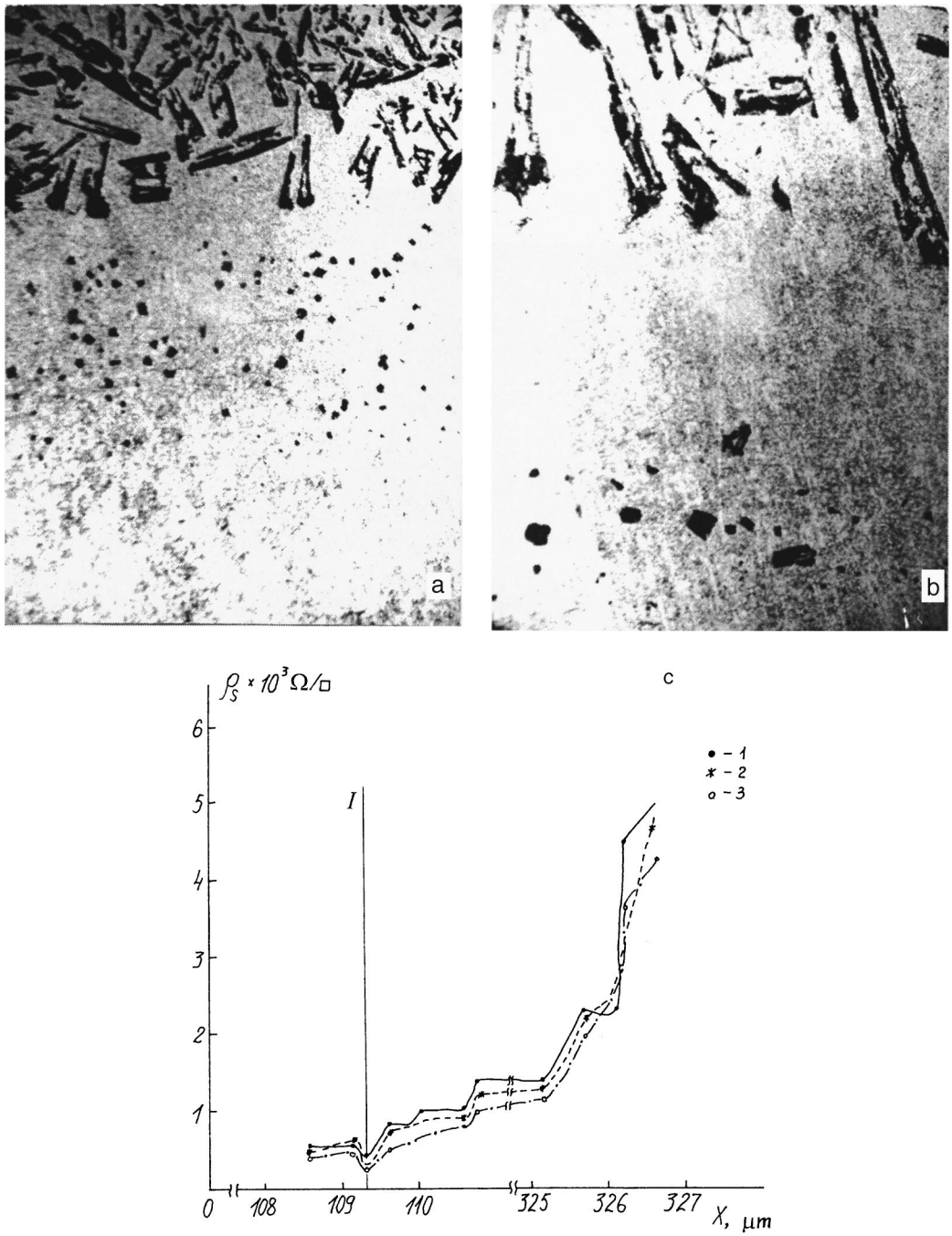

FIG. 2. Distribution of Si atoms in Al after ion–electron bombardment with a current $I=2.8$ mA, accelerating voltage $U=3.6$ kV, and initial Al layer thickness $h=3$ mm: a — beginning of motion of Si layer dissolved in melt distorted by mechanical treatment ($t=2$ s), b — time of motion of the layer of surface Si atoms in the middle of the Al layer ($t=3$ s), c — distribution of resistivity over sample profile: *1* — 5 element series, *2* — 7 element series, *3* — 10 element series, *I* — Al–Si interface.

whose concentration corresponds to the particle concentration in the ion–plasma flux.

When the Al–Si structure is annealed by an ion–electron beam, a temperature gradient of 70–35°C forms between the layers in the range 1053–1388 K. The existence of these two gradients leads to the formation of a vacancy flux in the direction of the Si surface. Bearing in mind the vacancy mechanism of diffusion, we can predict that Si atoms will be entrained by the vacancy flux.

If we only use the vacancy concentration gradient to determine the duration of the saturation of the melt by Si atoms to the saturation level in the Fick equation, we observe that in this case, the durations of saturation for melting in a uniform thermal field (t_1) and under ion–electron bombardment (t_2) are $t_1=14\times10^{-6}$ s and $t_2=90$ s. An analysis of these facts indicates that in the first case, the Si atoms entering the melt reach its surface almost instantaneously. This makes it impossible to control the melting process, which agrees with known data.[12]

In the second case, the Si atoms are entrained by vacancies, which leads to slowing of the diffusion process and the solubility of Si (σ_{Si}) in liquid Al becomes dependent on the

irradiation time (Fig. 1). An analysis of this dependence shows that for irradiation times <90 s, the value of σ_{Si} is lower than that calculated from the phase diagram of Al–Si. The maximum difference between these values is observed at $t=2$ s, i.e., when the front of Si atoms is located in the melt, as shown in Fig. 2a. From this time onward, it is possible to regulate the quantity of Si in the melt by varying the surface irradiation regime.

However, if entrainment occurs, the solidification of Si in the irradiation zone should follow different laws to that outside this zone. In fact, an image of an oblique polished section of the melt shown in Fig. 2b suggests that the dendritic Si ribbons near the surface in the irradiation zone are predominantly directed almost normal to the Si surface, whereas at the beginning of dissolution (Fig. 2a) they are distributed randomly. The departure from the normal is evidently caused by the thermal motion during the Al solidification process whose duration did not exceed 1–2 s.

The Si atoms in the surface region are weakly bound to the crystal structure and thus have a considerably higher rate of dissolution in liquid metals. On entering a vacancy region, an Si atom begins to be reflected from its inner surface, being delayed in the vacancy region for some time, during which it can become displaced with the vacancy toward the Si surface. On its path the vacancy–Si structure encounters Si atoms and free vacancies. These readily interact to form Si atom complexes and the expansion of the vacancy region, i.e., the vacancy rapidly stimulates saturation of the melt with Si atoms. This gives rise to some characteristic features of the entrainment effect: we only obtain an Al melt with a maximum Si content and it is possible to obtain melt zones completely free from semiconductor atoms (Fig. 2b). This advantage fully explains the mechanism for obtaining Ohmic contacts in Ref. 13. In addition, the linearity of the fronts of surface atoms dissolved in the melt and the Si bulk indicates that the vacancies are distributed uniformly over the flux cross section, which is clearly attributable to the uniform particle distribution over the cross section of the ion–electron beam.

Figure 2c shows the distribution of the resistivity over the sample profile. Some increase in the resistivity in the range $x=0$–$109.15\ \mu$m is caused by the formation of a layer of Si and Al solid solution, formed by atoms of the surface layer of the silicon substrate. A chemical analysis of the structure showed that this layer could only be removed by using a mixture of nitric and hydrofluoric acids, which suggests that it has semiconducting properties. This is also indicated by a severalfold increase in the amplitude of the thermo-emf and a change in its sign compared with similar values for the initial aluminum film. The considerably higher Si content in this zone can only be explained by the high concentration of atomic-size voids, in which several Si atoms can accumulate, and by the formation of bonds between them. This process undoubtedly involves trapping of Al atoms, which leads to the formation of an Al–Si solid solution. At high concentrations of these complexes or even when they merge, the vacancy generation process ceases and the subsequent growth of the layer thickness is accomplished by the diffusion of Si atoms through the liquid Al layer caused by the temperature gradient in the Al–Si structure and the thermal motion of the atoms. Ultimately this may result in the formation of a continuous layer having semiconducting properties. When this layer was removed, we observed a shiny layer of metallic Al ($x = 109.15$–$109.3\ \mu$m) which could be removed using hot sulfuric acid. It should be noted that in similar investigations of an Au–Si structure, this layer was gold-colored and could be removed using aqua regia etchant.

Abruptly heating and cooling the structure leads to an exponential increase in the dislocation concentration in the Si crystal from $5\times10^5\ \mathrm{cm}^{-2}$ at the $3.27\ \mu$m boundary until these merge near the metal–semiconductor interface ($x = 109.3\ \mu$m) to form dislocation loops and ribbons, where the thickness of this layer did not exceed 0.5–0.8 μm. The formation of Cotrell clouds can explain the low resistivity in the range $x = 109.3$–$109.6\ \mu$m (Fig. 2c). The dislocations are bulk-type defects as they move in the irradiation zone and can thus transfer Al atoms to appreciable distances ($X = 109.3$–$326.6\ \mu$m).

To sum up, when an Al–Si structure is bombarded with low-energy particles, an effect involving entrainment of semiconductor atoms by a vacancy flux occurs in the liquid metal, and the parameters of this effect can easily be controlled by varying the electron–ion irradiation regimes of the melt surface.

[1] A. N. Komov, A. I. Kolpakov, and N. I. Bondareva, Prib. Tekh. Éksp. No. 5, 218 (1984).
[2] J. Frenkel, *Kinetic Theory of Liquids* [Clarendon Press, Oxford, 1946; Nauka, Leningrad, 1975, pp. 380, 381, 390].
[3] Ya. I. Frenkel', *Introduction to the Theory of Metals* [in Russian], Nauka, Leningrad (1972), 250. pp.
[4] P. S. Kireev, *Semiconductor Physics* [in Russian], Vysshaya Shkola, Moscow (1975), pp.175–180.
[5] N. N. Rykalin, I. V. Zuev, and A. A. Uglov, *Principles of Electron-Beam Treatment of Metals* [in Russian], Mashinostroenie, Moscow (1978), 239 pp.
[6] V. V. Yudin, Élektron. Obrab. Mater. No. 3(33), 27 (1977).
[7] B. I. Boltaks, *Diffusion and Point Defects in Semiconductors* [in Russian], Nauka, Leningrad (1972), 379 pp.
[8] V. S. Vavilov, A. E. Kiev, and O. R. Niyazova, *Mechanisms for Formation and Migration of Defects in Semiconductors* [in Russian], Nauka, Moscow (1981), 368 pp.
[9] K. A. Valiev and V. A. Rakov, *Physical Principles of Submicron Lithography in Microelectronics* [in Russian], Radio i Svyaz', Moscow (1984), 350 pp.
[10] *Handbook of Chemistry*, Vol. 1 [in Russian], Khimiya, Moscow (1966), 1071 pp.
[11] *Physical Encyclopedic Dictionary*, Vol. 2 [in Russian], Sov. Éntsiklopediya, Moscow (1962), 608 pp.
[12] A. I. Kurnosov and V. V. Yudin, *Fabrication Technology for Semiconductor Devices* [in Russian], Vysshaya Shkola, Moscow (1974), 400 pp.
[13] A. N. Komov, A. I. Kolpakov, and B. D. Rafaevich, Élektron. Tekh. Ser. 7, **5**(96), 7 (1979).

Translated by R. M. Durham

Change in the properties of BT-23 titanium alloy induced by implantation of iron and zirconium ions followed by exposure to a low-energy high-current electron beam

E. A. Bazyl', A. D. Pogrebnyak, B. P. Gritsenko, S. V. Sokolov, V. V. Staĭko, N. V. Sviridenko, and S. N. Bratushka

Sumy State University, Ukraine
(Submitted April 13, 1999)
Pis'ma Zh. Tekh. Fiz. **25**, 66–73 (August 12, 1999)

Atomic physics methods, atomic force microscopy, and testing of microhardness, wear resistance, and friction coefficient were used to investigate Ti_{41}–V_{41}–Al_{18} samples implanted with iron (60 kV) and zirconium (40 kV) ions, and then exposed to a high-current electron beam with energy fluxes of 2.7 and 5.5 J/cm^2. The maximum concentration of iron ions is 16.5 at.% at a depth of 85 nm and that of zirconium ions 0.85 at.% at 56 nm. After double implantation, the friction coefficient decreases and the wear resistance increases. After implantation and high-current electron beam treatment, the depth of the hardened layer and the wear resistance increase. © *1999 American Institute of Physics.* [S1063-7850(99)01208-2]

Promising methods of treating the surface of components made of fire-resistant materials operated under high cyclic loading, elevated temperature, abrasive wear, and so on, are ion implantation[1–5] and treatment with high-current electron beams.[6–11] These treatments can substantially improve various characteristics of components made of steels, titanium alloys, and other materials such as the fatigue limit, fire resistance, resistance to salt corrosion, electrical erosion resistance, and so on.[1,5,10,11] Ion implantation,[12] high-current electron beam treatment,[11] or high-power ion beam bombardment[10] are mainly used separately for this treatment. It should be noted that a considerable number of studies have been made of the ion implantation of titanium alloys[1,5,10,11] and high-current electron beam treatment, but double implantation of iron and zirconium ions followed by high-current electron beam treatment has only been used in the present study. The aim of the present study was to make an experimental investigation of the physicomechanical properties of Ti_{41}–V_{41}–Al_{18} after double ''duplex'' treatment[9] (implantation of iron and zirconium alloys followed by exposure to a low-energy, high-current electron beam).

For the investigations we used samples of BT-23 titanium alloy measuring $22\times18\times2$ mm having polished surfaces. Ion implantation was carried out using a Diana-4 vacuum-arc implanter at $E=60$ kV for the iron ions and $E=40$ kV for the zirconium ions, with a pulse duration around 200 μs and a pulse repetition frequency of 50 Hz. The low-energy, high-current electron beam irradiation was provided by a Nadezhda-2 accelerator with beam parameters: $E_{at}=10$–20 keV, $j=10^2$–2×10^3 A/cm^2, pulse duration between 2 and 4 μs, in a vacuum of 10^{-5} Torr. The concentration profiles of the iron and zirconium ions were analyzed by Rutherford backscattering of 2 MeV helium ions. The concentration profiles of the carbon and oxygen ions were obtained using proton elastic resonance (1.744 MeV) and the elastic resonance of the $^{16}O(^{+4}He, ^{+4}He)^{16}O$ reaction at around 3.045 MeV. The surface inhomogeneities formed as a result of low-energy, high-current electron beam treatment and ion implantation were measured using an atomic force microscope. The wear resistance was determined by an abrasion test (ball–disk system) at frequency 7.2 Hz and 2.2 N load which is described in greater detail in Ref. 3. The microhardness was measured using a Knoop pyramid nanoindentor at a load of 100 g.

All the implantation regimes and irradiation parameters are given in Table I. Figure 1a shows the Rutherford backscattering spectrum measured for a Ti_{41}–V_{41}–Al_{18} sample implanted with iron and zirconium ions. The right-hand side of the spectrum clearly shows an iron peak and a zirconium peak. An additional analysis made using nuclear-reaction elastic resonance and proton elastic resonance revealed the profiles of the oxygen and carbon atoms in the surface layer (Fig. 1b). We know that in high-dose, high-intensity implantation (in the pulsed regime) the sputtering of the surface increases substantially as the atomic number and atomic mass of the implanted ion increase.[1,2] As a result of the implantation (incident iron ion dose 5×10^{17} cm^{-2}) the maximum iron concentration is only 16.5 at.% and the maximum zirconium concentration around 0.85 at.% (incident zirconium ion dose 5×10^{16} cm^{-2}). In addition to the implanted impurities, carbon atoms are implanted in the surface layer from the residual atmosphere of the implanter chamber, their

TABLE I. Parameters for implantation and electron beam irradiation of Ti_{41}–V_{41}–Al_{18} titanium alloy (irradiation time 200 μs, one pulse).

No.	Dose, cm^2 Fe	Dose, cm^2 Zr	E, kV Fe	E, kV Zr	Ion current density, mA/cm^2	Energy density W, J/cm^2	E_{at}, keV	τ_{pulse}, μS
1	8×10^{16}	5×10^{16}	60	40	1.8	2.7	10–15	4
2	1×10^{17}	5×10^{16}	60	40	2.2	5	10–18	4
3	5×10^{17}	5×10^{16}	60	40	3.5	5	10–20	2.5

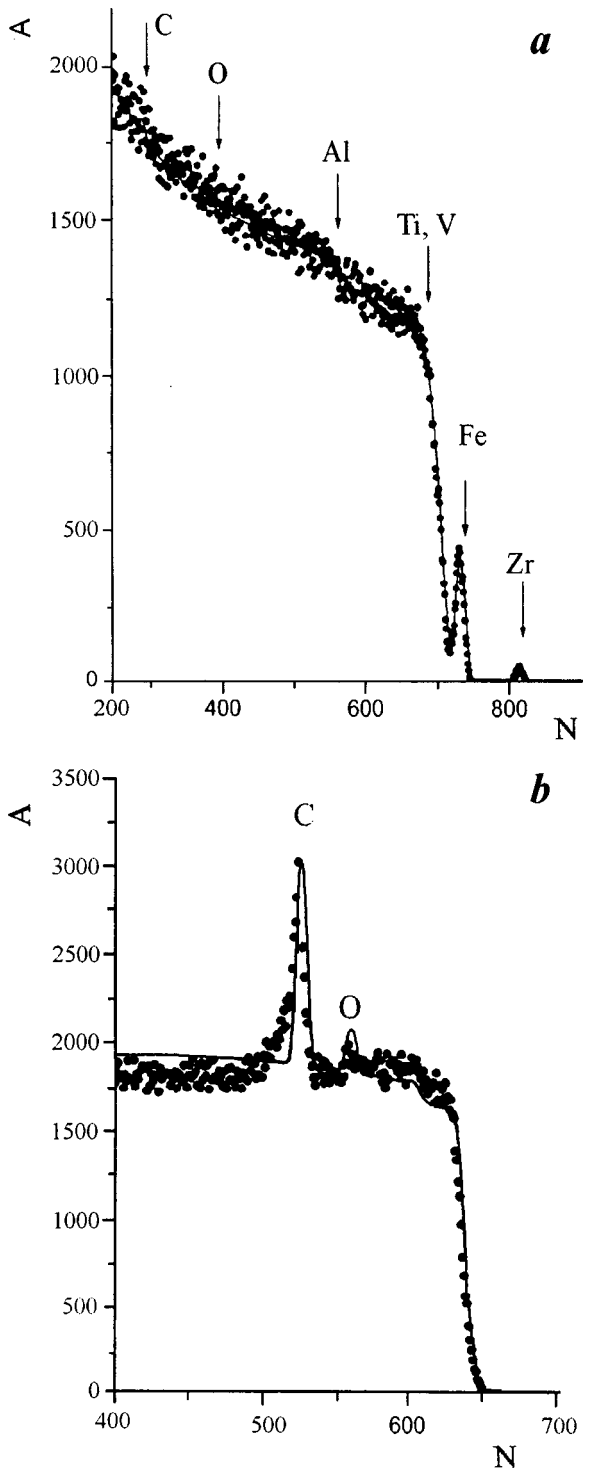

FIG. 1. a — Rutherford backscattering energy spectrum obtained using 2.430 MeV He^{+4} for a Ti–V–Al samples after implanting a 5×10^{17} cm^{-2} dose of iron ions (60 keV) and a 5×10^{17} cm^{-2} dose of zirconium ions (40 kV); b — energy spectrum obtained by the proton elastic resonance method at $E_p=1.744$ MeV to determine the carbon concentration: N — channel number, A — count.

maximum concentration being around 36 at.%. The concentration of oxygen atoms decreases since the oxide film acts as a protective shield for the penetration of carbon into the surface layer and for sputtering of the substrate material. For instance, when a 5×10^{16} cm^{-2} dose of iron ions is implanted, the oxygen concentration near the surface (around 30 nm) is approximately 2.5 at.% whereas for a 1×10^{17} cm^{-2} dose at the same depth, this concentration is around 1.4 at.%. Exposure of the Ti–V–Al samples after iron and zirconium implantation to a 5.5 J/cm^2 low-energy high-current electron beam leads to melting of a surface layer up to 3.5 μm thick[8,10] and partial evaporation of a surface layer of a few tens of nanometers. As a result of this treatment, the size of the inhomogeneities increases to 200–220 nm (Fig. 2a), iron and zirconium become redistributed in the surface layer (i.e., their peak concentration drops), and the concentration of carbon and oxygen increases at large depths (almost up to 400 nm).

Measurements of the wear resistance of the samples under nonlubricated friction after double implantation (Fig. 2b, curve *2*) show a slight reduction in the wear. However, after exposure to the low-energy high-current electron beam, the wear resistance increases abruptly (curve *3*) despite an increase in the surface roughness. Testing to measure the friction coefficient showed that after double ion implantation (iron ion dose 5×10^{17} cm^{-2} and zirconium ion dose 5×10^{16} cm^{-2}) the friction coefficient is reduced more than 1.8 times. After low-energy high-current electron beam treatment, the friction coefficient increases but is lower than that in the initial state. Measurements of the microhardness using a nanoindentor (100 g load) revealed an increase in the microhardness to 7 GPa at a depth of 180 nm, which is twice the depth of the ion range. Subsequent low-energy, high-current electron beam treatment (5.5 J/cm^2) leads to an even greater increase in the hardness (to almost 9 GPa) and the depth of the hardened layer is increased to at least 500 nm. However, the microhardness maximum is shifted into the hardened layer. We can postulate that the double implantation of iron and zirconium ions leads to the formation of Fe–Ti–C which reduces the friction coefficient and increases the wear resistance.[13–15] It was shown in these studies that implantation of Ti and Ti + C into iron and steel leads to the formation of Ti_2C and TiC carbides and the Fe_2Ti phase, which is inclined to amorphization.

To sum up, implantation of iron and zirconium ions improves the operating characteristics of BT-23 alloy such as wear resistance, friction coefficient, and hardness. Subsequent exposure to a low-energy, high-current electron beam at 5.5 J/cm^2 increases the depth of the hardened layer and the friction coefficient.

This work was partly financed by the Ukraine Ministry of Science and Technology (Raduga Project 7.5.4/73–93; 005K/95) and by the Department of Electrical Engineering of Nagaoka University of Technology, Nagaoka, Japan.

The authors thank Professor K. Yatsui and A. P. Kobzev for assistance with the experiments.

[1] J. K. Hirvonen, *Ion Implantation in Metals* [Russ. transl.], Metallurgiya, Moscow (1985), 456 pp.
[2] A. D. Pogrebnjak and A. M. Tolopa, Nucl. Instrum. Methods Phys. Res. B **52**, 25 (1990).
[3] A. D. Pogrebnjak, O. G. Bakharev, A. V. Martynenko *et al.*, Nucl. Instrum. Methods Phys. Res. B **94**, 81 (1994).
[4] V. I. Lavrentiev and A. D. Pogrebnjak, Surf. Coat. Technol. **99**, 24 (1998).
[5] J. M. Poate, G. Foti, and D. C. Jacobson, *Surface Modification and Alloying by Laser, Ion and Electron Beams* (Plenum Press, New York, 1983).

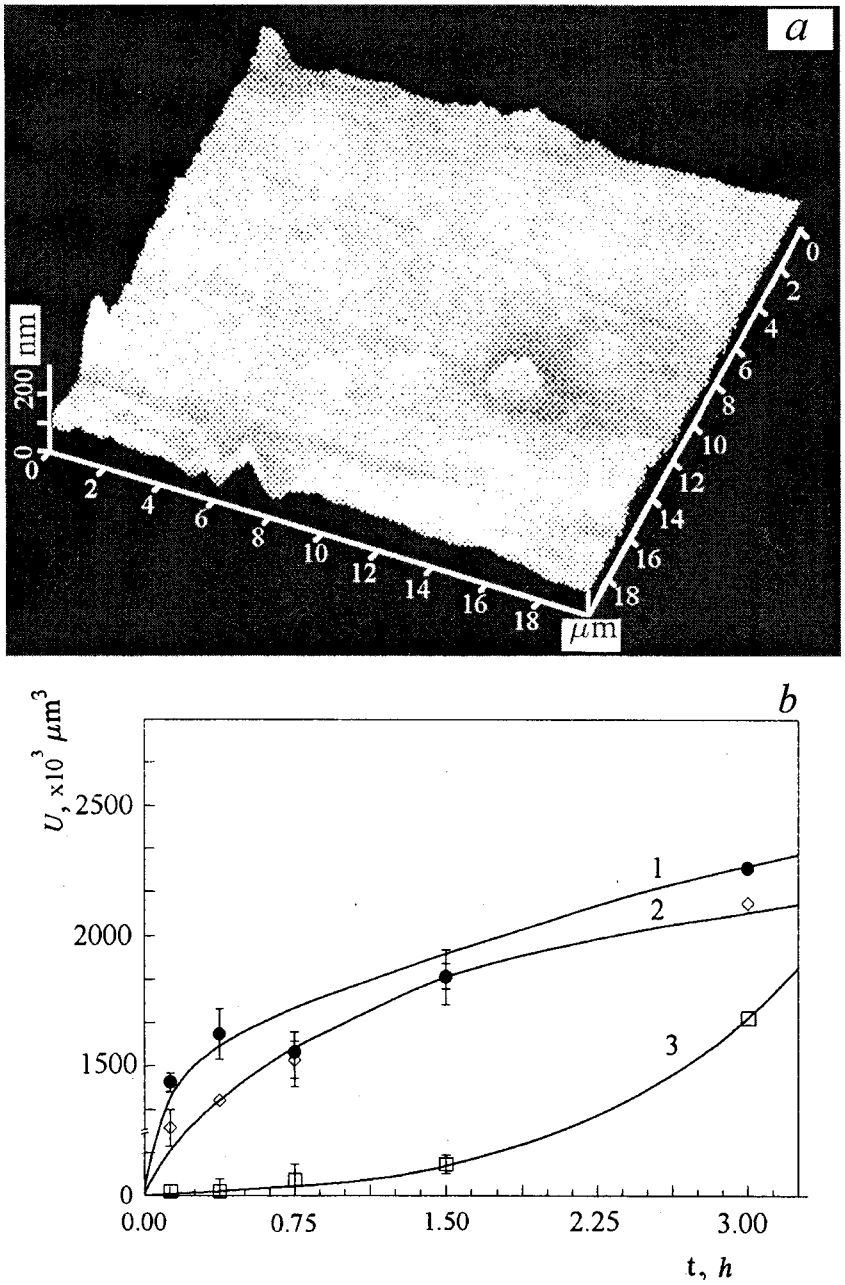

FIG. 2. a — Atomic force microscope images of the surface of a Ti_{41}–V_{41}–Al_{18} sample after implanting a $5\times10^{17}\,cm^{-2}$ dose of iron ions and a $5\times10^{16}\,cm^{-2}$ dose of zirconium ions followed by treatment with a low-energy, high-current electron beam with energy flux $5.5\,J/cm^2$, $\tau=2.5\,\mu s$, $E=10$–20 keV; b — time dependences of material wear as a result of friction of a 100 Cr6 steel ball on the surface of Ti_{41}–V_{41}–Al_{18} samples: *1* — initial state, *2* — after implanting a $1\times10^{17}\,cm^{-2}$ iron ion dose and a $5\times10^{16}\,cm^{-2}$ zirconium ion dose; *3* — after implanting a $5\times10^{17}\,cm^{-2}$ dose of iron ions and a $5\times10^{16}\,cm^{-2}$ dose of zirconium ions; *U* — material wear.

[6] A. N. Valyaev, A. D. Pogrebnyak, and S. V. Plotnikov, *Radiation Mechanical Effects in Solids Exposed to High-Intensity Pulsed Electron and Ion Beams* [in Russian], Gylym, Alma-Aty (1998), 266 pp.
[7] A. D. Pogrebnjak and D. I. Proskurovski, Phys. Status Solidi A **145**, 9 (1994).
[8] A. D. Pogrebnjak, A. D. Mikhaliov, N. A. Pogrebnjak Jr. *et al.*, Phys. Lett. A **241**, 357 (1998).
[9] A. Matthews and A. Leyland, Surf. Coat. Technol. **71**, 88 (1995).
[10] V. A. Shulov, G. E. Remnev, N. A. Nochevnaya *et al.*, Pis'ma Zh. Tekh. Fiz. **17**(9), 38 (1991) [Tech. Phys. Lett. **17**, 621 (1991)].
[11] D. I. Proskurovsky, V. P. Rotshtein, G. E. Ozur *et al.*, J. Vac. Sci. Technol. A **16**, 2480 (1998).
[12] V. A. Shulov, A. I. Ryabchikov, N. A. Nochevnaya *et al.*, Poverkhnost' No. 6, 132 (1993).
[13] D. M. Follstaedt, J. A. Knapp, and L. E. Pope, Appl. Phys. Lett. **45**, 529 (1984).
[14] I. L. Singer and T. M. Barlak, Appl. Phys. Lett. **43**, 457 (1983).
[15] J. -P. Hirvonen, M. Nastasi, and J. W. Mayer, Appl. Phys. **60**, 980 (1986).

Translated by R. M. Durham

Formation of gas folds during pressing of $Y_1Ba_2Cu_3O_{7-\delta}$ powder

S. A. Churin

Institute of Microstructure Physics, Russian Academy of Sciences, Nizhniĭ Novgorod
(Submitted July 16, 1998; resubmitted January 15, 1999)
Pis'ma Zh. Tekh. Fiz. **25**, 74–78 (August 12, 1999)

Conditions for the formation of density discontinuities during pressing of $Y_1Ba_2Cu_3O_{7-\delta}$ powder are described. The experimental results are explained using catastrophe theory. It is hypothesized that the density discontinuities are gas folds formed during pressing.
 [S1063-7850(99)01308-7]

One of the obstacles preventing the use of high-temperature superconductivity is the fabrication of products of specified dimensions and high density from high-temperature superconductor (HTSC) powder. These products fabricated by pressing are of independent scientific and technical interest and also form the initial materials for the charges used to obtain long HTSC crystals by the Bridgman–Stockbarger method[1,3] or zone refining.[2] The crystals thus obtained have a substantially higher critical current density than the initial charges. It was shown in Ref. 4 that the presence of pores in the charge leads to a loss of crystal stoichiometry during the crystallization process and a variation of the crystal parameters over length. The loss of stoichiometry increases as the concentration and sizes of the pores increases. The formation of long, high-density $Y_1Ba_2Cu_3O_{7-\delta}$ charges is thus quite a topical issue. However, the fabrication of charges by pressing is accompanied by the formation of various defects, including density discontinuities.

The phenomenon of powder stratification was described in Ref. 5 using a continuum model of the pseudoliquefaction of multicomponent media. This phenomenon was explained by the existence of friction between the powder and the tube walls, which leads to a multivalued distribution of the powder flux velocity over the tube length. We shall show that the density discontinuities formed during the static pressing process may also be a gas fold: some of the gas filling the pores in the charge collects in a single plane during pressing. In the present paper we report some results of experiments on the pressing of $Y_1Ba_2Cu_3O_{7-\delta}$ powder and calculations using catastrophe theory[6,7] which can be used to determine the coordinates of the fold formation.

The powder (typical grain size 10 μm) was poured into cylindrical molds 15 or 50 mm in diameter and compacted using a press. The density of the charge did not exceed 2.5 g/cm^3. After pressing at a pressure of 5×10^4 N/cm^2 the density of the charge increased to 3.5 g/cm^3. The piston velocity during the pressing process was $\sim$1 mm/s. After the $\sim$50 mm long finished article was removed from the 15 mm diameter mold, in some cases (at pressures higher than 1×10^4 N/cm^2) this disintegrated into two or three fragments 1.5–2 cm long. A density discontinuity ran over the cross-sectional surface. The surface of this discontinuity revealed no steps typical of breaking, and the convexity of the discontinuity surface was directed toward the piston. The normal to the discontinuity surface on the symmetry axis coincided with the axis of the mold. For the 50 mm diameter charge the length of the fragments was several millimeters out of a total charge thickness of 7–8 mm. In this case, the convexity of the discontinuity surface was directed away from the piston surface. On either side of the discontinuity, surface the density of the products varied continuously. In order to make numerical estimates to determine the coordinates of the folds using catastrophe theory,[6,7] we need to find the gas velocity distribution over the length of the charge during pressing. We shall consider the pressing process in greater detail. For simplicity we shall consider the one-dimensional motion of a powder in a semi-infinite medium. Under the action of the piston, the powder and the gas filling the pores begin to move, and the porosity of the charge and the gas pressure in it vary. Naturally, the volume of the charge is connected to atmosphere and some of the gas is expelled from the charge under pressure. However, the gas escape rate depends strongly on the porosity of the medium and the distance covered before the gas reaches the boundary of the charge,[8] and in our case was much lower than the velocity of the piston. Thus, a gas pressure gradient will always exist over the length of the charge during pressing. Under the action of this pressure gradient, the gas begins to move in the pores, and has an average velocity at the exit from a section of thickness $\Delta\xi$ determined by the Darcy law:[8]

$$\langle v\rangle=\eta^{-1}K(\Pi\nabla\langle p\rangle+\langle p\rangle\nabla\Pi), \tag{1}$$

where η is the viscosity of the gas, $K=\Pi^3\times d^2\times(1-\Pi)^{-2}$, d is the characteristic pore size, Π is the porosity of the medium, $\nabla\Pi$ is the porosity gradient of the medium, $\langle p\rangle$ is the average gas pressure in the medium,and $\nabla\langle p\rangle$ is the average gas pressure gradient in the medium for the section $\Delta\xi$. In expression (1) we neglected the gravitational force. In order to simplify the following estimates, we shall assume that the porosity of the charge is constant and the pressure is a function of the charge length and does not vary with time. In this case, the average gas velocity is:[8]

$$\langle v\rangle\approx-\eta^{-1}K\Pi\nabla\langle p\rangle. \tag{3}$$

In order to find the average gas pressure in the powder $\langle p\rangle$, we shall assume that the pressure distribution over the charge length is given by:[9]

$$p(\xi)=p_0\left(1-\exp\left(-\frac{R^2}{2\nu\xi^2}\right)\right), \tag{4}$$

where p_0 is the pressure at the surface of the piston, R is the radius of the cylindrical charge, and ν is a coefficient which determines the transfer of vertical load to the side wall of the mold. Expression (4) was derived and checked experimentally for soil. Its application in the present case can be justified by the fact that soil, like HTSC powder, is a low-plasticity oxide, and therefore it is predicted that they will exhibit the same behavior under pressing. The pressure in the gas filling the pores of the charge will obviously be lower than that in a powder, but we shall assume that its distribution over the length of the mold is also described by the law (4) to within the constant factor. We shall also assume that the average pressure in the section ξ_i, ξ_j will be equal to the pressure at the center of the selected section: $\langle p\rangle \approx p(\langle\xi\rangle)$. In this case, the average velocity at the point $\xi=0.5(\xi_i+\xi_j)$ will be given by:

$$v(\xi)\approx\langle v\rangle\approx \eta^{-1}K\Pi p_0\exp\left(-\frac{4a^2}{\xi^2}\right)\frac{8a^2}{\xi^3}, \tag{5}$$

where $a^2=R^2/2\nu$. Since the points ξ_i and, ξ_j were selected arbitrarily, we can assume that the expression for the gas velocity (5) holds for the total thickness of the charge. We shall then use a standard approach to determine the coordinates of fold formation.[6,7] We shall assume that in the section ξ_i, ξ_j the gas particles propagate at constant velocity (5). The coordinate for the beginning of formation of a gas fold may be determined from:[6,7]

$$x_s=\xi+v(\xi)(t-t_0), \tag{6}$$

where ξ is the Lagrange coordinate of the gas flux, t is the time of motion, and $v(\xi)$ is the gas velocity in the powder which is given by (5). Determining $d\langle v\rangle/d\xi$ and equating this to zero, we find that for $\xi>(8/3)^{0.5}a$ the derivative becomes negative and for $\xi<(8/3)^{0.5}a$ it is positive, i.e., in this case the gas can move toward the piston. Then, finding the second derivative (5) with respect to ξ and equating this to zero, we determine the two roots of the algebraic equation: $\xi_1=(3.5)^{0.5}a$ and $\xi_2=(1.5)^{0.5}a$. We recall that ξ_1 and ξ_2 are the Lagrange coordinates at which a fold begins to form. It is then easy to determine the coordinate of fold formation:

$$x_{\rm cr}=\xi_{\rm cr}-\frac{v(\xi_{\rm cr})}{v'(\xi_{\rm cr})}, \tag{7}$$

where $\xi_{\rm cr}$ is either ξ_1 or ξ_2. Performing the necessary calculations we find two values for the beginning of fold formation: $x_{\rm cr1}\approx 4.48a$ and $x_{\rm cr2}\approx 0.54a$. We postulate that $x_{\rm cr1}$ is responsible for fold formation for small mold diameters. A reverse fold does not have time to form for small mold diameters — a considerable fraction of the gas filling the pores escapes from the charge along the powder–mold interface. For the larger-diameter mold, a reverse fold does not have time to form and corresponds to the coordinate $x_{\rm cr2}$. The density discontinuity over the cross-sectional surface is also caused by the escape of gas from the charge. Taking into account the boundaries of the mold, the gas pressure distribution (4) is a function of the instantaneous radius of the mold. The expressions given above for ξ_1 and ξ_2 can be used to check the experimental results numerically. We shall take the mold radius to be 0.75 cm and ν to be 1. At this point, it should be noted that ν does not exceed 1. In this case, we obtain $a\approx 0.5$ cm and $x_{\rm cr1}\approx 2.2$ cm, which shows satisfactory agreement with the experimental results. Performing similar calculations for the larger, 50 mm-diameter mold, we find that the coordinate of reverse fold formation is $x_{\rm kp2}\approx 9$ mm. This value differs appreciably from that observed experimentally because of the approximate nature of the calculation model and because in our case, the pressure distribution function (4) near the surface of the piston differs appreciable from that proposed in Ref. 9. If the charge is sufficiently long, several successive folds may form, at approximately equal intervals. The formation of folds can be prevented by evacuating gas from the porous medium to a pressure less than 10 Pa before the beginning of pressing. The formation of folds is also observed during the pressing of other materials such as Y_2O_3.

This work was carried out under Project 95032 in the Superconductivity Section of the Program ''Topical Problems in Physics of Condensed Media.''

[1] S. Jin, T. H. Tiefel, R. S. Sherwood *et al.*, Appl. Phys. Lett. **52**, 2074 (1988).
[2] K. Salama and D. F. Lee, Supercond. Sci. Technol. **7**, 177 (1994).
[3] P. J. McGinn and M. A. Black, Physica C **156**(24), 57 (1988).
[4] S. A. Churin, Pis'ma Zh. Tekh. Fiz. **23**(8), 85 (1997) [Tech. Phys. Lett. **23**, 329 (1997)].
[5] L. A. Galin, Yu. P. Gupalo, and G. P. Cherepanov, *Mechanics of Multicomponent Media in Technological Processes* [in Russian], Nauka, Moscow (1978), 147 pp.
[6] V. I. Arnold, *Catastrophe Theory*, 2nd ed. (Springer-Verlag, Berlin, 1986) [Russ original, later ed., Nauka, Moscow, 1990, 128 pp.].
[7] Ya. B. Zel'dovich and A. D. Myshkis, *Elements of Mathematical Physics* [in Russian], Nauka, Moscow (1973), 352 pp.
[8] A. V. Lykov, *Heat and Mass Exchange* [in Russian], Énergiya, Moscow (1978), 477 pp.
[9] I. I. Kandaurov, *Mechanics of Granular Media and Its Application in Construction* [in Russian], Stroĭizdat, Leningrad (1988), 281 pp.

Translated by R. M. Durham

Dependence of the microwave surface resistance on the structure and thickness of superconducting cuprate films

S. F. Karmanenko, A. A. Svishchev, A. A. Semenov, I. T. Serenkov, V. I. Sakharov, and A. V. Nashchekin

St. Petersburg Electrotechnical University, St. Petersburg;
A. F. Ioffe Physicotechnical Institute, Russian Academy of Sciences, St. Petersburg
(Submitted March 29, 1999)
Pis'ma Zh. Tekh. Fiz. **25**, 79–88 (August 12, 1999)

An investigation is made of the microwave surface resistance R_s measured at 10 GHz and 77 K, as a function of the thickness of superconducting epitaxial films of yttrium barium cuprate grown on lanthanum aluminate substrates by magnetron sputtering. Films between 200 and 1800 nm thick have low values R_s (0.3–0.5) mΩ and do not show any deterioration. The level of R_s achieved in films of comparatively large thickness is mainly attributable to the low rate of film growth (0.8 nm/min). © *1999 American Institute of Physics.*
[S1063-7850(99)01408-1]

Studies of the microwave surface resistance R_s of yttrium barium cuprate $YBa_2Cu_3O_{7-\delta}$ (YBCO) superconducting films as a function of the thickness h were started more than ten years ago. Then, in the initial period of research on the behavior characteristics of YBCO films in the rf–microwave range, we observed[1] a nonmonotonic dependence $R_s(h)$ which was later studied in greater detail.[2,3] Since then, interest in this dependence has remained undiminished because this subject is not only of scientific value, but also has important practical applications. This is confirmed by a recent publication[4] in which Stork *et al.* reported some deterioration in the quality of YBCO films with increasing thickness. The depth of penetration of the magnetic field λ_L in a YBCO film at 77 K is at least 300 nm (Refs. 4 and 5) and superconducting lines of thickness several times λ_L are needed to transfer a high-power microwave signal without additional losses. Hence, YBCO films more than 1 μm thick[7] are required to develop microwave film devices.

Vendik *et al.*[2,3] observed that the critical thickness of YBCO films is 300–400 nm, and an increase in thickness causes R_s to increase to a high level, incompatible with the requirements of microwave cryoelectronics. The existence of a critical thickness was observed when YBCO films were grown on various types of (100)-oriented substrates having the mismatch parameter $\xi = 2(a_1 - a_2)/(a_1 + a_2)$, where a_1 and a_2 are the unit cell parameters for the substrate and film material.

Two types of substrate should be distinguished. Structurally matched substrates of perovskite compounds have a mismatch parameter ξ 1.0–2.0%; for instance, $SrTiO_3$, $LaAlO_3$, $NdGaO_3$, and a heteroepitaxial $Ba_xSr_{1-x}TiO_3$ layer grown on an MgO substrate.[3] The other type of substrates exhibit strong structural mismatch, such as MgO ($\xi \sim 9\%$), zirconium-stabilized yttrium oxide (YSZ, $\xi \sim 6\%$), and a heteroepitaxial CeO_2 layer on an α-$Al_2O_3[10\underline{1}2]$ substrate (cerium dioxide on *r*-cut sapphire).[6]

The deterioration of the film structure occurs because after the critical thickness has been reached, the film growth mechanism is impaired and a granular layer forms on the surface. The film becomes two-layered: the lower layer is highly oriented while the upper layer is either misoriented or granular. The growth mechanism is impaired by the buildup of stresses in the structure of the YBCO film and their ''sink'' effect in the network of interfaces formed when the growth mechanism breaks down. In this way, the defect structure of YBCO films of above-critical thickness becomes stabilized.

The $c_\perp$-oriented structure is most likely a metastable phase of YBCO.[7] The formation of a granular layer on the surface is similar to the mechanism for the formation of a ''columnar'' structure, observed on superconducting films of niobium compounds, such as NbN and Nb_3Ge (Ref. 8). If the width of the layer boundaries between the columns does not exceed the coherence length of the appropriate superconductor, conditions for a superconducting current are established in the granular structure. A similar structure is responsible for the exaggerated values of R_s and the additional microwave losses, which may be identified in experiments where a static magnetic field is applied to the microwave cavity.[9]

The mechanism for the formation of three-dimensional defects in the form of a regular network of pores (pinholes)[10] is more favorable for reducing the microwave residual losses in superconducting films. The almost straight-through pores or ''wells,'' where impurity phases can be identified at the bottom, play the same role in the stress and impurity sink as the network of intergranular layers. In this case, however, there are no barriers for the superconducting current and the microwave losses are reduced. A porous defect structure can overcome the micron barrier for the formation of highly oriented YBCO films, and the presence of a network of three-dimensional defects has little influence on the characteristics of planar topologies used in microwave cryoelectronics. However, the presence of pores in the films plays a negative role for other applications. In a porous structure, the noise level increases, such as the low-frequency flicker noise char-

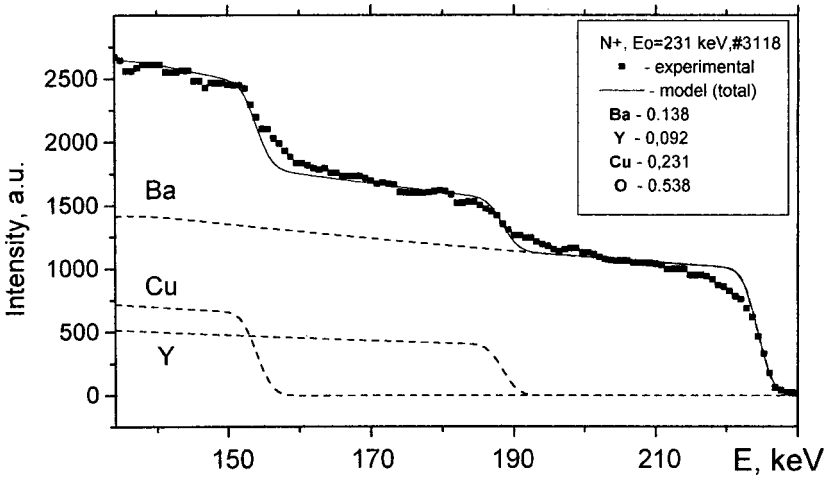

FIG. 1. Determination of the component composition of a 1.8 μm thick YBCO film (No. 3118) from the scattering spectrum of 231 keV nitrogen ions; the ratio of the cationic components Y:Ba:Cu is 0.92 : 0.138 : 0.231 or 2 : 3 : 5.

acterized by the Hooge parameter α since a pore is an independent fluctuator.[11] The parameter α determines the operating characteristics of antenna microbolometers, i.e., the detection sensitivity and the equivalent noise power in the submillimeter range.[12] Porous films cannot be used in layered structures because of possible ''punctures'' and shorting of the layers. Thick porous films have many advantages, but smooth YBCO films more than 1 μm thick are required to fabricate cryoelectronics devices. Thus, we need to search for mechanisms of formation in which the epitaxial structure in YBCO films is stabilized by low-dimensional defects.

In the present study we investigate the growth of epitaxial films more than 1 μm thick on $LaAlO_3(001)$ (LAO) substrates. The films were deposited by dc magnetron sputtering of a stoichiometric target. Details of the growth process of the YBCO films were presented in Refs. 3 and 7. The microwave surface resistance was measured using a plane–plane resonator method (Taber method[13]) at 10 GHz and 77 K. Medium-energy ion scattering was used to investigate the structure and composition of the films.[3,14] The energy distribution of the scattered ions was analyzed after a 100–230 keV primary H^+, He^+, or N^+ beam had interacted with the sample. For the analysis we used an electrostatic analyzer or semiconductor detector operated in the randomly oriented beam regime, or with channeling along the [001] axis of the substrate, and we measured the dependences of the reflected ion yield on their energy, $Y_r(E)$ and $Y_c(E)$, respectively. The ratio $\chi(E)=Y_c(E)/Y_r(E)$, described as the relative yield, characterized the perfection of the crystal lattice of the samples.

In order to achieve a two-dimensional mechanism of film growth at the very early stages, as far as 3 ML, the conditions of formation must be close to equilibrium. A low atomic-component flux density and elevated temperature help to establish more equilibrium conditions of deposition, intensify surface diffusion, and prevent the formation of competing $c_{\|}$-phase nuclei. The formation of blocks of alternative orientation leads to the formation of interblock boundaries which tend to disrupt the oriented growth mechanism.

In the growth regime used, the specific power of the magnetron discharge was initially set at 30% lower than the rated value, which was $\sim$5–6 W/cm^2. The discharge power was increased and the substrate temperature was gradually reduced by 20–30 K over 20–25 min. The substrate temperature in the steady-state film growth process was $\sim$1000 K. The results of investigations of ultrathin films showed that approximately three monolayers formed over this time in the layer-by-layer growth regime (Frank–van der Merwe mechanism).[14,15] Channeling was observed on the Ba–Y

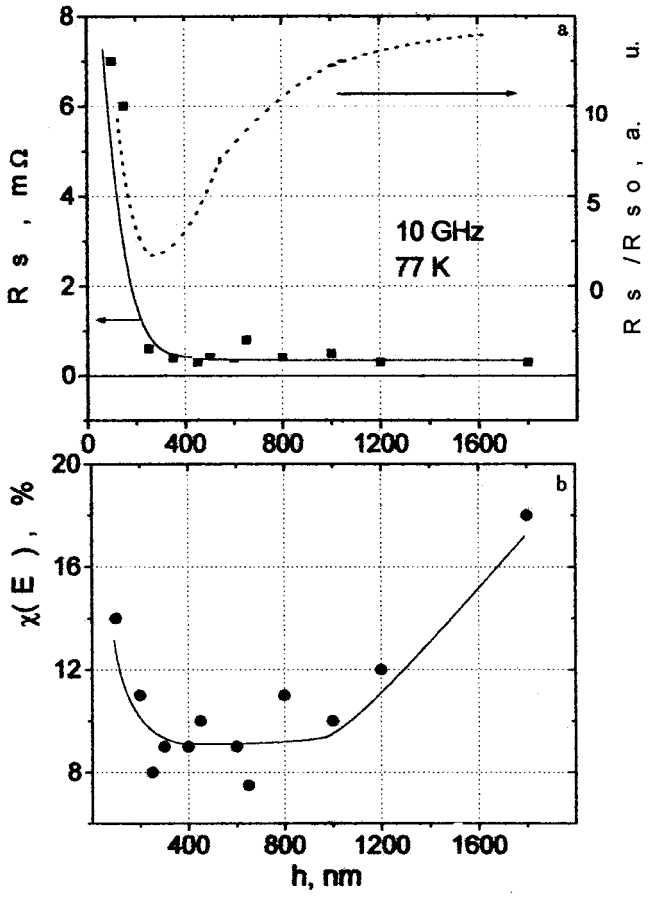

FIG. 2. Physical characteristics of YBCO films as a function of thickness *h*: a — microwave surface resistance measured at 10 GHz and 77 K; b — relative yield χ of He^+ ions of initial energy $\sim$200 keV determined from the intensity ratio of the scattered ion flux in the channeling regime $Y_c(E)$ to the flux in the random orientation regime $Y_r(E)$.

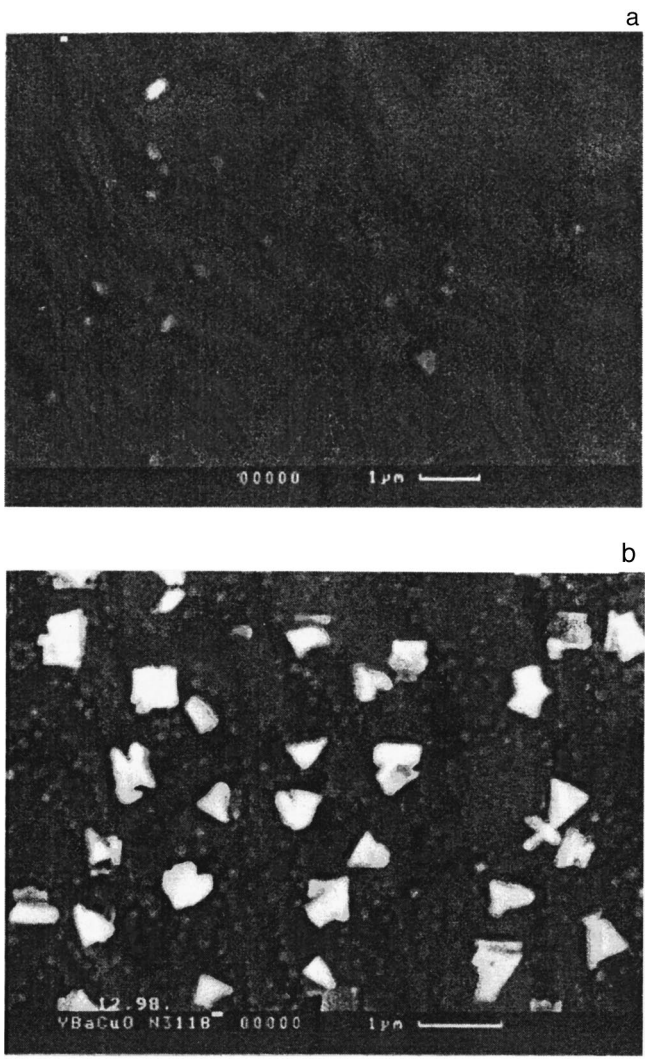

FIG. 3. Surface morphology of YBCO films of different thickness: a — epitaxial film ~500 nm thick, b — highly oriented surface layer of 1.8 μm thick film (No. 3118, see Fig. 1).

sublattice and the composition of the films was close to stoichiometric or had a small copper and barium deficit. Photomicrographs of the surface revealed homogeneous morphology with no islands, pores, or outgrowths.

Cationic and planar defects, i.e., corner and twinning boundaries, and edge dislocations, can be used to stabilize the superconducting phase on substrates with low ξ. At certain stages in the growth, screw dislocations develop, promoting the evolution of a surface relief. Thermodynamic estimates[15] showed that for the growth regimes used, conditions for the formation of the equilibrium (123) phase do not exist but various mechanisms of defect formation and stabilization of the perovskite compound are probable. An analysis of equilibrium in a $YO_{1.5}$–CuO–BaO system using methods of geometric thermodynamics showed that the Gibbs potential ΔG of the (123) phase should be reduced to a minimum of 50 kJ/g-atom by means of nonequilibrium defects, i.e., by 20–25%. One of the probable mechanisms for cationic defect formation is the formation of an orthorhombic phase, assumed to have the composition $\langle 235 \rangle$ (Ref. 15). This assumption is based on studies of the cationic composition of YBCO films grown on LAO substrates. Films having the highest critical parameters have a low barium and copper deficit. This conclusion agrees with the experimental results obtained in Ref. 16. Figure 1 shows the medium-energy ion backscattering spectrum obtained when YBCO/LAO sample No. 3118, having a film thickness of ~1.8 μm and $R_s \approx 0.3\,\mathrm{m\Omega}$, was bombarded with nitrogen ions. The spectrum showed that the film has the composition $Y_{1.2}Ba_{1.8}Cu_3O_{7-x}$, which corresponds to the ratio $\langle 235 \rangle$.

Figure 2a gives the dependence $R_s(h)$ for YBCO/LAO films grown under steady-state conditions at a rate of ~0.8 nm/min. This curve is hyperbolic and does not exhibit extrema similar to those observed for YBCO/BSTO/MgO films.[1–3] For comparison, the dashed curve in Fig. 2a gives the dependences of the surface resistance R_s/R_{s0} measured earlier, in arbitrary units for which R_{s0} is ~5 mΩ at 60 GHz and 4.2 K (Ref. 3).

The monotonic behavior of $R_s(h)$ for film thicknesses less that 1 μm agrees with the dependence $\chi_S(h)$ of the relative yield measured from the extremum of $\chi(E)$ at the surface of the film (near the maximum energy of the scattered ions). The graph of $\chi(E)_S$ plotted in Fig. 2b differs from the dependence of the surface resistance plotted in Fig. 2a. The layer-by-layer mechanism of YBCO film growth on LAO substrates is probably achieved up to a thickness of around 1 μm in the growth regime described above. At ~500 nm thickness, various light formations appear on the surface, which could decorate interblock and corner boundaries. Figure 3a shows a photomicrograph of the surface of a ~500 nm thick film. This occurs because the free surface energy is substantially reduced along lines of planar defects, which promotes the attachment of competing-phase nuclei at these defects. When the thickness increases to ~1 μm, screw dislocations begin to reach the surface of the film, three-dimensional dominant-phase nuclei begin to form, and the layer-by-layer growth is replaced by the growth of isolated pyramids and columns along the dislocation axis. Figure 3b shows the surface morphology of sample No. 3118, ~1.8 μm thick, which reveals a cellular morphology with isolated microblocks of 250–300 nm. Isolated crystallites of a competing phase measuring around 0.5 μm are observed on the surface. The microblock size of the structurally perfect phase can be used to estimate their density as ~(1–2) $\times 10^9\,\mathrm{cm}^2$. This estimate agrees with the density of nucleation centers of the $c_\perp$-oriented phase determined in Ref. 18. The formation of microblocks of the dominant phase and isolated crystallites of the competing phase leads to an increased yield of scattered ions in the channeled regime, $Y_c(E)$. However, this feature of the growth mechanism does not appear on the curve $R_s(h)$. Thicker (greater than 1.2 μm) YBCO/LAO films are most likely ''two-layer.'' The epitaxial layer is transformed into a $c_\perp$-highly oriented upper layer having a pyramidal columnar structure in which the microblock boundaries contain no competing phases and do not introduce additional microwave losses.

A barium and copper deficit in the YBCO films may be provided by an ''on-axis'' film deposition regime at a low working gas (argon–oxygen mixture) pressure, 30–40 Pa. When the substrates are positioned in the forward projection

of the erosion zone, the growing films are exposed to the action of the glow discharge plasma, which results in a slight deficit of the component most liable to resputtering, i.e., barium. The excess yttrium atoms in the crystal lattice occupy barium positions, which leads to the formation of substitutional Y_{Ba} defects which help to stabilize the $c_{\perp}$-oriented phase. Another mechanism for self-regulation of the film composition also appears, in which crystallites of a competing phase (presumably $BaCuO_2$), containing no yttrium atoms and possessing dielectric properties, reach the surface of the film. The structurally perfect orthorhombic phase expels nuclei of the competing phase to the surface, their size increasing as the film grows. It should be noted that the competing-phase crystallites can be almost completely removed from the surface as a result of treatment in organic liquids or ionic purification (which should be followed by heat treatment of the films in oxygen). Measurements of the electrical parameters of the YBCO films, which are indicators of the $\langle 235 \rangle$ phase, revealed that T_c reaches 93.5 K, the Hooge constant has the lowest values yet recorded, $\sim 2 \times 10^{-4}$ at 93 K (Ref. 12 and 17), and the microwave surface resistance measured at 77 K and 10 GHz is $\sim 3 \times 10^{-4}$ mΩ.

To sum up, we have shown that YBCO films up to 2 μm thick can be formed without any increase in the microwave surface resistance. For epitaxial smooth YBCO/LAO structures we observed a change in the growth mechanism at a thickness of $\sim (1.0–1.2)\,\mu$m.

This work was carried out under Projects Nos. 98055 and 98031 under the ''Superconductivity'' Program.

The authors are grateful to I. B. Vendik and O. G. Vendik for their interest in this work, support, and discussion, and also to R. N. Il'in and M. E. Gaevskiĭ for participating in the analysis of the results and useful discussions.

[1] O. G. Vendik, M. M. Gaĭdukov, S. F. Karmanenko *et al.*, Pis'ma Zh. Tekh. Fiz. **15**(7), 69 (1989) [Sov. Tech. Phys. Lett. **15**, 277 (1989)]; O. G. Vendik, M. M. Gaĭdukov, S. F. Karmanenko *et al.*, in *Proceedings of the European Conference on High Temperature Superconductors*, Ustron, Poland, 1989 (World Scientific, Singapore, 1990) pp. 521–525.
[2] O. G. Vendik, Yu. V. Likholetov, S. F. Karmanenko *et al.*, Physica C **179**, 91 (1991).
[3] S. F. Karmanenko, M. V. Belousov, V. Ju. Davydov *et al.*, Supercond. Sci. Technol. **6**, 23 (1993).
[4] F. J. B. Stork, J. A. Beal, A. Roshko, D. C. DeGroot *et al.*, IEEE Trans. Appl. Supercond. **7**, 1921 (1997).
[5] S. A. Wolf and V. Z. Krestin, IEEE Trans. Magn. **27**, 621 (1991).
[6] R. Schulz, M. Simoneau, and J. Lanteigne, Physica C **233**, 113 (1994).
[7] S. F. Karmanenko, V. Yu. Davydov, A. P. Mitrofanov, and A. A. Semenov, Pis'ma Zh. Tekh. Fiz. **22**(23), 69 (1996) [Tech. Phys. Lett. **22**, 982 (1996)].
[8] M. Bel'ski, M. M. Gaĭdukov, S. F. Karmanenko *et al.*, Fiz. Tverd. Tela (Leningrad) **29**, 2953 (1987) [Sov. Phys. Solid State **29**, 1697 (1987)].
[9] M. M. Gaidukov, S. F. Karmanenko, A. B. Kozyrev *et al.*, Supercond. Sci. Technol. **7**, 721 (1994).
[10] E. K. Hollman, V. I. Gol'drin, V. E. Loginov, D. A. Plotkin, S. V. Razumov, and A. V. Tumarkin, Pis'ma Zh. Tekh. Fiz. **23**(5), 39 (1997) [Tech. Phys. Lett. **23**, 186 (1997)].
[11] Sh. Kogan, *Electronic Noise and Fluctuations in Solids* (Cambridge University Press, Cambridge, 1996), 354 pp.
[12] A. V. Bobyl, M. E. Gaevski, S. F. Karmanenko *et al.*, J. Appl. Phys. **82**, 1274 (1997).
[13] R. C. Taber, P. Merchant, R. Hiskes *et al.*, J. Supercond. **5**, 371 (1992).
[14] V. V. Afrosimov, R. N. Il'in, S. F. Karmanenko *et al.*, Fiz. Tverd. Tela (St. Petersburg) **41**, 588 (1999) [Phys. Solid State **41**, 601 (1999)].
[15] S. F. Karmanenko, Izv. Vyssh. Uchebn. Zaved. Rossii Radioélektron. No. 1, 1 (1999).
[16] P. Schneider, G. Linker, and R. Schneider, Physica C **266**, 271 (1996).
[17] A. V. Bobyl, S. F. Karmanenko, V. N. Leonov, and R. A. Suris, in *Proceedings of the Conference ''Physics at the Threshold of the 21st Century''*, Ioffe Institute, St. Petersburg, 1998, p. 47.
[18] C. W. Nieh, L. Anthony, J. Y. Josefowicz, and F. G. Krajenbrink, Appl. Phys. Lett. **56**, 2138 (1990).

Translated by R. M. Durham

Particle size distribution in a coagulating dusty plasma

I. A. Belov, A. S. Ivanov, D. A. Ivanov, A. F. Pal', A. N. Starostin, and A. V. Fillipov

''Kurchatov Institute'' Russian Science Center, Moscow, Russia
(Submitted March 18, 1999)
Pis'ma Zh. Tekh. Fiz. **25**, 89–95 (August 12, 1999)

A modified version of the classical coagulation theory in the diffusion approximation is used to study some anomalies in the behavior of the particle size distribution function. It is established that unlike a normal aerosol, in a dusty plasma the dispersion of the distribution and the average particle size may decrease with time. © *1999 American Institute of Physics.* [S1063-7850(99)01508-6]

Studies of the particle coagulation process in a dusty plasma and in particular, the behavior of the particle size distribution function are relevant to the problem of material transport and surface contamination in the fabrication of semiconductor devices in microtechnology.[1–3] Similar problems arise in areas associated with plasma-chemical technologies for the fabrication of powders.[4] In this last case, coagulation is one of the main mechanisms responsible for dust particle growth. The microparticle size distribution is also important for investigations of a nuclear battery using a dusty plasma formed by micron-size radioactive particles in an excimer gas such as xenon,[5] and for developing new technologies for depositing coatings.[6] An important difference between this situation and the usual aerosol is that the particles may undergo monopolar charging with comparatively large charges while conserving the overall electrical neutrality of the medium.

We know[7] that for a monopolar-charged aerosol, electrostatic repulsion leads to the separation of like-charged particles, reduces the coagulation rate, and causes a drop in the aerosol concentration. The behavior characteristics of particles in a dusty plasma are first, associated with the suppression of coagulation as a result of monopolar charging for particle sizes smaller than the Debye shielding length R_d and second, equalizing this charge for sizes larger than R_d.

On entering a plasma, dispersed particles become negatively charged because the electron mobility is substantially higher than the ion mobility. The characteristic particle charging time is 10^{-5}–10^{6} s (Ref. 8). It should be noted that the characteristic discharge time, which is determined by ion diffusion and drift, is appreciably longer than the times given, but is substantially shorter than the characteristic times for variation of the particle size distribution as a result of coagulation over a wide range of dust particle sizes and concentration n_d. In view of this, the problems of particle charging and formation of the distribution function can be separated and solved consecutively.

To be specific, we shall consider the case when the ionization in a plasma is created by fast particles. This example is typical of the dusty plasma of a nuclear battery[5] where these particles may be electrons or α-particles depending on the type of radioactivity. The plasma composition is determined by the charge conservation equations (the plasma quasineutrality condition) and the continuity equations for the electrons and ions.[5,9] An analysis of these equations shows that the ratio of the dusty-particle charges q to their radius r_d and the volume-averaged concentrations of ions $\overline{N}_+$ and electrons $\overline{N}_-$ for a given ionization source power Q are functions of the product $\xi = n_d r_d$ and are given by the similarity relations:

$$\overline{N}_- = f_1(\xi, Q); \quad \overline{N}_+ = f_2(\xi, Q); \quad \frac{q}{r_d} = f_3(\xi, Q). \qquad (1)$$

Assuming that $q \sim r_d$, i.e., $f_3(\xi, Q) = \text{const}$, then ξ is proportional to the sum charge collected at the aerosol particles. In this case, the relations (1) have a fairly simple meaning, i.e., that the plasma composition is determined only by the source power and the total charge collected by the aerosol dispersed in it.

Calculations made using formulas from Ref. 5, taking into account Eqs. (1), show that the curve of q/r_d (Fig. 1) resembles a slightly broadened Fermi step. It can be seen from Fig. 1 that the ratio q/r_d and therefore the particle floating potential $U = eq/r_d$ are constant over a wide range of parameters of the plasma dust component as far as a certain value $\xi = \xi_0$, which is determined by the power of the ionization source. If the initial concentrations and particle sizes of the aerosol satisfy the condition $\xi \leqslant \xi_0$, then the inequality $\xi \leqslant \xi_0$ holds during the coagulation process, which is accompanied by a fall in the particle concentration and an increase in the particle size. This means that the dusty particle coagulation process can be studied under the condition $U = \text{const}$.

The coagulation of a polydisperse system with an arbitrary initial particle size distribution is described using a solution of the Smolukhovskiĭ system of equations

$$\frac{\partial n_d(r_k,t)}{\partial t} = -\sum_i \left(1 - \frac{1}{2}\delta_{ik}\right) G(r_i, r_k) n_d(r_i,t) n_d(r_k,t) + \frac{1}{2}\sum_i \sum_j G(r_i, r_k)\theta_{ij}^k n_d(r_i,t) n_d(r_j,t), \qquad (2)$$

where $n_d(r_k,t)$ is the concentration of particles having radii between r_k and r_{k+1} at time t, $G(r_i, r_j)$ are the coagulation

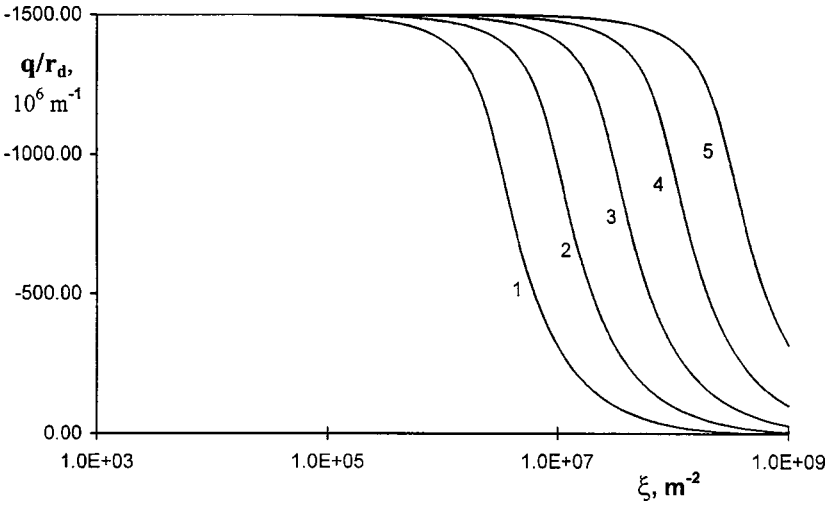

FIG. 1. Ratio of charge to radius of dust particles in a xenon plasma as a function of the parameter ξ. The numbering of the curves corresponds to different rates of ionization: $(1,2,\ldots,5)\rightarrow Q=10^{19}$, 10^{20}, ..., $10^{23}\,\mathrm{m}^{-3}\cdot\mathrm{s}^{-1}$.

constants of particles having radii r_i and r_j, respectively, δ_{ik} is the Kronecker delta, θ_{ij}^k are the interpolation coefficients, and $i,j=1,2,3,\ldots,N$ (Ref. 10).

The influence of the particle charging on the profile of the distribution function was taken into account by renormalizing the coagulation constants in the formulas (2). This procedure was carried out using an approached developed by Fuks,[7] although the shielded Coulomb potential $\varphi_i(r)$ was used as the electrostatic interaction potential of the particles. The ratio of the coagulation constants of the charged and

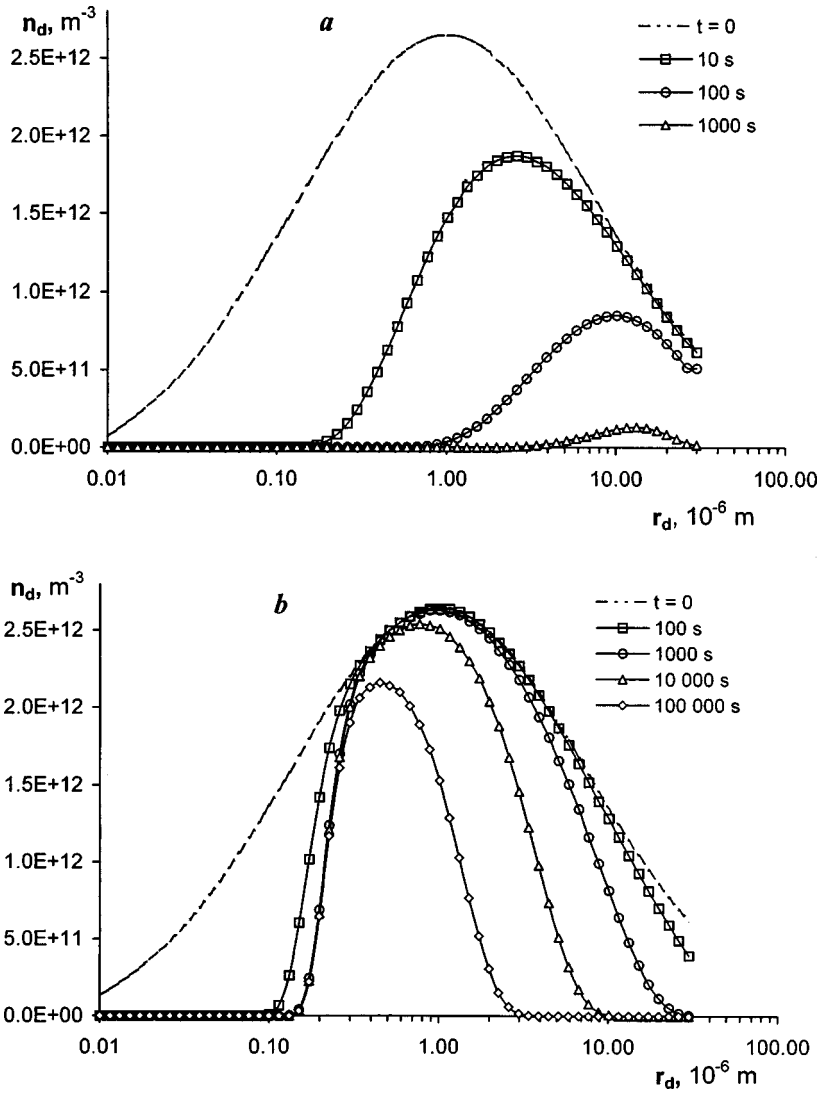

FIG. 2. Dynamics of variation in particle size distribution per unit volume: a — uncharged polydisperse aerosol, b — dusty plasma.

uncharged dust particles γ_{ik} is then given by:

$$\gamma_{ik}=\left(\int_0^1 \exp\left\{\frac{1}{kT}\Psi_{ik}\left(\frac{r_i+r_k}{x}\right)\right\}dx\right)^{-1},$$

$$\Psi_{ik}(r)=eq_k\varphi_i(r), \tag{3}$$

where $eq_k=r_kU$ is the charge of a particle of radius r_k.

The behavior of the coagulation constants of the charged particles in the plasma changes drastically. As the particle size increases, a decrease in the coagulation constants caused by electrostatic repulsion is replaced by an increase caused by the Debye shielding of the charges. The nonmonotonic dependence of the coagulation constants on the particle size significantly changes the behavior of the particle size distribution function with time. Dependences of the concentrations on the particle sizes, calculated by us taking these factors into account are plotted in Figs. 2a and 2b. Graphs of $n_d(r_k,t)$ for an uncharged aerosol at various times are also plotted for comparison (Fig. 2a). The initial distribution was taken to be a lognormal particle size distribution with a geometric standard deviation of two and an average radius $\overline{r_i}=10^{-6}$ m (the initial total concentration of dust particles is $10^{14}\,\mathrm{cm}^{-3}$). The calculations were made for a plasma having the Debye radius $R_d=8.4\times10^{-6}$ m and the floating potential $U=0.15$ V. The range of variation of the particle sizes ($r_{\min}=10^{-8}$ m, $r_{\max}=3\times10^{-5}$ m) was split into $m=60$ divisions having the relations $(m-1)\ln(r_k/r_{k-1})=\ln(r_{\max}/r_{\min})$. In order to ensure that the largest particles did not accumulate in the system and distort the distribution function, effective deposition was introduced.

The results indicate that charging of the particles generally slows the coagulation process. At the same time, the behavior of the distribution function changes qualitatively. Initially a small fraction whose coagulation is slowed considerably less than the larger particles is rapidly removed. This leads to the appearance of clusters having a ''cauliflower'' structure, consisting of numerous small particles. Collisions between larger particles are impeded by the resulting Coulomb barrier. As it moves in the direction of increasing particle size, the distribution function appears to ''encounter'' the Coulomb barrier. However, for particles whose sizes are comparable to or greater than the Debye length, the electrostatic repulsion effect decreases and their coagulation becomes more probable. This leads to the ''removal'' of larger fractions in the particle size distribution. The distribution becomes narrower and the dispersion decreases. Another interesting feature in the behavior of the distribution function under these conditions is that the average particle size may decrease with time.

To sum up, the behavior of the particle size distribution in a dusty plasma is anomalous and has many interesting features which may lead to some unusual physical phenomena important for the production of a nuclear battery,[5] such as the levitation of a long-lived ''quasiliquid'' dusty structure in an electrostatic trap. At the same time, the possible technological applications of these effects are quite clear, especially the possibility of developing control measures to prevent the contamination of surfaces during ion etching processes.

To conclude the author would like to thank V. Yu. Baranov, V. E. Fortov, A. V. Dem'yanov, and Yu. V. Petrushevich for useful discussions of this work.

[1] V. N. Tsytovich, Usp. Fiz. Nauk **167**(1), 57 (1997).
[2] S. J. Choi and M. J. Kushner, J. Appl. Phys. **74**, 853 (1993).
[3] F. J. Huang and M. J. Kushner, J. Appl. Phys. **81**, 5960 (1997).
[4] S. A. Krapivina, *Plasma-Chemical Technological Processes* [in Russian], Khimiya, Leningrad (1981), 248 pp.
[5] V. Yu. Baranov, I. A. Belov, A. V. Dem'yanov, A. S. Ivanov *et al.*, Preprint No. IAE-6105/6 [in Russian], Russian Scientific Center, ''Kurchatov Institute,'' Moscow (1998), 39 pp.
[6] H. S. Shin and D. G. Goodwin, Mater. Lett. **19**, 119 (1994).
[7] N. A. Fuks, *Mechanics of Aerosols* [in Russian], Academy of Sciences of the USSR Press, Moscow (1955), 252 pp.
[8] P. Raĭst, *Aerosols: Introduction to the Theory* [Russ. transl.], Mir, Moscow (1987), 278 pp.
[9] B. M. Smirnov, *Aerosols in Gases and Plasmas* [in Russian], IVTAN, Moscow (1990), 102 pp.
[10] H. Bunz, M. Kouro, and W. Schock, *NAUA-MOD4 - A Code for Calculating Aerosol Behaviour in LWR Core Melt Accidents, Code Description and Users Manual KfK-3554* (KfK, Karlsruhe, 1983), 66 pp.

Translated by R. M. Durham

Transition to classical behavior in mesoscopic magnetic systems and quantum decoherence

V. V. Makhro and Ya. A. Padamanov

Moscow Pedagogical State University, Bratsk Industrial Institute
(Submitted April 1, 1999)
Pis'ma Zh. Tekh. Fiz. **25**, 1–5 (August 26, 1999)

A mesoscopic $CrNi_6$ system is used to demonstrate the possibility of transitions from quantum to classical behavior in thermally stimulated tunneling processes. The main mechanism responsible for these transitions is assumed to be quantum decoherence produced as a result of thermal interaction between the spin system and its neighborhood. Results are presented of calculations of the disruption probability for a mesoscopic system as a function of temperature. It is shown that the main characteristic which can reveal the decoherence effect is the nonmonotonic behavior of the disruption probability at low temperatures. © *1999 American Institute of Physics.* [S1063-7850(99)01608-0]

Interest in transitions of mesoscopic systems from quantum to classical behavior (and the reverse) is fully justified from the applied and general physical point of view. Of late this interest has been predominantly directed toward the recently discovered high-spin magnetic clusters such as $Mn_{12}Ac$, $CrNi_6$, and similar. These systems may be observed in various quasisteady states, usually separated by a potential barrier of a few tens of kelvin. Some time ago it was assumed that the transition between these takes place either by tunneling or by thermal activation. It was also assumed that the regions where disruption takes place by either of these mechanisms can be clearly delimited by temperature. However, it then became clear that the potential barrier is always overcome (even at temperatures very close to zero) by the combined action of both mechanisms, i.e., thermally stimulated tunneling.

The process of overcoming the potential barrier can then be represented schematically as follows. A system being in thermal equilibrium with its environment can, at a given temperature T, acquire the energy E with a specific probability $P(E,T)$. This system can then overcome the barrier with a probability, say $G(E)$. It is important to stress that pure thermal activation as understood classically will not exist for any E, if only because of the need to allow for above-barrier reflection. Naturally, in this sense so-called first-order transitions from quantum to classical disruption, as discussed in Refs. 1–3, are completely excluded. The total probability for the disruption of a mesoscopic system as a function of T is given by

$$P_{\text{tot}}(T) - \int_0^\infty P(E,T)G(E)dE.$$

In most cases, a mesoscopic spin system is sufficiently well described using the model of a particle in a two-well potential. Even in the semiclassical case, assuming a quasicontinuous spectrum, $G(E)$ can only be calculated explicitly at the bottom of the well. For an arbitrary semiclassical potential $U(x)$ the corresponding value of $G(E)$ will be

$$G(E) = \frac{\overline{\omega}}{\pi}\exp\left(-\frac{\pi E}{\hbar\overline{\omega}}\right), \tag{1}$$

where $\overline{\omega} = \sqrt{m/|U'(x=x_{\min})|}$ is the frequency of the classical oscillations at the bottom of one of the potential wells and its condition of validity will be: $kT \ll \hbar\overline{\omega}$. Assuming a Maxwellian energy distribution, for the asymptotic behavior of P_{tot} in the limit $T \to 0$ we have

$$P_{\text{tot}}(T) \propto \exp\left(\frac{2\pi U_0}{\hbar\overline{\omega}}\right)\frac{G\overline{\omega}^{3/2}\hbar^{3/2}}{(\hbar\overline{\omega}+2\pi k' l')^{3/2}}, \tag{2}$$

where U_0 is the barrier height. Expression (2) can only be used to determine the behavior tendency of the total disruption probability at low temperatures. With increasing temperature, the probability of a particle acquiring higher energy as a result of interaction with the thermal system of the crystal increases exponentially, and the semiclassical expression (1) becomes unacceptable. For arbitrary T, a numerical analysis of the system becomes preferable (see, for example, Refs. 4 and 5). The numerical schemes used in these studies involve analyzing an ensemble of identical particles localized in a two-well potential, calculating the energy distribution of these particles (the quasicontinuous spectrum in the semiclassical approximation or the discrete spectrum in the quantum case), calculating the probability of crossing the barrier, and finally determining the fraction of particles that have crossed the barrier as a result of tunneling or an above-barrier transition. The latter gives the total probability of disruption of the system.

These schemes give results which show fairly satisfactory agreement with the experimental data. However, at low temperatures they predict a monotonic decrease in the disruption probability with decreasing temperature, whereas deviations of the dependence of the disruption probability from monotonic are recorded experimentally at temperatures below 10 K (see, for instance, Ref. 6). We postulate that quantum decoherence effects accompanying tunneling are responsible for this behavior.

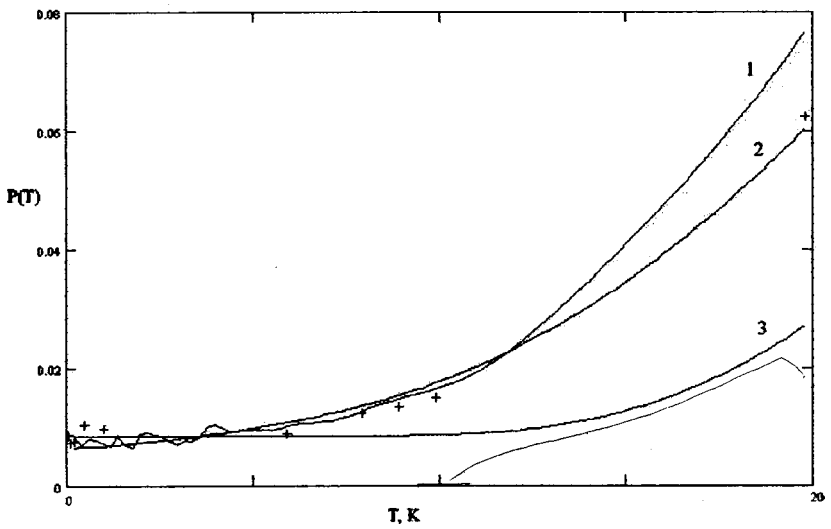

FIG. 1. Disruption probability as a function of temperature: *1* — probability of thermally stimulated tunneling allowing for decoherence, *2* — probability of thermally stimulated tunneling in the absence of decoherence, *3* — probability of thermally stimulated disruption calculated in accordance with Ref. 6, + — experimental data from Ref. 6.

The influence of decoherence on particle tunneling in a symmetric two-well potential was first described by Grossmann *et al.*[7] The decoherence effect occurred as a result of an external periodic force $S \sin \overline{\omega} t$ acting on the system and was manifest as the ''freezing'' of tunneling at certain values of S and $\overline{\omega}$. The authors of Refs. 8–10 then derived explicit expressions for the tunneling probability in the presence of an external periodic perturbation:

$$P_{\mathrm{dec}} = P J_0\left(\frac{2V}{\hbar \overline{\omega}}\right), \tag{3}$$

where P is the tunneling probability in the absence of a perturbation and $J_0(x)$ is a Bessel function. In particular, the zeros of $J_0(x)$ determine the parameters V and $\overline{\omega}$ at which tunneling is completely frozen and the particle remains for an arbitrarily long time in one of the wells.

We shall model the interaction between a particle and the thermal system of a crystal by the interaction with a finite set of classical harmonic oscillations at frequencies $\overline{\omega_i}$, and we shall assume that the corresponding oscillation amplitudes A_i are proportional to the probability of realizing a particular frequency at a particular temperature. For V_i we then have $V_i = Cn(\overline{\omega_i}, T)\hbar \overline{\omega_i}$, where C is the coupling constant. We shall take the distribution function $n(\overline{\omega_i}, T)$ in the form $(\exp(\hbar \overline{\omega_i})/kT) - 1)^{-1}$, which gives for the argument of the Bessel function: $C(\exp(\hbar \overline{\omega_i}/kT) - 1)^{-1}$. At a given temperature T interaction with ''high-frequency'' oscillators ($\overline{\omega_i} \gtrsim kT/\hbar$) has little influence on the modulated tunneling probability (3) because, as the ratio $\hbar \overline{\omega_i}/kT$ increases, the Bessel function rapidly tends to unity. Conversely, interaction with ''low-frequency'' oscillators whose fraction increases with decreasing temperature, leads to the appearance of fast oscillations in Eq. (3) and consequently causes an abrupt change in the behavior of $P_{\mathrm{tot}}(T)$ at low temperatures.

Detailed calculations confirm this qualitative conclusion. Figure 1 gives the results of comparing the numerical calculations of the disruption probability for a $CrNi_6$ system with the experimental data.[6]

First, it should be noted that at low temperatures (below 20 K), disruption in this system is fairly adequately described by thermal-assisted tunneling (curves *1* and *2*). For comparison we also give curve *3*, which is plotted assuming independent tunneling and thermal activation processes as proposed by Keren *et al.*[6] In order to explain the difference between the behavior of curve *3* and the experimental data, the authors[6] assumed that a first-order phase transition from tunneling to thermal activation takes place near 6 K, although the physical reasons for this were not discussed.

Second, we note that sections of nonmonotonic behavior of $P_{\mathrm{tot}}(T)$ are observed at $T \lesssim 10$ K as a result of the influence of decoherence effects (curve *1*). Since the coupling constant C for these materials is as yet unknown and in our calculations essentially served as a fitting parameter, detailed agreement between the results of the numerical modeling and the experimental data can hardly be expected. However, the behavior of these characteristics may serve as a sufficiently reliable indicator that decoherence does occur. It is then highly desirable to obtain more detailed data on the behavior of the curve $P_{\mathrm{tot}}(T)$ below 10 K which could also be used to refine the coupling constant.

[1] E. M. Chudnovsky, Phys. Rev. A **46**, 8011 (1992).
[2] D. A. Garanin and E. M. Chudnovsky, Phys. Rev. B **56**, 11 102 (1997).
[3] S. P. Kou, Phys. Rev. B **59**, 6309 (1999).
[4] V. V. Makhro, J. Phys.: Condens. Matter **10**, 6911 (1998).
[5] V. V. Makhro, LANL *e*-print, Cond-mat/9807262 (Los Alamos eprint server, 1998).
[6] A. Keren, P. Mendels, A. Kratzer *et al.*, LANL *e*-print, Cond-mat/9806230 (Los Alamos eprint server, 1998).
[7] F. Grossman, T. Dittrich, P. Jung, and P. Hänggi, Phys. Rev. Lett. **67**, 516 (1991).
[8] J. M. Gomez Llorente and J. Plata, Phys. Rev. A **45**, 6958 (1992).
[9] L. Wang and J. Shao, Phys. Rev. A **49**, 637 (1994).
[10] Y. Kayanuma, Phys. Rev. A **50**, 843 (1994).

Translated by R. M. Durham

Nature of hyperthermal surface ionization

V. N. Ageev and S. Yu. Davydov

A. F. Ioffe Physicotechnical Institute, Russian Academy of Sciences, St. Petersburg
(Submitted March 23, 1999)
Pis'ma Zh. Tekh. Fiz. **25**, 6–11 (August 26, 1999)

A model of electron-stimulated desorption is used as the basis to propose a simple theory of hyperthermal surface relaxation of atoms at metal and semiconducting substrates. The dependence of the ion flux on the kinetic energy of the scattered atoms is obtained near the ionization threshold. © *1999 American Institute of Physics.* [S1063-7850(99)01708-5]

The phenomenon of surface ionization under conditions of thermal equilibrium has been thoroughly studied and is widely used to obtain ion currents.[1–3] When an atom or molecule collides with a metal surface, the ion flux J_i leaving the surface is determined by the Saha–Langmuir formulas: the positive ion flux J^+ is proportional to $\exp[(\phi-I)/k_BT_s]$, where ϕ is the work function, I is the ionization energy of the atom (molecule), k_B is the Boltzmann constant, and T_s is the surface temperature. For negative ions we have $J^- \propto \exp[(A-\phi)/k_BT_s]$, where A is the electron affinity. However, if neutral particles (neutrals) impinge on a surface at superthermal velocity, the ion component of the scattered flux is far greater than that predicted by the Saha–Langmuir theory. As the kinetic energy of the incident neutrals increases, the ion yield increases.[4–9] This phenomenon is known as hyperthermal surface ionization. In the present paper we propose a simple analytical model for hyperthermal surface ionization based on the Menzel–Gomer–Redhead approximation[10,11] to describe the reneutralization of ions leaving a metal surface. We shall consider a neutral particle incident on a metal surface, having the kinetic energy E_{in}. If, as a result of the collision with the surface, an electron is not transferred from the particle to the metal (or from the metal to the particle), the scattered particle remains in the neutral state and leaves the surface with the same kinetic energy E_{in} provided that the scattering is elastic. However, if an electron is transferred as a result of the collision, a positive (negative) ion is removed from the surface with a kinetic energy whose magnitude can be determined from the energy conservation law:

$$E(z)=E_{\text{in}}-\frac{e^2}{4z^*}+\frac{e^2}{4z}, \tag{1}$$

where z is the distance between the surface and the outgoing singly charged ion, z^* is the turning point, at which it is assumed that the neutral becomes ionized, and e is the positron charge. It follows from Eq. (1) that the threshold energy E^*, i.e., the energy sufficient for the product ion to leave the surface, is given by

$$E^*=e^2/4z^*. \tag{2}$$

In accordance with the Menzel–Gomer–Redhead approximation,[10,11] the probability P_i of a positive (negative) ion leaving the surface without being neutralized by the metal electrons (without transferring an excess electron to the metal) is

$$P_i=\exp\left[-(2/\hbar)\int_{z^*}^{\infty}dz\,\frac{\Gamma(z)}{v(z)}\right], \tag{3}$$

where $\hbar$ is Planck's constant. The half-width of the ion quasilevel Γ is given by

$$\Gamma(z)=\Gamma^*\exp[-2\gamma(z-z^*)], \tag{4}$$

where Γ^* is the quasilevel half-width at the turning point and γ is the characteristic reciprocal interaction length.[12] The normal ion velocity is

$$v(z)=\sqrt{2E(z)/M}, \tag{5}$$

where M is the ion mass.

Substituting Eq. (5) into Eq. (3), we obtain

$$P_i=\exp(-CS),$$

$$C=2\sqrt{2M}\,(\Gamma^*/\hbar eQ)\exp(\alpha)\,(z^*)^{3/2},$$

$$S(\varepsilon,\alpha)=\int_1^{\infty}dx\exp(-\alpha x)\,\sqrt{x/(\varepsilon x+1)}, \tag{6}$$

$$\alpha\equiv 2\gamma z^*,\quad x\equiv z/z^*,\quad \varepsilon\equiv(E_{\text{in}}-E^*)/E^*.$$

It follows from expression (6) that in the high-energy limit ($\varepsilon\gg 1$), we have

$$S(\varepsilon,\alpha)\cong\alpha^{-1}\exp(-\alpha)\,\varepsilon^{-1/2}, \tag{7}$$

which shows complete agreement with the theory of charge transfer for particles having energies of the order of a few tens of electronvolts at a metal surface,[12,13] where it was shown that the probability of ion drift is proportional to $\exp(-\text{const}/v)$. In the low-energy (near-threshold) limit ($\varepsilon\ll 1$), we can show that

$$S(\varepsilon,\alpha)_{\varepsilon\to 0}\cong\alpha^{-3/2}\left[\Gamma(3/2,\alpha)-\frac{\varepsilon}{2}\Gamma(5/2,\alpha)\right], \tag{8}$$

where $\Gamma(i,j)$ is an incomplete gamma function.[14] Thus, in the low-energy limit we find

$$P_i=P_i^*\,\overline{P}_i,$$

$$P_i^* \cong \exp\left[-\sqrt{M}\,\frac{\Gamma^*}{\hbar e \gamma^{3/2}}\, f(3/2,\alpha)\right], \tag{9}$$

$$\overline{P_i} \cong \exp\left[\sqrt{M}\,\frac{\Gamma^*}{\hbar e \gamma^{3/2}}\, f(5/2,\alpha)\,\frac{\varepsilon}{2}\right],$$

where $f(i,\alpha)=\exp(\alpha)\,\Gamma(i,\alpha)$. For $\alpha>2$ which is a general case, since $\gamma \cong 1$ Å^{-1}, we obtain $z^* \geqslant 1$ Å (Refs. 4, 12, and 13), $f(3/2,\alpha)\cong\sqrt{\alpha}$, and $f(5/2,\alpha)\cong(\alpha+3/2)\sqrt{\alpha}$.

We know from the theory of charge transfer in the scattering of atoms at a metal surface[12,13,15] that there is a certain critical distance between the atom and the surface z_c at which the atomic level E_a intersects the Fermi level E_F separating the regions of high ($z<z_c$) and low ($z>z_c$) ionization probability. The distance z_c for the creation of a positive ion may be determined from

$$\phi - I + e^2/4z_c = 0. \tag{10}$$

For a negative ion the equivalent equation has the form

$$\psi - A - e^2/4z_c = 0. \tag{11}$$

Clearly the turning and ionization point z^* introduced by us should satisfy the condition $z^* \leqslant z_c$.

In order to analyze the experimental data on hyperthermal surface ionization we shall determine the energy dependence of the logarithm of the ion current in the low-energy limit

$$\xi_i = (\partial \ln J_i / \partial E_{\text{in}})_{E_{in}\to E^*}. \tag{12}$$

Since $J_i \propto P_i$, only the cofactor $\overline{P_i}$ from Eq. (9) makes any contribution to ξ_i. We obtain

$$\xi_i = \sqrt{M}\,\frac{\Gamma^*}{2\hbar e E^* \gamma^{3/2}}\, f(5/2,\alpha). \tag{13}$$

The experimental data on hyperthermal surface ionization will be analyzed as follows. We shall take the experimental threshold energy E^* and determine the ionization (turning) point z^* for it using Eq. (1). Then, by finding the critical point z_c from Eqs. (10) or (11), we determine whether these values satisfy the inequality $z^* \leqslant z_c$. The next step is to determine the half-width of the atomic quasilevel Γ^* from the experimentally determined slope ξ_i of the curve of the logarithm of the ion yield, linearized near the threshold energy.

Table I gives results of an analysis of experiments on the hyperthermal surface ionization of benzene molecules at an oxidized rhenium surface,[9] anthracene at the surface of diamond,[5,6] and $N(C_2H_4)_3N$ at pure and oxidized (111) platinum surfaces.[8] It can be seen that in all these cases the inequality $z^* \leqslant z_c$ is satisfied. The values of Γ^* are also quite reasonable: in Ref. 4 where hyperthermal surface ionization of alkali metal atoms was studied at an Si(111) surface, quasilevel half-widths of the order of tenths of an electron-volt were obtained for the adsorption of potassium on graphite, 0.1 eV (Ref. 16).

To sum up, we have proposed a simple analytic expression to describe hyperthermal surface ionization. The higher ion yield obtained for hyperthermal surface ionization compared with surface ionization of particles in thermal equilibrium with a solid can be attributed to the fact that in the first case, the energy of the incident particles is $E_{\text{in}} \gg k_B T_s$. As the kinetic energy E_{in} increases, the velocity of an ion moving away from the surface increases and the probability P_i of its departing to infinity without being neutralized, increases. It can be shown that this effect is suppressed to some extent by increased broadening of the quasilevel Γ^* at the turning point z^* since the incident atom will approach closer to the surface. At the same time, a decrease in z^* leads to an increased ionization probability.

TABLE I. Experimental data (I, ϕ, E^*, eV; ξ_i, eV^{-1}) and calculated results (r^*, r_c, Å; Γ^*, eV).

Value	Benzene/ rhenium	Anthracene/ diamond	$N(C_2H_4)_3N$/Pt(111)	
			pure Pt	oxidized Pt
I	8.82	7.55	7.25	
ϕ	7.2	6.1	5.7	5.9
E^*	3	3	2	2
ξ_i	3.94	4.14	9.21	6.14
r^*	1.20	1.20	1.80	1.80
r_c	2.22	2.48	2.32	2.67
Γ^*	0.11	0.08	0.09	0.06

For practical purposes it is convenient to use the expression for the ion current

$$J_i \propto \exp(-C_1 + C_2\varepsilon), \tag{14}$$

where $C_1 = -\ln P_i^*$, $C_2 = (1/\varepsilon)\ln \overline{P_i}$ [see Eq. (9)].

The authors are grateful to U. Kh. Rasulev for useful discussions.

This work was carried out under the Federal Program ''Surface Atomic Structures.''

[1] N. I. Ionov, Prog. Surf. Sci. **1**(2), 237 (1972).
[2] É. Ya. Zandberg and N. I. Ionov, *Surface Ionization* [in Russian], Nauka, Moscow (1969), 432 pp.
[3] U. Kh. Rasulev and E. Ya. Zandberg, Prog. Surf. Sci. **28**(1), 181 (1988).
[4] Y. Bu, E. F. Greene, and D. K. Stewart, J. Chem. Phys. **92**, 3899 (1990).
[5] A. Danon and A. Amirav, J. Phys. Chem. **93**, 5549 (1989).
[6] A. Danon and A. Amirav, Int. J. Mass Spectrom. Ion Processes **96**(1), 139 (1990).
[7] A. Danon, A. Vardi, and A. Amirav, Phys. Rev. Lett. **65**, 2038 (1990).
[8] A. Amirav, Org. Mass Spectrom. **26**(1), 1 (1991).
[9] H. Kishi and T. Fujii, J. Phys. Chem. **99**, 11 153 (1995).
[10] D. Menzel and R. Gomer, J. Chem. Phys. **41**, 1164 (1964).
[11] P. A. Redhead, Can. J. Phys. **42**, 886 (1964).
[12] R. Brako and D. M. Newns, Rep. Prog. Phys. **52**, 655 (1989).
[13] J. Los and J. J. C. Geerlings, Phys. Rep. **190**(3), 133 (1990).
[14] I. S. Gradshteyn and I. M. Ryzhik, *Tables of Integrals, Series, and Products*, transl. of 4th Russ. ed. (Academic Press, New York, 1980) [Russ. original, 5th ed., Nauka, Moscow, 1971, 1108 pp.].
[15] W. L. Clinton and S. Pal, Phys. Rev. B **41**(15), 15 (1990).
[16] A. Sandell, O. Hjorstram, A. Nilsson, P. A. Bruhwiler, O. Eriksson, P. Bennich, P. Rudolf, J. M. Wills, B. Johansson, and N. Martensson, Phys. Rev. Lett. **78**, 4994 (1997).

Translated by R. M. Durham

Bifurcations in the trajectory problem as a cause of internal-time singularities and the onset of quantum (wave) chaos

A. V. Bogdanov, A. S. Gevorkyan, and A. G. Grigoryan

Institute for High-Performance Computing and Databases, St. Petersburg
(Submitted April 22, 1999)
Pis'ma Zh. Tekh. Fiz. **25**, 12–22 (August 26, 1999)

A new theory is proposed for quantum-mechanical multichannel scattering in a collinear three-body system. This simple problem is used to show that the principle of quantum determinism is generally violated and we are dealing with microirreversible quantum mechanics. Fundamental calculations of quantum (wave) chaos are presented for the first time for the elementary reaction $Li+(FH)\rightarrow(LiFH)^*\rightarrow LiF+H$. © *1999 American Institute of Physics.* [S1063-7850(99)01808-X]

At the early stages in the development of quantum mechanics, Einstein posed a question which has attracted universal attention several decades later.[1] The question was: how will a classical chaotic system behave in the quantum case? As a clear example, Einstein specifically referred to a three-body system.

The present authors have already studied the problem of quantum chaos for quantum-mechanical scattering in a collinear three-body system.[2,3] We showed that this problem can be reduced to the problem of an anharmonic oscillator with nontrivial time (internal time) which can generally exhibit chaotic behavior. In the present study, we continue our investigations of the problem of quantum chaos using numerical calculations for an elementary chemical reaction.

1. FORMULATION OF THE PROBLEM

The problem of quantum multichannel scattering can be represented schematically using a collinear model as follows:

$$A+(BC)_n\rightarrow\begin{cases}A+(BC)_m\\(AB)_m+C\\A+B+C\\(ABC)^*\rightarrow\begin{cases}A+(BC)_m\\(AB)_m+C\\A+B+C,\end{cases}\end{cases}\qquad(1)$$

where m and n are the vibrational quantum numbers corresponding to the (in) and (out) scattering channels. It was shown in our previous studies[2,3] that the problem of quantum multichannel scattering (1) can be formulated as the evolution of a wave packet on the manifold M (fiber bundle of the Lagrange surface S_p) in terms of a local coordinate frame moving on S_p

$$S_p=\{x^1;x^2;2\mu_0(E-V(x^1,x^2))>0\},$$
$$\mu_0=\left\{\frac{m_Am_Bm_C}{m_A+m_B+m_C}\right\}^{1/2},\qquad(2)$$

where m_A, m_B, and m_C are the masses of the corresponding particles, and E and $V(x^1,x^2)$ are the total energy and interaction potential of the system, respectively. The metric on the surface S_p is introduced as follows:

$$g_{ik}=P^2(x^1,x^2)\,\delta_{ik},\quad P^2(x^1,x^2)=2\mu_0(E-V(x^1,x^2)).\qquad(3)$$

The motion of the local coordinate system is determined by the projection of the motion of a mapping point with the reduced mass μ_0 onto the extremal ray $\mathfrak{I}_{\rm ext}$ of the Lagrange manifold S_p. Note that for the scattering problem (1) there are two extreme rays on the surface S_p: one connects the (in) channel to the (out) channel of the regrouping reaction while the second connects the (in) and (out) channels of the dissociation reaction. We shall subsequently study the regrouping reaction.

We shall introduce the curvilinear coordinate system (x^1,x^2) on the Euclidean space R^2 along the projection of the extremal ray $\bar{\mathfrak{I}}_{\rm ext}$ such that x^1 varies along $\bar{\mathfrak{I}}_{\rm ext}$, and x^2 varies in the perpendicular direction. In this case, the trajectory of the mapping point is described by the following system of second-order differential equations:

$$x^k_{;ss}+\left\{\frac{k}{ij}\right\}_{S_p}x^i_{;s}x^j_{;s}=0\quad(i,j,k=1,2),\qquad(4)$$

where

$$x^i_{;s}=\frac{dx'}{ds}\ \text{ and }\ \left\{\frac{k}{ij}\right\}_{S_p}=\frac{1}{2}g^{kl}\left(\frac{\partial g_{lj}}{\partial x^i}+\frac{\partial g_{il}}{\partial x^j}-\frac{\partial g_{ij}}{\partial x^l}\right).$$

Equation (4) with the initial conditions

$$x^i_0=x^i(-\infty),\quad x^i_0=x^i_{;t}(-\infty)\qquad(5)$$

at any time t has the unique solution $x^i(t)$ and $\dot{x}^i(t)$, i.e., the geodesic trajectory and the geodesic velocity.

We shall now make a quantum analysis of the regrouping process. Note that in the quasiclassical limit this analysis is equivalent to describing the trajectory flux on the Lagrange surface S_p. This trajectory flux can be conveniently studied in a local coordinate system whose motion is determined by the solution $x^1(s)$ of the system (4). The cor-

responding flux should be quantized in this coordinate system on the fiber bundle M of the Lagrange surface S_p.

Bearing this reasoning in mind, we can write the Schrödinger equation for the system of bodies in terms of the moving local frame of reference:[4,5]

$$\{\hbar^2\gamma^{-\frac{1}{2}}\{\partial_{x^1(s)}[\gamma^{ij}\gamma^{\frac{1}{2}}\partial_{x^1(s)}]+\partial_{x^2(s)}[\gamma^{ij}\gamma^{\frac{1}{2}}\partial_{x^2(s)}]\}$$
$$+P^2(x^1(s),x^2(s))\}\Psi=0,$$
$$\partial_{x^i(s)}=\partial/\partial x^i(s), \tag{6}$$

where

$$\gamma_{11}=\left(1+\frac{\lambda(x^1(s))}{\rho_1(x^1(s))}\right)^2, \quad \gamma_{22}=\left(1+\frac{x^2}{\rho_2(x^1(s))}\right)^2,$$
$$\gamma_{12}=\gamma_{21}=0, \quad \gamma=\gamma_{11}\gamma_{22}>0. \tag{7}$$

In formula (6) λ is the de Broglie wavelength on $\Im_{\text{ext}}$, and ρ_1 and ρ_2 are the principal curvatures of the surface S_p at the point $x^1\in\bar{\Im}_{\text{ext}}$ in the direction of the coordinates x^1 and x^2.

The main difference between Eq. (6) and the Schrödinger equation is that the independent coordinate $x^1(s)$ is a solution of a system of nonlinear differential equations and thus is not generally a natural parameter. Moreover, under certain conditions it may be a stochastic function.

Our task is to find a solution of Eq. (6) which would satisfy the following asymptotic conditions for the complete wave function of the system of bodies:

$$\lim_{(s,x^1)\to-\infty}\Psi^{(+)}(x^1(s),x^2)$$
$$=\Psi_{\text{in}}(n;x^1,x^2)+\sum_{m\neq n}R_{mn}\Psi_{\text{in}}(m;x^1,x^2),$$

$$\lim_{(s,x^1)\to+\infty}\Psi^{(+)}(x^1(s),x^2)=\sum_m S_{mn}\Psi_{\text{out}}(m;x^1,x^2), \tag{8}$$

where the coefficients R_{mn} and S_{mn} are the amplitudes of the probabilities of excitation and regrouping, respectively.

The following analytical study of Eq. (6) with the boundary conditions (8) can only be made after simplifying this equation.

2. SOLUTION OF THE SCHRÖDINGER EQUATION ON THE MANIFOLD $M(\Im(u))$

Bearing in mind that the wave function is localized along the reaction coordinate $\Im$, and using the parabolic equation method[6] for this problem, we can express the solution of Eq. (6) in the form

$$\Psi^{(+)}(x^1(s),x^2)=\exp\left(i\hbar^{-1}\int_0^{x^2(s)}p(x^1)\sqrt{\gamma_0}dx^1\right)$$
$$\times A(x^1(s),x^2), \tag{9}$$

where $\gamma_0=\gamma(x^1(s),x^2)|_{x^2=0}$ and $p(x^1(s))=P(x^1(s),x^2)|_{x^2=0}$.

After transforming the coordinates in expression (6)

$$\tau=(E)^{-1}\int_0^{x^1(s)}p(x^1)\sqrt{\gamma_0}dx^1, \quad z=(\hbar E)^{-\frac{1}{2}}p(x^1(s))x^2$$

taking into account the quasiclassical approximation,[7] we can obtain the complete wave function of the three-particle system in the harmonic approximation

$$\tilde{\Psi}^{(+)}(n;z,\tau)=\left[\frac{(\Omega_{\text{in}}/\pi)^{\frac{1}{2}}}{2^n n!|\xi|}\right]^{\frac{1}{2}}\exp[i\hbar^{-1}S_{\text{eff}}(z,\tau)]H_n$$
$$\times\left[\frac{\sqrt{\Omega_{\text{in}}}}{|\xi|}(z-\eta)\right], \tag{10}$$

$$S_{\text{eff}}(z,\tau)=S_{cl}(\tau)-E_v^i\int_0^\tau|\xi|^{-2}d\tau'+\left\{\dot{\eta}(z-\eta)\right.$$
$$\left.+\frac{1}{2}\dot{\xi}\xi^{-1}(z-\eta)^2-\frac{1}{2}\dot{p}p^{-1}z^2\right\},$$

$$S_{cl}(\tau)=E\tau-E\int_{-\infty}^{\tau}\left\{\frac{1}{2}[(\dot{\eta})^2-\Omega^2(\tau')\eta^2]+F(\tau')\eta\right\}d\tau',$$

$$E_v^i=\hbar\Omega_{\text{in}}\left(n+\frac{1}{2}\right). \tag{11}$$

We recall that the function $\xi(\tau)$ is a solution of the classical oscillator problem

$$\ddot{\xi}+\Omega^2(\tau)\xi=0,$$
$$\Omega^2(\tau)=-\left(\frac{E}{p}\right)^2\left\{\frac{1}{p_2^2}+\sum_{k=1}^{2}\left[\frac{p_{;kk}}{p}+\left(\frac{p_{;k}}{p}\right)^2\right]\right\},$$
$$p_{;k}=\frac{dp}{dx^k} \tag{12}$$

with the asymptotic behavior

$$\xi(\tau)_{\tau\to-\infty}\sim\exp(i\Omega_{\text{in}}\tau_-),$$
$$\xi(\tau)_{\tau\to+\infty}\sim c_1\exp(i\Omega_{\text{out}}\tau_+)-c_2\exp(-i\Omega_{\text{out}}\tau_+), \tag{13}$$

where $\tau_-=2\mu_0x^1/p_-$ and $\tau_+=2\mu_0x^1/p_+$ are the internal time in the asymptotic subspaces R_{in}^2 and R_{out}^2, respectively, the momenta in the asymptotic form are defined as $p_\mp=\lim_{x^1\to\mp\infty}p(x^1)$, and the constants c_1 and c_2 are obtained by solving Eq. (12).

The function $\eta(\tau)$ is expressed in terms of the solution of the homogeneous equation (12):

$$\eta(\tau)=(2\Omega_{\text{in}})^{-\frac{1}{2}}[\xi(\tau)d^*(\tau)+\xi^*(\tau)d(\tau)],$$
$$\eta(-\infty)=\dot{\eta}(-\infty)=0,$$
$$d(\tau)=(2\Omega_{in})^{-\frac{1}{2}}\int_{-\infty}^{\tau}d\tau'\,\xi(\tau')F(\tau'),$$

$$F(\tau)=\frac{(E)^{\frac{3}{2}}}{\hbar^{\frac{1}{2}}}\frac{1}{p}\left[\frac{p_{;2}}{p}-\frac{1}{\rho_2}\right]. \tag{14}$$

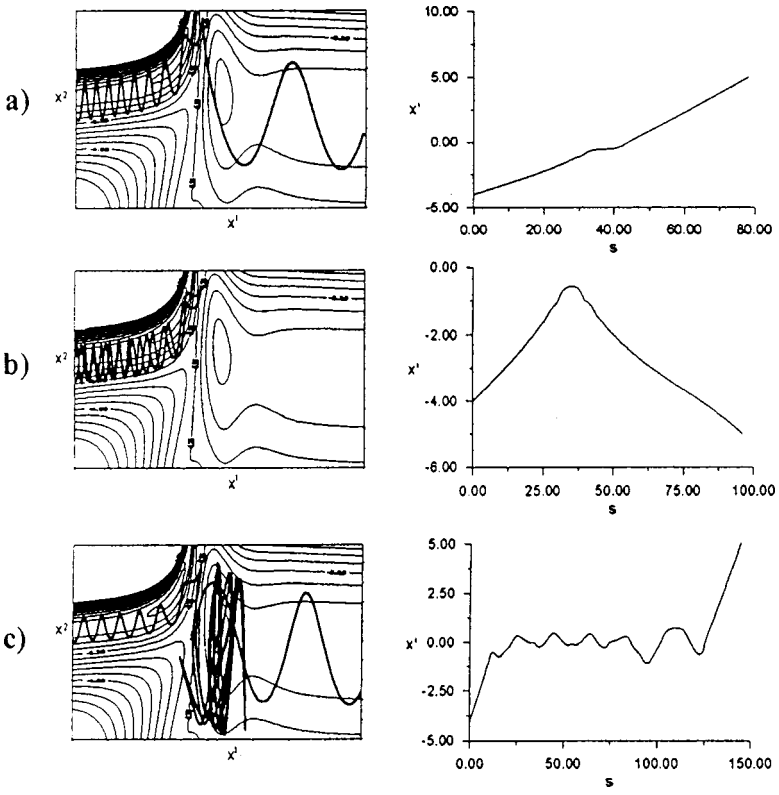

FIG. 1. Geodesic trajectories and dependence of the internal time on the natural parameter for: a — a direct regrouping reaction, b — a direct reflection reaction, and c — a regrouping reaction taking place via a resonant state.

Note that in the limit $\tau \to -\infty$ the exact wave function (10) goes to its asymptotic value — the wave function of a harmonic oscillator at the frequency Ω_{in}.

3. EXACT REPRESENTATION FOR THE *S*-MATRIX IN TERMS OF INTERNAL TIME. PROBABILITY OF A REGROUPING TRANSITION

We shall analyze an exact representation for the *S*-matrix in terms of the complete wave functions of the (in) and (out) states[8]

$$\Psi^{(+)}(n;x^1(s)x^2) = \sum_k S_{kn}\Psi^{(-)}(k;x^1(s),x^2). \tag{15}$$

Bearing in mind that the asymptotic wave functions form a basis set in the R^2_{out} space, after projecting expression (15) onto the asymptotic state in the limit $x^1 \to +\infty$, we can obtain the following expression:

$$S_{mn} = \lim_{(s,x^1)\to+\infty} \langle \Psi^*_{\text{out}}(m;x^1,x^2)\Psi^{(+)}(n;x^1,x^2)\rangle_{x^2}$$
$$= \lim_{\tau\to+\infty} \langle \tilde{\Psi}^*_{\text{out}}(m;z_+,\tau_+)\tilde{\Psi}^{(+)}(n;z,\tau)\rangle_z,$$

$$\langle \ldots \rangle_z = \int_{-\infty}^{+\infty} dz. \tag{16}$$

We have thus obtained a new representation for the *S*-matrix which is one integration smaller than the standard one. Since in this case, the variable $x^1(s)$ or τ plays the role of the natural parameter s (normal time) in scattering theory, in expression (16), following Prigogine,[9] by analogy with the nonsteady-state representation of the *S*-matrix, we shall call τ the ''internal'' time of the three-body system

We shall use the exact representation of the *S*-matrix (16) to calculate the amplitude of the probability of a reaction transition. Using expression (10) for the complete wave function and expression (16) for its asymptotic limit, we obtain a final expression for the probability amplitude of the reaction transition $A+(B,C)_n \to (ABC)^* \to (A,B)_m + C$, which takes place via the formation of a resonant complex:

$$W_{mn} = |S_{mn}|^2 = \frac{(1-\theta)^{1/2}}{m!n!}|H_{mn}(b_1,b_2)|^2$$
$$\times \exp[-\nu(1-\sqrt{\theta}\cos 2\varnothing)]. \tag{17}$$

Here the function $H_{mn}(b_1 b_2)$ denotes a complex Hermite polynomial and in addition:

$$b_1 = \sqrt{\nu(1-\theta)}\exp(i\varnothing),$$

$$b_2 = -\sqrt{\nu}[\exp(-i\varnothing) - \sqrt{\theta}\exp(i\varnothing)],$$

$$\varnothing = \frac{1}{2}(\delta_1+\delta_2) - \beta. \tag{18}$$

The variables θ, δ_1, δ_2, β, and ν are determined by the coefficients c_1 and c_2, and by the solution $\xi(\tau)$ (see Ref. 10)

$$c_1 = e^{i\delta_1}(\Omega_{\text{in}}/\Omega_{\text{out}})^{\frac{1}{2}}(1-\theta)^{-\frac{1}{2}},$$

$$c_2 = e^{i\delta_2}(\Omega_{\text{in}}/\Omega_{\text{out}})^{\frac{1}{2}}[\theta/(1-\theta)]^{\frac{1}{2}} \quad \theta = |c_2/c_1|^2,$$

$$d = \lim_{\tau\to+\infty} d(\tau) = \sqrt{\nu}\exp(i\beta). \tag{19}$$

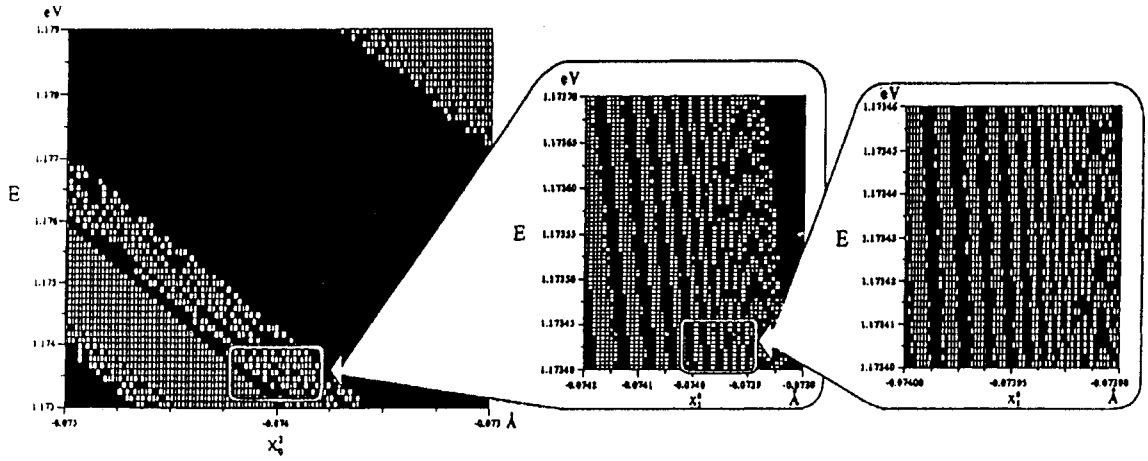

FIG. 2. Irregular pattern of initial values of the total energy E and the coordinate x_0^2 for transmitted (white squares) and reflected (black squares) geodesic trajectories.

4. INVESTIGATION OF THE DEPENDENCE OF THE INTERNAL TIME ON THE NORMAL TIME OR NATURAL PARAMETER

We shall now proceed to prove that chaos may appear in the wave function of three-body systems (10), which we shall call quantum chaos. We stress that in this case, the behavior of the transition probability as a function of the properties of the classical trajectory will also be irregular. For this it is sufficient to show that the solution $x^1(s)$ is unstable or chaotic for some initial conditions. We made a detailed study of the behavior of the mapping point trajectory on the Lagrange surface S_p for the elementary chemical reaction $\mathrm{Li}+(\mathrm{FH})_n \rightarrow (\mathrm{LiFH})^* \rightarrow (\mathrm{LiF})_m + \mathrm{H}$. The potential interaction surface of this reaction was reproduced using quantum-mechanical calculations performed in Ref. 11. It was shown that if the beginning of the geodesic trajectory x_0^2 in the (in) channel is fixed (i.e., $x^1 \rightarrow -\infty$), then for the total system energy $E \geqslant 1.4$ eV the behavior of the trajectories [in the sense that they propagate into the (out) or reflect into the (in) channels] alternates regularly (Figs. 1a and 1b).

From $E = 1.4$ eV and as far as the threshold reaction energy of 1.1 eV, the geodesic trajectories exhibit unstable behavior as a function of energy which sometimes leads to their total mixing in the intermediate region and results in the formation of a resonant complex (LiFH)* (Fig. 1c).

Numerical calculations of the leading Lyapunov exponent showed that this has positive values for the entire energy range. However, from 1.4 eV and above, this exponent increases negligibly. In the energy range between 1.4 and 1.1 eV the leading Lyapunov exponent increases rapidly which indicates that the trajectories diverge exponentially. For this energy range the regular alternation of the propagating and reflected trajectories is impaired and a region of stochastic trajectory behavior is formed. Numerical investigations in this range showed that this region of chaotic trajectory behavior is self-similar relative to scale transformation (Fig. 2).

For the given initial values, the evolution of the corresponding classical problem is chaotic and the motion of the local coordinate system is also stochastic. It is easy to see that in this situation, the behavior of $x^1(s)$ is also chaotic, and this is also true for the internal time $\tau(x^1(s))$ which is essentially the time scale parameter of the quantum evolution in the three-body system.

It can be shown that the chaotic behavior of the internal time $\tau(x^1(s))$ also leads to stochastic behavior of the solution of the standard equation $\xi(\tau(x^1(s)))$. This also holds for the representation of the wave function (10) and the transition probability (18). Thus, a strict analysis of the simple model of multichannel scattering (1) using the system of equations (4) and (6) shows that the principle of quantum determinism is violated and quantum chaos appears.

Finally, we stress that these results agree with the theory of a transition complex (see Ref. 12) which essentially involves a stochastic description of chemical reactions. In addition, this representation can also be used to provide an answer to Einstein's objection regarding the irreducibility of quantum mechanics to classical chaotic dynamics. We have studied the amplitude of the regrouping probability for the reaction $\mathrm{Li}+(\mathrm{FH})_n \rightarrow (\mathrm{LiFH})^* \rightarrow (\mathrm{LiF})_m + \mathrm{H}$ and we have shown that in regions where there are many internal-time singularities, this is stochastic. We have also shown that this representation satisfies the constraints of going to the limit, including the transition from the Q_{ch} region to the P region. This transition takes place as $\hbar$ tends to zero and for $E_k^i < E_c$.

[1] A. Einstein, Verh. Dtsch. Phys. Ges. **19**, 82 (1917).
[2] A. V. Bogdanov and A. S. Gevorkyan, in *Proceedings of the International Symposium on Nonlinear Theory and its Applications*, Hawaii, 1997, Vol. 2, pp. 693–696.
[3] A. V. Bogdanov and A. S. Gevorkyan, *Multichannel Scattering Closed Three-Body System as a Example of Irreversible Quantum Mechanics*, LANL E-print quant-ph/9712022 (Los Alamos National Laboratory e-Print archive, 1997).
[4] A. V. Bogdanov and A. S. Gevorkyan, *Multichannel Scattering in a Collinear Three-Body System as an Example of Irreducible Quantum Mechanics*, Preprint No. IVViBD-1-97 [in Russian] Institute for High-Performance Computing and Databases, St. Petersburg (1997).
[5] A. V. Bogdanov, A. S. Gevorkyan, A. G. Grigoryan, and S. A. Matveev (accepted for publication) Int. J. Bifurcat. Chaos.

[6] V. M. Babich and B. S. Buldyrev, *Asymptotic Methods in the Problem of Short Wave Diffraction* [in Russian], Nauka, Moscow (1972).
[7] A. V. Bogdanov and A. S. Gevorkyan, in *Proceedings of International Workshop QS-96*, Minsk, Belarus, 1996, pp. 34–40.
[8] R. G. Newton, *Scattering Theory of Waves and Particles* (McGraw-Hill, New York, 1966).
[9] I. Prigogine, *From Being to Becoming: Time and Complexity in the Physical Sciences* (Freeman, San Francisco, 1980).
[10] A. I. Byaz', Ya. B. Zel'dovich, and A. M. Perelomov, *Scattering, Reactions, and Decay in Nonrelativistic Quantum Mechanics* [in Russian], Nauka, Moscow (1971).
[11] S. Carter and J. N. Murrell, Mol. Phys. **41**, 567 (1980).
[12] E. E. Nikitin, *Theory of Elementary Atomic Molecular Processes in Gases* [in Russian], Khimiya, Moscow (1970).

Translated by R. M. Durham

Electrical properties of Schottky diodes using high-resistivity CdTe crystals

V. O. Ukrainets, G. A. Il'chuk, N. A. Ukrainets, Yu. V. Rud', and V. I. Ivanov-Omskiĭ

Lvov Polytechnic State University;
A. F. Ioffe Physicotechnical Institute, Russian Academy of Sciences, St. Petersburg
(Submitted March 15, 1999)
Pis'ma Zh. Tekh. Fiz. **25**, 23–28 (August 26, 1999)

The Schottky barrier height is measured for single crystals doped with the halogens Cl, Br, and I during growth by chemical transport reactions. The measurements are made using a modification of the $F(V)$ function [N. V. Agrinskaya, Mater. Sci. Eng. B **16**, 172 (1993)] proposed by the authors. © *1999 American Institute of Physics.* [S1063-7850(99)01908-4]

Cadmium telluride is one of the most promising materials for fabricating high-efficiency counters for penetrating radiation.[1,2] With a view to realizing this possibility, research has been carried out over many years to produce semi-insulating single crystals of this compound by adding vapor-phase chlorine to a flux. It has recently been established that semi-insulating cadmium telluride can also be prepared using the chemical transport reaction method, when the halogens themselves participate in the growth process as a constituent component of the carriers used.[3] This study is part of a series and its aim is to characterize a halogen-doped high-resistivity material, and specifically to determine the parameters of Schottky barriers using these single crystals.

A consequence of the high series resistance of a Schottky diode is that the current–voltage characteristic ceases to be linear in the semilogarithmic scale $\ln I = f(V)$ used, in particular, to determine the barrier height.

Norde[4] analyzed the influence of the series resistance on the current–voltage characteristic of an *n*-Si Schottky diode with a thermionic current mechanism and suggested that the experimental current–voltage characteristic could be expressed in the form

$$F(V) = \frac{V}{2} - \frac{kT}{q} \ln \frac{I}{AA^{**}T^2}, \tag{1}$$

which, when plotted graphically, can be used to determine the barrier height φ_B on the metal side and the series resistance of the structure. Here V is the voltage applied to the diode, I is the current, A^{**} is the Richardson constant, A is the barrier area, $F(V)$ is the Norde function, T is the absolute temperature, k is the Boltzmann constant, and q is the elementary charge.

We investigated Me(In,Sn)–*p*-CdTe diodes ($p = 10^8$–$10^{10}\,\mathrm{cm}^{-3}$, $T = 293\,\mathrm{K}$) having a high base resistance, which differ fundamentally from those studied in Ref. 4 because of the diffusion mechanism of current flow caused by the low hole mobility in *p*-CdTe [$\mu_p \leqslant 50\,\mathrm{cm}^2/(\mathrm{V}\cdot\mathrm{s})$]. The current–voltage characteristics of these structures plotted in the coordinates $\ln I = f(U)$ are nonlinear and determining the base resistance from the I–V dependence yields multivalued results. Hence, the search for optimum methods of analyzing the I–V characteristics to determine the parameters of a structure fabricated using high-resistivity materials can be considered to be highly topical.

In order to measure the barrier height of Me(In,Sn)–*p*-CdTe structures, we modified expression (1) to the case of barriers with a diffusion mechanism of current flow. We know that in diffusion theory of a metal–semiconductor

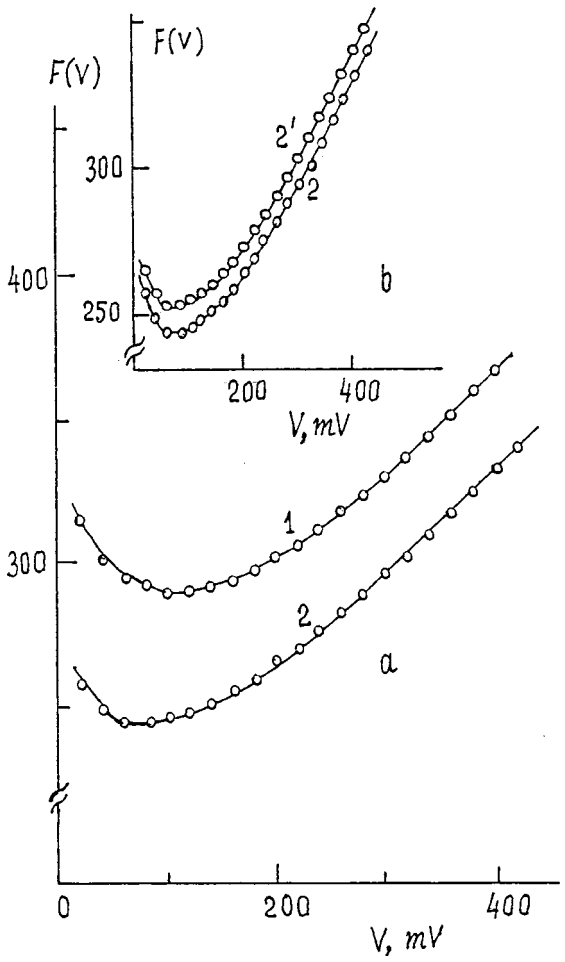

FIG. 1. Experimental $F(V)$ dependences for two Sn–*p*-CdTe Schottky diodes D1 and D2 (curves *1* and *2*, respectively) using different *p*-CdTe (a) and evolution of the $F(V)$ function of diode D2 during refinement of the diffusion potential (b).

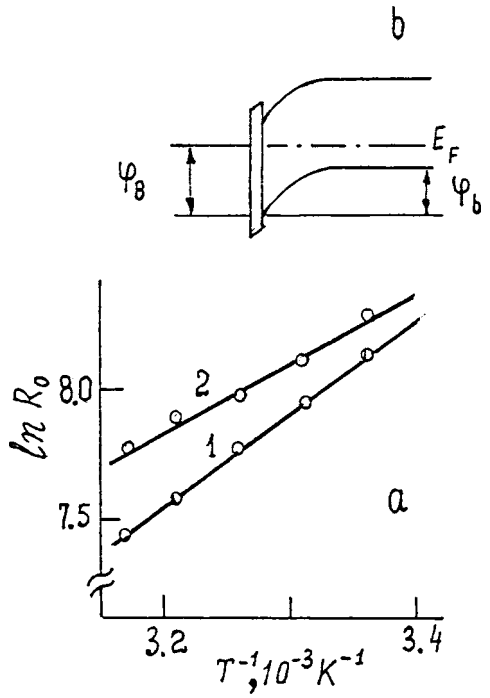

FIG. 2. Temperature dependences of the zero-bias differential resistance of diodes D1 and D2 (a) and energy model of Me–*p*–CdTe barrier (φ_b is the barrier height for *p*-CdTe holes and φ_B is that for metal holes) (b).

junction the saturation current density j_{SD} is given by[5]

$$j_{SD}=qp_\infty\mu_p\frac{V_D}{w}\exp\left(-\frac{\varphi_b}{kT}\right). \tag{2}$$

Here p_∞ is the hole concentration in the bulk of the *p*-CdTe, w is the width of the space charge region, and φ_b is the barrier height for the semiconductor holes[6] (Fig. 2b), which is related to the diffusion potential V_D by

$$\varphi_b=qV_D. \tag{3}$$

Applying a formalism similar to expression (1), we denote the factor before the exponential function in formula (2) by A_D such that

$$A_D=qp_\infty\mu_p\frac{V_D}{w}. \tag{4}$$

The Norde function (1) can then be modified to the case of a current diffusion mechanism which gives

$$F(V)=\frac{V}{2}-\frac{kT}{q}\ln\frac{I}{AA_D}. \tag{5}$$

By plotting the results of measuring the I–V characteristics of structures having a current diffusion mechanism in the form (5), we can determine the barrier height φ_b on the semiconductor side, unlike expression (1), and then use this to determine the barrier height on the metal side φ_B (Ref. 6) (Fig. 2b). However, some difficulties are encountered along the way because φ_b appears directly in Eqs. (4) and (5). This can be avoided by using the approximation $V_D=V_I$ to determine V_D in Eq. (4). Here V_I is the current cutoff voltage on the forward part of the current–voltage characteristic plotted in the coordinates I, V. Since A_D appears in the denominator of the logarithm in Eq. (5), using this approximation only gives an error of the second order of smallness when determining φ_b from the $F(V)$ curve.

TABLE I. Comparison between the parameters of Sn–*p*-CdTe Schottky diodes obtained by analyzing the experimental current–voltage characteristics*, $F(V)$**, and the temperature dependence of the differential resistance R_0***.

Diodes	V_I*, V	φ_b**, eV	$\varphi_{b,R}$***, eV	r*, Ω	r**, Ω
D1	0.19	0.31		210	400
D2	0.18	0.25	0.265	200	560
		0.26[a]			
D3	0.10	0.25	0.24	3×10^3	3.2×10^3

[a]Refined value of φ_b obtained by repeated plotting of $F(V)$.

We checked the efficiency of using the proposed modification of the function $F(V)$ (5) to determine the parameters of Me(In,Sn)–*p*-CdTe diodes. The $F(V)$ dependences constructed using the experimental current–voltage characteristics of these diodes are plotted in Fig. 1a (curves *1* and *2*). In this case, the numerical values of p_∞ and w for substitution into Eq. (4) were determined from measurements of the differential capacitance of the barriers and its dependence on the bias voltage and V_I was taken to be equal to the current cutoff V_D of the current–voltage characteristic. It can be seen that a typical minimum for the $F(V)$ function is observed for curves *1* and *2*. As in Ref. 1, we used the coordinates of this minimum to determine the barrier height φ_b and the base resistance r, which are given in Table I. It can be seen that there is a substantial difference between the numerical values of φ_b and V_I. In order to determine φ_b more accurately, we again constructed the $F(V)$ dependence for diode D2 using the previously determined value $\varphi_b=0.25$ eV (Fig. 1b, curves *2* and *2′*). We then obtained $\varphi_b=0.26$ eV, which only differs by 0.01 eV from the result obtained using the approximation $V_D=V_I$.

The results obtained using the proposed technique were compared with results of measuring the temperature dependence of the differential resistance of the diode at zero bias (Fig. 2a) using the method from Ref. 7 (see Table I). It can be seen that the values of φ_b obtained independently by each method agree to within 0.01 eV. However, a significant difference is observed between the value of r and that estimated fairly approximately from the current–voltage characteristic. We postulate that one reason for this discrepancy is carrier injection in the Me–*p*-CdTe barriers which is manifest in the specific behavior of the differential capacitance and the current–voltage characteristic at positive bias $V\geqslant V_D$.

To sum up, a method of vapor-phase growth of semi-insulating CdTe single crystals developed by us has been used to fabricate Schottky barriers with a diffusion mechanism of current flow, which are potentially useful for developing high-efficiency semiconductor detectors for nuclear radiation.

[1] E. N. Arkad'eva, O. A. Matveev, Yu. V. Rud', and S. M. Ryvkin, Zh. Tekh. Fiz. **36**, 1146 (1966).
[2] N. V. Agrinskaya, Mater. Sci. Eng., B **16**, 172 (1993).

[3] G. Ilchuk, N. Ukrainets, B. Datsko, and V. Ukrainets, in *Abstracts of ICCG 12*, *ICVG 10*, Jerusalem, Israel, 1998, p. 311.
[4] H. Norde, J. Appl. Phys. **50**, 5052 (1979).
[5] E. H. Rhoderik, *Metal–Semiconductor Contacts* (Clarendon Press, Oxford, 1978; Radio i Svyaz', Moscow 1982, 208 pp.).
[6] J. I. Pankove, *Optical Processes in Semiconductors* (Prentice-Hall, Englewood Cliffs, N.J., 1971; Nauka, Moscow, 1973, 456 pp.).
[7] V. I. Panichevskaya and V. I. Strikha, Radiotekh. Elektron. **20**, 1559 (1975).

Translated by R. M. Durham

Anomalous backscattering of high-power laser radiation by the flat surface of a solid

A. Yu. Ivanov

Institute of Analytical Instrumentation, Russian Academy of Sciences, St. Petersburg
(Submitted March 26, 1999)
Pis'ma Zh. Tekh. Fiz. **25**, 29–38 (August 26, 1999)

Results of measurements of the backscattering characteristics of high-power laser radiation at flat randomly rough surfaces of various materials are described for a wide range of radiation and surface parameters. It is observed that for probe radiation intensities in the range $\sim 10^3$–10^7 W/cm^2 and a pulse duration of $\sim 10^{-8}$ s the scattering pattern becomes anomalous under various additional conditions. The results are analyzed in accordance with the laws of structural conditionality, the qualitative boundary, abnormality, and alternation of nonequilibrium. Possible practical applications of the observed effect are discussed. © *1999 American Institute of Physics.* [S1063-7850(99)02008-X]

Studies of the interaction of high-power laser radiation with the surface of solids have recently become increasingly relevant. It is important to determine the properties of surfaces for strain measurements, monitoring surface roughness during the treatment of materials, quality control in laser optics (such as cavity mirrors, crystals, dispersion elements, and so on), in nonlinear optics, lidar, microinterferometry, ellipsometry, and so on.

In order to study the characteristics of light scattering by plane, isotropic, treated rough surfaces of various materials, Besnichenko *et al.* developed a universal experimental rig[1,2] which could be used to make high-precision on-line measurements of a vast range of radiation backscattering characteristics over an extremely wide dynamic range.

This facility was used to make numerous measurements of the amplitude, polarization, temporal, and spectral scattering characteristics of samples. The measurements were made using various radiation sources, both coherent and incoherent, cw and pulsed (with short pulse durations of $\sim 10^{-8}$ s and a long inverse duty cycle of $\sim 10^6$), for various polarization states of the incident wave, at various wavelengths, for various sizes and orientations of the illuminated area, and at intensities of $\sim 10^{-3}$–10^9 W/cm^2, which corresponds to a radiation power of $\sim 10^{-3}$–10^6 W. The surface being studied was irradiated by a narrow, parallel light beam with low angular divergence of $\sim 10^{-3}$ rad. The scattered radiation was also detected in a small solid angle of $\sim 10^{-4}$ rad. The scattering angle was varied by rotating the sample, i.e., the scattering angle was equal to the angle of incidence and the angle between the directions of irradiation and observation was fixed at $\sim 2.5°$.

Angular dependences of the brightness coefficient $\beta(\varphi)$ and the reflection $\rho(\varphi)$ and the elements of the 2×2 rank Müller $[B_{ik}]$ polarization matrix of the sample surface were recorded, as well as the angular dependence of the scattered pulse duration $\tau(\varphi)$. A wide variety of materials having different structures was investigated, including metals and nonmetals, with various coatings and different depths of penetration of the radiation in the medium, over the roughness range $R_z 10^{-3}$–10^2 μm and the spectral range λ 0.26–1.1 μm.

It was found that the backscattering characteristics for intensities between 10^{-3} and 10^3 W/cm^2 and roughness between 10^{-3} and 10^2 μm in the cw and pulsed irradiation regimes give the well-known pattern with diffuse, specular, and specular diffuse scattering indicatrices which are described quite satisfactorily by the classical Fresnel and Rayleigh–Rice scattering theories.[3,4]

In the intensity range 10^7–10^{10} W/cm^2 the interaction between the radiation and the solid surface exhibits clearly defined nonlinear behavior. Processes are excited which generally lead to irreversible thermal deformations of the surface, such as optical breakdown, local breakdown at microinhomogeneities in the surface structure, thermodynamic deformations of the surface, melting and evaporation, cutting, polishing, and so on. The scattering characteristics naturally vary, compared with the previous case. These processes are also fairly well described using well-known theories of nonlinear optics.[5–7]

At some surfaces of specific materials, incoherent and nonlinear processes may take place, involving the emission of surface bulk particles (such as fluorescence, Raman scattering, harmonic generation and parametric frequency conversion, photoionization, various types of photochemical and optoacoustic processes, and so on). These processes may also lead to changes in the light scattering characteristics compared with the classical case and are also fairly accurately described using well-known optical theories.[8–10] However, these processes generally exhibit clearly defined resonant behavior and only take place for strictly specific materials.

At the same time, when coherent sources of radiation (lasers) are used, having short pulse durations of $\sim 10^{-8}$ s comparable with the characteristic structural times of atomic-molecular processes, and intensities of $\sim 10^3$–10^7 W/cm^2, i.e., when the degree of nonequilibrium[11] of the ''radiation–surface'' system is increased, an unusual scattering pattern appears. The backscattering indicatrices are elongated in the direction of specular reflection (Fig. 1) and the scattered pulse duration (which is increased up to a maximum of ten times greater than the duration of the incident radiation) exhibits characteristic dependences on the scattering angle,

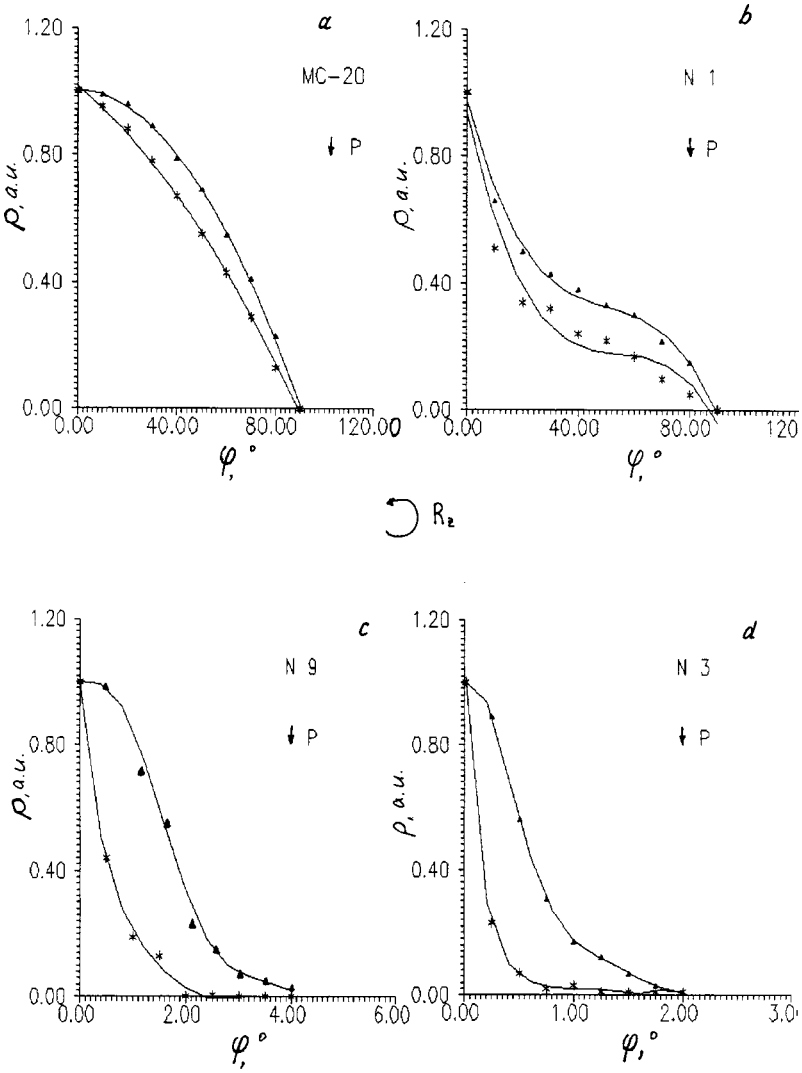

FIG. 1.

with a maximum at $\sim 45°$ whose value is inversely proportional to R_z (Fig. 2). In addition, the spectral dependences $\beta(\varphi)$, $\rho(\varphi)$, and $[B_{ik}](\varphi)$ change to the exact opposite ($\rho \sim \lambda^2$) of the classical case ($\rho \sim \lambda^{-2}$) (Fig. 3). These characteristics are inversely proportional to the average roughness R_z and increase with incident radiation power P_0 as follows: the angular width of the indicatrix increases as $\Delta\varphi \sim P_0^{-1/2}$ (Fig. 4) while the scattered pulse duration increases as $\tau_0 \sim P_0^{+1/2}$, and this increase may be two orders of magnitude.

Figures 1–4 give experimental data for typical specular (samples Nos. 3 and 9), specular-diffuse (sample No. 1) and diffuse samples (milky glass MS-20). The arrows indicate the directions of growth of the average surface roughness of the sample R_z and the pulse power of the incident laser radiation P_0. The integral expressions

$$\frac{\left(\int\int \rho(\varphi)d\varphi dt\right)^{P>10^3\ \mathrm{W}}}{\left(\int\int \rho(\varphi)d\varphi dt\right)^{P<10^3\ \mathrm{W}}} \cong \frac{(\Delta\varphi\Delta\tau)^{P>}}{(\Delta\varphi\Delta\tau)^{P<}} \cong \frac{(\Delta\varphi\rho(0))^{P>}}{(\Delta\varphi\rho(0))^{P<}} \cong 1 \qquad (1)$$

proved to be invariant relative to any change in the parameters of the incident radiation and the surface. This was confirmed by an additional experiment to measure the integral absolute reflection coefficients of the surfaces, which are defined as

$$\rho_0 = \int_0^\infty dt \int_0^\pi \rho(\varphi)d\varphi. \qquad (2)$$

The results suggest that as the degree of nonequilibrium of the ''incident radiation–surface'' system increases, specifically as the incident radiation intensity increases and the pulse duration decreases, i.e., as these values approach some structural critical constants ($\tau_0 \to \tau_s^c$, $P_0 \to P_0^c$), the space–time characteristics of the radiation scattered by the flat, isotropic rough surface of the solid change substantially. The total energy of the scattered radiation beam does not change. Energy is merely transferred from the diffuse to the specular component of the scattered radiation, and this process takes place with some time delay which depends first, on the angle of incidence and the direction of polarization of the incident wave, the wavelength and intensity of the incident laser radiation, and second on the characteristics of the irradiated surface. This process is elastic, reversible, and does not de-

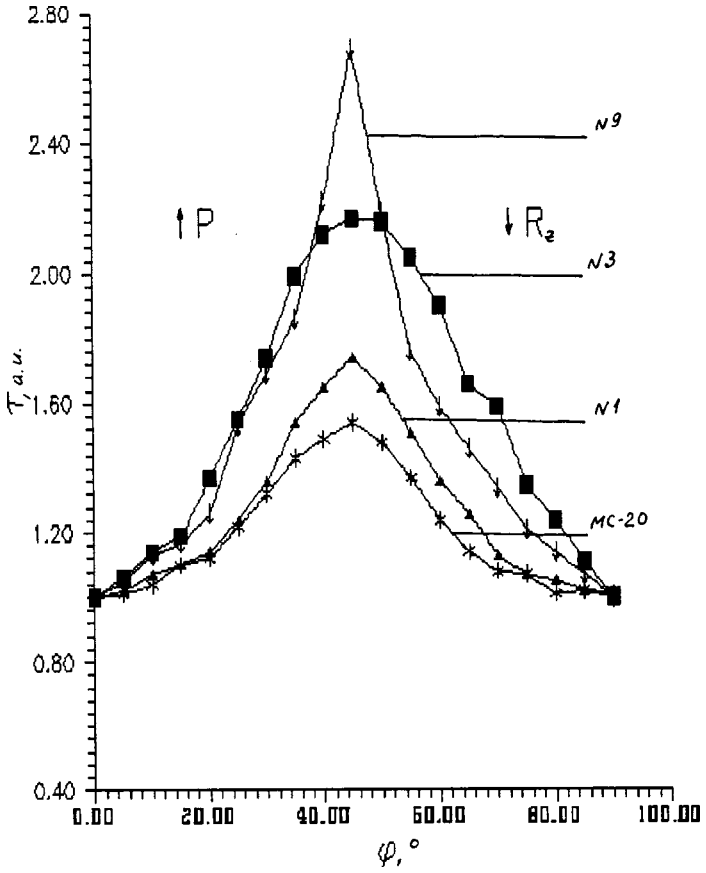

FIG. 2.

pend on the size and orientation of the irradiated part of the surface. Moreover, no nonlinear and incoherent processes take place at the surface, typical of high laser radiation intensities $I \sim 10^7 - 10^{10}$ W/cm^2. However, this anomalous scattering pattern cannot be explained in terms of the classical Fresnel and Rayleigh–Rice scattering theories, which work well for intensities $I < 10^3$ W/cm^2.

Thus, some window effect is observed for which beyond some qualitative boundary $\lambda \to \lambda_s$ ($R_z/\lambda \to \lambda/10$) (Ref. 11), $\tau_0 \to \tau_s \sim 10^{-8}$ s (Ref. 12), and $\varepsilon_0 \to \varepsilon_s$ ($I_0 \to I_c = 10^3 - 10^7$ W/cm^2), the surface scattering of laser radiation becomes anomalous. This is consistent with the laws of qualitative boundary, abnormality, and alternation of nonequilibrium.[11,12] The most reasonable physical explanation of the observed effect can be put forward in terms of the theory of three-wave interaction of the scattered wave with the incident wave and a wave initiated by this incident wave, known as a surface electromagnetic wave, during the dynamic reversible structural rearrangement of the surface under the action of high-power laser radiation,[13–16] which is consistent with the law of structural conditionality.[17]

Following this theory, the lower quality boundaries ε_s and τ_s may be determined from the condition of optimum reversible dynamic structural rearrangement of the surface under the action of high-power pulsed laser radiation, and maximum amplitude of the accompanying surface electromagnetic wave. These can be determined from:[18]

$$\begin{cases} kI_0\tau_0 \geqslant (R_z/\lambda)\text{opt} \\ I_0/I_c = 64\pi^2(w_{sp}/\gamma)(h/c\lambda)^2(1-\sin\varphi_{\text{opt}}) \geqslant 1, \end{cases} \tag{3}$$

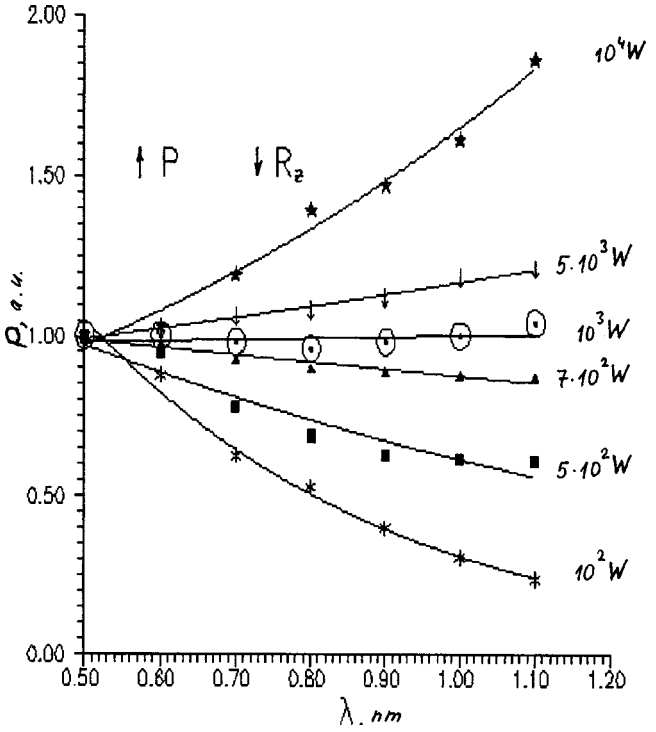

FIG. 3.

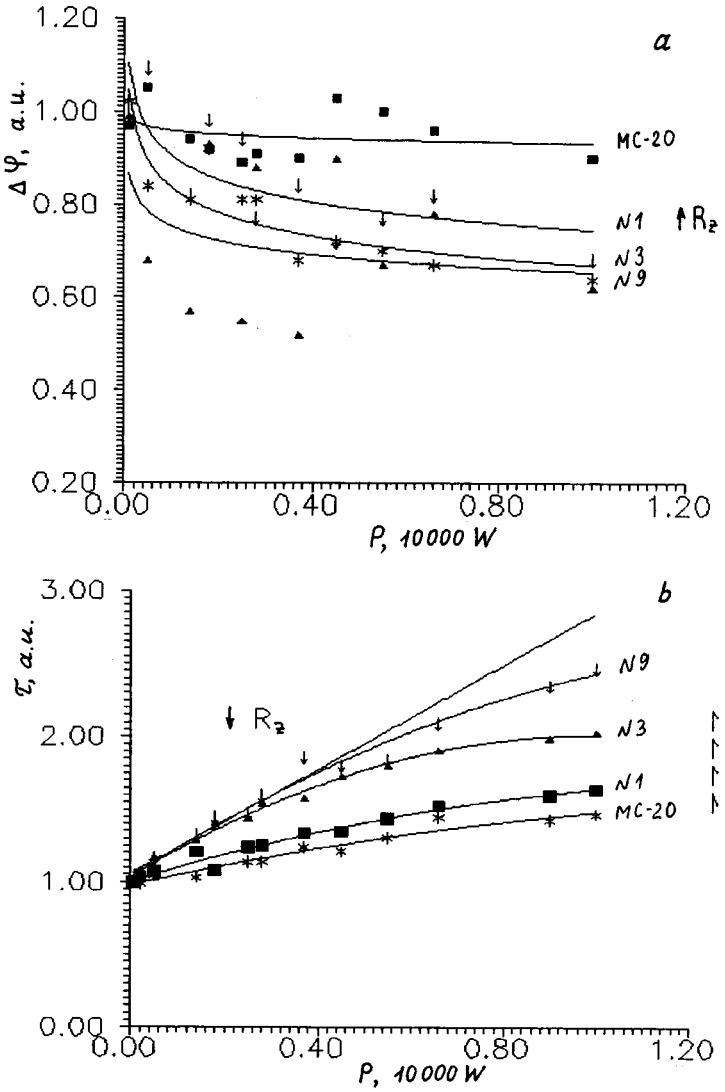

FIG. 4.

where $k \approx 1$ is a dimensional constant, w_{sp} and γ are the frequency and half-width of the excited surface-plasmon resonances, h and c are Planck's constant and the velocity of light in vacuum.

The upper quality boundary for the intensity is determined by the constraint to eliminate any nonlinear processes which lead to irreversible changes in the surface such as optical breakdown, and so on (see above).

Quite clearly, this anomalous scattering effect must be taken into account in many different cases: lidar, surface quality control during treatment of materials, quality control in laser optics, nonlinear optics, spectroscopy, in the theory of interaction between light and matter, and so on. This effect may serve as the basis for developing new efficient technologies using the ''window of quasiequilibrium.'' These include laser optics where this effect means that mirrors whose surface quality is considerably inferior to that required for Fresnel reflection may be used. With this in mind, the author was able to fabricate a high-power solid-state laser using a nontransmitting ''poor-quality'' mirror and an interference pile, made of plane-parallel glass plates, as the exit mirror.[19]

[1] G. A. Vesnicheva, A. Yu. Ivanov, and G. M. Malyshev, Deposited Paper No. 4215-B, dated 17.05.1988, TsNIITÉIpriborostroeniya (1988), 10 pp.
[2] G. A. Vesnicheva, A. Yu. Ivanov, and V. M. Prosuzhikh, in *Abstracts of Papers presented at Second International Conference on Optical Processing of Information*, Frunze, 1990 [in Russian], pp. 153–154.
[3] V. A. Kizel', *Reflection of Light* [in Russian], Nauka, Moscow (1973), 502 pp.
[4] V. V. Maksimenko, V. I. Krikunov, and A. A. Lushnikov, Zh. Éksp. Teor. Fiz. **102**, 1571 (1992) [Sov. Phys. JETP **75**, 848 (1992)].
[5] S. I. Anisimov, Ya. A. Imas, T. S. Romanov, and Yu. V. Khadyko, *Action of High-Power Radiation on Metals* [in Russian], Nauka, Moscow (1970), 272 pp.
[6] A. S. Kovalev, A. M. Popov, and O. B. Pyatigorskaya, Zh. Tekh. Fiz. **53**, 939 (1983) [Sov. Tech. Phys. Lett. **28**, 603 (1983)].
[7] A. M. Bonch-Bruevich, Ya. A. Imas, M. N. Libenson, and G. D. Shandybina, Poverkhnost' No. 5, 102 (1985).
[8] A. M. Bonch-Bruevich, Ya. A. Imas, M. N. Libenson, and G. D. Shandybina, Izv. Akad. Nauk SSSR Ser. Fiz. **49**, 1166 (1985).
[9] V. S. Letokhov, *Nonlinear Selective Photoprocesses in Atoms and Molecules* [in Russian], Nauka, Moscow (1988), 408 pp.
[10] A. M. Bonch-Bruevich, I. A. Didenko, and L. N. Kaporskiĭ, Izv. Akad. Nauk SSSR, Ser. Fiz. **49**, 1096 (1985).
[11] G. E. Skvortsov, Pis'ma Zh. Tekh. Fiz. **16**(17), 15 (1990) [Sov. Tech. Phys. Lett. **16**, 647 (1990)].
[12] G. E. Skvortsov, Pis'ma Zh. Tekh. Fiz. **23**(7), 23 (1997); **23**(6), 85 (1997) [Tech. Phys. Lett. **23**, 261 (1997); **23**, 247 (1997)].

[13] A. V. Andreev, V. I. Emel'yanov, and Yu. A. Il'inskiĭ, *Cooperative Effects in Optics* [in Russian], Nauka, Moscow (1988), 288 pp.
[14] P. Sheng, *Scattering of Classical Waves in Random Media* (World Scientific, Singapore, 1990), 417 pp.
[15] V. V. Kosobukin, Izv. Akad. Nauk SSSR Ser. Fiz. **49**, 1111 (1985).
[16] A. A. Maradudin and A. R. McGurn, J. Opt. Soc. Am. B **4**, 910 (1987).
[17] G. E. Skvortsov, Pis'ma Zh. Tekh. Fiz. **23**(10), 17 (1997) [Tech. Phys. Lett **23**, 383 (1997)].
[18] V. I. Emel'yanov, in *Abstracts of Papers presented at Seventh All-Union Conference on Interaction of Optical Radiation with Matter*, Leningrad, 1988 [in Russian], pp. 17–19.
[19] A. Yu. Ivanov, in *Abstracts of Papers presented at First International Conference on the ''Search, Study, and Development of Inventions in Russia,''*, St. Petersburg, 1992 [in Russian], pp. 49–50.

Translated by R. M. Durham

Possibility of nonequilibrium phase transitions in semiconductors and semiconducting superstructures in crossed electric and magnetic fields

E. P. Prokop'ev

A. Yu. Malinin Research Institute of Materials Science, Moscow
(Submitted December 11, 1998)
Pis'ma Zh. Tekh. Fiz. **25**, 39–44 (August 26, 1999)

An analysis is made of two types of negative differential conductivity in semiconductors and semiconducting superstructures containing *ND* shallow impurity atomic systems (centers), in crossed electric and magnetic fields corresponding to nonequilibrium phase transitions of n_e, where n_e is the average density of nonequilibrium carriers (electrons). It is observed that these semiconductors and semiconducting superstructures in crossed electric and magnetic fields may be used to fabricate various semiconductor devices and apparatus, and also memory elements for the acquisition, storage, and protection of information under extreme conditions. © *1999 American Institute of Physics.* [S1063-7850(99)02108-4]

The concept of fabricating various semiconductor devices and apparatus, and memory elements by modifying the properties of natural systems such as normal atoms and shallow impurity atomic systems (centers) created by doping, or artificial atomic systems, such as excitons and superatoms, in semiconductors and semiconducting superstructures in crossed electric and magnetic fields is now quite clearly a realistic proposition.[1–7] At this point, it should be noted that the electronic properties of ordinary atoms are predetermined by nature, while the electronic properties of superatomic systems can be determined artificially.

In principle, atomic systems (such as shallow electronic impurity centers) of different dimensions, including one-dimensional (1*D*), two-dimensional (2*D*), and three-dimensional (3*D*), can be formed in semiconductors and semiconducting structures using crossed electric and magnetic fields.[4] Using the effective mass approximation, the energies of the ground state of these atomic systems are given by

$$E(3D) = -\frac{Z^2}{2n^2}\frac{m_n e^4}{\varepsilon^2 h^2}, \tag{1}$$

where $Z=1$ is the effective charge of the atomic impurity system, m_n is the effective electron mass, e is the electron charge, ε is the static permittivity, and h is Planck's constant. For the ground state, the principal quantum number is $n=1$.

For a two-dimensional impurity atomic system we have

$$E(2D) = -\frac{Z^2}{2(n-1/2)^2}\frac{m_n e^4}{\varepsilon^2 n^2}, \quad n = 0,1,2,\ldots \tag{2}$$

For the ground state the principal quantum number is $n=0$.

For the ground state of a one-dimensional impurity atomic system we have

$$E(1D) = -\frac{h^2}{2m_n a^2 \alpha^2} = -\frac{1}{2\alpha^2}\frac{m_n e^4}{\varepsilon^2 h^2}, \tag{3}$$

where

$$a = \frac{h^2 \varepsilon}{m_n e^2}. \tag{4}$$

Here $\alpha \ll 1$ is the parameter from the theory of a one-dimensional hydrogen atom.[5]

From Eqs. (1) and (2), the binding energies $W(3D) = -E(3D)$ and $W(2D) = -E(2D)$ for the ground state are related as[6,7]

$$W(2D) = 4W(3D), \tag{5}$$

and $W(1D) = -E(1D)$ is given in accordance with Ref. 5

$$W(!D) \gg W(2D), \quad W(1D) \gg E(3D). \tag{6}$$

Apart from anomalies (5) and (6) in the binding energies, two-dimensional and one-dimensional atomic systems have anomalous properties in relation to the action of electric (Stark effect) and magnetic fields (Zeemann effect).[5–7] We shall not discuss these effects here, but will focus our attention on transitions of the type

$$W(3D) \leftrightarrow W(2D) \leftrightarrow W(1D), \tag{7}$$

$$W(3D) \leftrightarrow W(2D); \quad W(2D) \leftrightarrow W(1D) \tag{8}$$

in crossed electric and very strong (up to ~ 100 T) magnetic fields.[4]

It is readily established that transitions of the type (7) and (8) in the bulk conductivity of a semiconductor and a semiconducting superstructure correspond to the different cases of negative differential conductivity,[8] shown for transitions of type (7) (Fig. 1, curve *1*) and type (8) (curve *2*). Figure 2 gives a diagram of the process and an example of a device, for a GaAs bulk semiconductor and a gallium arsenide quantum well in an $Al_{0.3}Ga_{0.7}As \mid GaAs$ semiconducting superstructure with applied crossed electric E and magnetic H fields.

We shall assume that in general, the bulk of the GaAs semiconductor and the gallium arsenide quantum well of the $Al_{0.3}Ga_{0.7}As|GaAs$ semiconducting superstructure contain

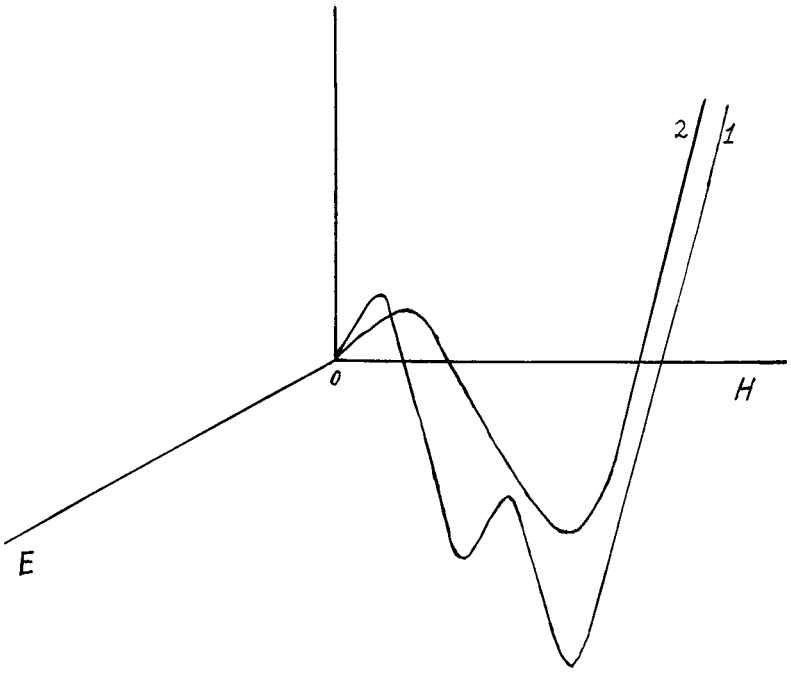

FIG. 1. Dependence of the current density j on crossed electric E and magnetic H fields for two types of negative differential conductivity: *1* — for a transition of type (7), *2* — for a transition of type (8).

3*D*, 2*D*, and 1*D* shallow impurity states, respectively. When crossed electric E and magnetic H fields are applied, transitions of type (7) and (8) will be observed, shallow *ND* impurities will undergo electron impact ionization, and recombination will take place when an electron encounters an ionized impurity.

Following Ref. 9, these processes correspond to the scheme

$$n_e+n_a \underset{\beta}{\overset{\alpha}{\leftrightarrow}} n_i+2n_e; \quad n_e+n_a=n; \quad n_e=n_i, \tag{9}$$

where n_e, n_i, and n_a are the average densities of electrons, ionized impurities, and neutral atoms, respectively, and α and β are the coefficients of electron impact ionization of shallow impurities and recombination of electrons and ionized impurities in the presence of an electron.

The dynamic generation–recombination equations[8,9] corresponding to the scheme (9) have the form

$$\frac{dn_e}{dt}=\alpha n_e n_a-\beta n_e^2 n_i=(\alpha n_a-\beta n_e n_i)n_e;$$

$$n_e=n_i; \quad n_e+n_a=n. \tag{10}$$

Here the second equation in the system (10) assumes that the average numbers of electrons and ionized impurities are equal, and the third assumes that the number of electrons and neutral impurity centers is constant.

It is easy to establish that Eq. (10) can be reduced to the form

$$\frac{dn_e}{dt}[\alpha(n-n_e)-\beta n_e^2]n_e=(r_{n_e}-g_{n_e})n_e, \tag{11}$$

where $r_{n_e}=\alpha(n-n_e)$ and $g_{n_e}=\beta n_e^2$ are the rate constants for impact ionization and carrier recombination.

Note that in general in the presence of the fields E and H, the rate constants r_{n_e} and g_{n_e} should be functions of the strengths of these fields, i.e.,

$$r_{n_e}=r_{n_e}(E,H); \quad g_{n_e}(E,H), \tag{12}$$

where the coefficients of impact ionization α and recombination β also depend on E and H, as is deduced from the above reasoning.

For instance, in accordance with Refs. 10 and 11, the coefficient of impact ionization is given by the Shockley formula

$$\alpha(E,H)=[eE/\varepsilon_i(H)]\exp[-\varepsilon_i(H)/eE\lambda], \tag{13}$$

where λ is the mean free path and $W_i=\varepsilon_i$ is the threshold value of the ionization energy which generally increases with increasing H. For simplicity, we shall neglect the dependence of β on the fields E and H, so that

$$\alpha=\alpha(E,H); \quad \beta=\beta(n_e). \tag{14}$$

Equation (11) then becomes

$$\frac{dn_e}{dt}[r_{n_e}(E,H)-g_{n_e}]n_e. \tag{15}$$

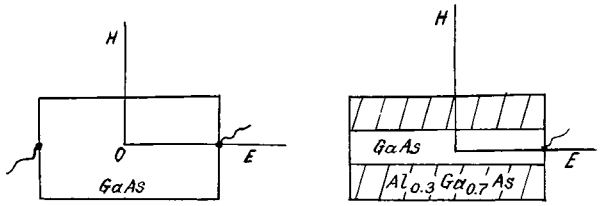

FIG. 2. Diagram of process and device using a GaAs semiconductor (*1*) and an $Al_{0.3}Ga_{0.7}As|GaAs$ semiconducting superstructure (*2*) in crossed electric E and magnetic H fields.

We can see from Eq. (15) that

$$\text{for} \quad r_{n_e}(E,H) < g_{n_e}; \quad n_e(\infty) \to 0, \tag{16}$$

$$\text{for} \quad r_{n_e}(E,H) > g_{n_e}; \quad n_e(\infty) \neq 0. \tag{17}$$

Thus, it follows from Eqs. (11)–(13) that as E and H increase, we have cases of nonequilibrium phase transitions from state (17) to state (16) and back in a range of specific values of $\alpha(E,H)$ [since $W = W(H)$] and this is responsible for the different types of negative differential conductivity. These transitions can be studied in detail using methods from the physics of open systems described in Ref. 10.

Transitions of the type (16) and (17) can also be observed for ordinary natural atoms in ultrastrong magnetic fields ($H \approx 10^9$ T) at the surface of neutron stars.[12]

In conclusion, it should be noted that transitions of the type (7) and (8) corresponding to the negative differential conductivity in Fig. 1, may be used to fabricate various semiconducting devices and apparatus (such as tunnel diodes, Gunn diodes, and so on[8]), and also memory elements for the acquisition, storage, and protection of information under extreme conditions.[13]

The author would like to thank Yu. V. Kopaev and A. A. Gorbatsevich for discussions and valuable comments.

[1] A. Watanabe and T. Inoshita, Optoelectron., Devices Technol. **1**(1), 33 (1986).
[2] T. Inoshita, S. Ohnishi, and A. Oshiyama, Phys. Rev. Lett. **57**, 2360 (1980).
[3] E. A. Andryushin and A. P. Silin, Fiz. Tverd. Tela (Leningrad) **33**, 211 (1991) [Sov. Phys. Solid State **33**, 123 (1991)].
[4] L. A. Burkova, I. E. Dzyaloshinskiĭ, G. F. Drukarev, and V. S. Monozon, Zh. Éksp. Teor. Fiz. **71**, 526 (1976) [Sov. Phys. JETP **44**, 276 (1991)].
[5] R. Loudon, Am. J. Phys. **27**, 649 (1959).
[6] X. L. Yang, S. H. Guo, F. T. Chang *et al.*, Phys. Rev. A **43**, 1186 (1991).
[7] H. A. Bethe and E. E. Saltpeter, *Quantum Mechanics of One- and Two-Electron Atoms* (Academic Press, New York, 1957; Fizmatgiz, Moscow, 1961, 564 pp.).
[8] E. Schöll, *Nonequilibrium Phase Transitions in Semiconductors : Self-Organization Induced by Generation and Recombination Processes* (Springer-Verlag, New York, 1987; Nauka, Moscow, 1991), 460 pp.
[9] Yu. L. Klimontovich, Usp. Fiz. Nauk **164**, 811 (1994); **166**, 1231 (1996)].
[10] L. P. Landsberg and A. Pimpale, J. Phys. C: Solid State Phys. **9**, 1243 (1976).
[11] W. Shockley, Solid-State Electron. **2**, 95 (1961).
[12] M. A. Liberman and B. Johansson, Usp. Fiz. Nauk **165**(2), 121 (1995).
[13] E. P. Prokop'ev, Deposited Paper No. R-4497 [in Russian], TsNII ''Élektronika,'' Moscow (1993), p. 179.

Translated by R. M. Durham

Zero-radius potential model for a planar waveguide in a photonic crystal

I. Yu. Popov

Institute of Precision Mechanics and Optics, St. Petersburg
(Submitted February 9, 1999)
Pis'ma Zh. Tekh. Fiz. **25**, 45–49 (August 26, 1999)

A zero-radius potential model is proposed to describe a waveguide in a planar crystal. Two-dimensional and three-dimensional cases are considered. Layers, waveguides, and coupled waveguides are described. Explicit model dispersion equations are derived and the spectral properties are described. © *1999 American Institute of Physics.* [S1063-7850(99)02208-9]

The development of nanotechnology has now reached the stage where it is possible to fabricate materials impregnated with periodically distributed small inclusions, for instance, in the form of small spherical particles or thin parallel filaments. Typical sizes are inclusions of around 100 nm diameter, where the particles occupy no more than 0.1 of the volume. This has made it possible to fabricate new optical materials, i.e., photonic crystals (see, for example, Ref. 1) which have extremely promising applications, especially in fiber optics. However, the theoretical description of these systems has not yet been sufficiently developed, so there is an urgent need to develop suitable theoretical methods.[2–4] In the present study we propose to use a method of zero-radius potentials, based on the theory of self-conjugate expansions of symmetric operators,[5,6] to describe various waveguide systems in photonic crystals (see Figs. 1a–1e).

We shall consider a photonic crystal in the form of a three-dimensional cubic lattice and we shall assume that the sizes of the inclusions are small compared with the wavelength. The model assumes that these inclusions are replaced by zero-radius potentials and that one layer of centers is missing from the lattice. We then have a waveguide layer. If the polarization is fixed (for example, TM) and we assume a harmonic time dependence, we can reduce the problem to the Helmholtz equation. In order to construct the model, we shall first make a separate analysis of the three-dimensional lattice and the monomolecular layer. We shall assume that Λ is a Bravais lattice with the basis a_1, a_2, a_3 and Γ is a reciprocal lattice with the basis b_1, b_2, b_3. We shall consider the closure of the Laplace operator in $L_2(\mathbf{R}^3)$ contracted to a set of functions which go to zero at the lattice points. This is a symmetric nonself-conjugate operator. ''Switching on'' the zero-radius interaction means constructing its self-conjugate expansion. Taking into account the periodicity, we construct the model operator Δ_Λ (Ref. 5) whose spectrum is absolutely continuous and has the form:

$$\sigma(-\Delta_\Lambda)=\sigma_{ac}(-\Delta_\Lambda)[E_0^\Lambda(0),E_0^\Lambda(\theta_0)]\cup[E_1^\Lambda,\infty], \quad (1)$$

where

$$\theta_0=-\frac{1}{2}(b_1+b_2+b_3),$$

$$E_1^\Lambda=\min\left\{E_{b_-}^\Lambda(0),\frac{1}{4}|b_-|^2\right\}.$$

Here $b_-, b_-\in\{b_1,b_2,b_3\}$ is such that $|b_-|\leqslant|b_j|$, $j=1,2,3$. $E_0^\Lambda(0)$ is the first root of the equation

$$\alpha=(2\pi)^{-3}\lim_{\omega\to\infty}\left[\sum_{\gamma\in\Gamma,|\gamma+\theta|\leqslant\omega}\frac{|\hat\Lambda|}{|\gamma+\theta|^2-k^2}-4\pi\omega\right],$$

$$\theta\in\hat\Lambda, \quad (2)$$

where $\hat\Lambda=\{s_1b_1+s_2b_2+s_3b_3\in\mathbf{R}^3,$

$s_j\in[-1/2,1/2), \quad j=1,2,3\}$,

$\hat\Lambda$ is the Brillouin zone, θ is the quasimomentum, and α is a model parameter related to the potential ''force.''

A similar analysis is performed for the monomolecular layer.[5,7] As a result, we obtain the model operator Δ_{Λ_2} having the following spectrum:

$$\sigma(-\Delta_{\Lambda_2})=\sigma_{ac}(-\Delta_{\Lambda_2})=\begin{cases}[E_0^{\Lambda_2}(0),\infty), & \alpha\geqslant\alpha_{\Lambda_2},\\ [E_0^{\Lambda_2}(0),E_0^{\Lambda_2}(\theta_0)]\cup[0,\infty), & \alpha<\alpha_{\Lambda_2},\end{cases} \quad (3)$$

where $E_0^{\Lambda_2}(0)$, $E_0^{\Lambda_2}(\theta)=[k_0^{\Lambda_2}(\theta)]^2$ is the root of the equation

$$\alpha=(2\pi)^{-3}\pi\lim_{\omega\to\infty}\left[\sum_{\gamma\in\Gamma_2,|\gamma+\theta|\leqslant\omega}\frac{|\hat\Lambda_2|}{|\gamma+\theta|^2-k^2}-2\pi\omega\right],$$

$$\theta\in\hat\Lambda_2, \quad (4)$$

$$\mathcal{J}k_0^{\Lambda_2}(\theta)\geqslant0, \quad [k_0^{\Lambda_2}(\theta)]^2<|\theta|^2, \quad \theta_0=-(b_1+b_2)/2.$$

Moreover, we have $E_0^{\Lambda_2}(0)<E_0^{\Lambda_2}(\theta_0)<0$ for $\alpha<\alpha_{\Lambda_2}$,

$$\alpha_{\Lambda_2}=\frac{1}{8\pi^2}\lim_{\omega\to\infty}\left[\sum_{\gamma\in\Gamma_2,|\gamma+\theta_0|\leqslant\omega}\frac{|\hat\Lambda_2|}{|\gamma+\theta_0|^2}-2\pi\omega\right].$$

Exactly the same analysis is performed for a linear polymer. The spectrum of the corresponding model operator Δ_{Λ_1} is:

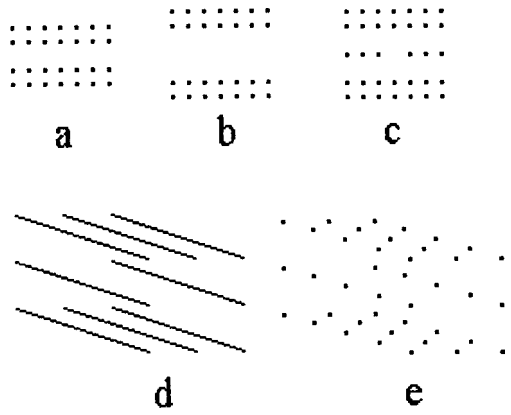

FIG. 1. Structures being studied: two-dimensional square lattice, with one line of unfilled sites (a), with three unfilled lines of sites (b), with two separated unfilled lines of sites (coupled waveguides) (c); three-dimensional lattice structure (waveguide), equivalent two-dimensional structure (lattice with one unfilled center) (d); three-dimensional lattice with unfilled line of sites (waveguide) (e).

$$\sigma(-\Delta_{\Lambda_1})=\sigma_{ac}(-\Delta_{\Lambda_1})=\begin{cases}[E_0^{\alpha,\Lambda_1},\infty), & \alpha\geqslant-(\ln 2)/2\pi\alpha,\\ [E_-^{\alpha,\Lambda_1},E_+^{\alpha,\Lambda_1}]\cup[0,\infty), & \alpha<-(\ln 2)/2\pi\alpha,\end{cases} \tag{5}$$

where

$$E_{\pm}^{\alpha,\Lambda_1}=-\alpha^{-2}\left\{\ln\left[\mp 1+\frac{1}{2}e^{-4\pi\alpha a}+e^{-2\pi\alpha a}\sqrt{\frac{1}{4}e^{\pi\alpha a}\mp 1}\,\right]\right\}^2. \tag{6}$$

We then use this scheme to construct a model of the conducting layer in a photonic crystal. It is easy to see that the lattice sum in the dispersion equation breaks down into the difference between the corresponding lattice sums for the total crystal and the monomolecular layer. Thus, taking into account Eqs. (2) and (4) we obtain the following dispersion equation:

$$\alpha=(2\pi)^{-3}\left(\lim_{\omega\to\infty}\left[\sum_{\gamma\in\Gamma,|\gamma+\theta|\leqslant\omega}\frac{|\hat{\Lambda}|}{|\gamma+\theta|^2-k^2}-4\pi\omega\right]-\pi\lim_{\omega\to\infty}\left[\sum_{\gamma\in\Gamma_2,|\gamma+\theta|\leqslant\omega}\frac{|\hat{\Lambda}_2|}{|\gamma+\theta|^2-k^2}-2\pi\omega\right]\right). \tag{7}$$

Bearing in mind the behavior of the functions on the right-hand side of the equation, we conclude that there are generally two zones (a ''crystal zone'' and a ''layer zone'') which cannot intersect. Their position depends on the relationships between $E_0^{\Lambda_2}(0)$, $E_0^{\Lambda_2}(\theta_0)$, $E_0^{\Lambda}(0)$, $E_0^{\Lambda}(\theta_0)$, and E_0^{Λ} [see Eqs. (1) and (3)]. The states corresponding to the layer zone describe the propagation of a photon along the layer, i.e., the waveguide effect.

Exactly the same analysis is made for the waveguide structure (see Fig. 1c) except that here the role of the second term is played by the lattice sum for the linear polymer, which leads to the appearance of a waveguide zone related to the corresponding zone (5).

The two-dimensional problems involved in describing structures consisting of parallel dielectric filaments are solved similarly. We merely need to replace the Green function for the three-dimensional space $\exp(ik|\gamma|)/(4\pi|\gamma|)$ by the Green function for the plane $\frac{i}{4}H_0^{(1)}(k|\gamma|)$. Note that if several ($n$) layers rather than one are missing (Fig. 1b), there are generally n waveguide zones, although they may overlap. This agrees with the result obtained in Ref. 8. A more complex structure consisting of coupled waveguides (Fig. 1c) may also be considered. In this case, in addition to the zone, a bound state appears which passes from the eigenvalue of the isolated zero-radius potential to the planes. This results agrees with the results[8] for a curved waveguide and agrees with Refs. 9 and 10 for coupled waveguides with nontransmitting walls.

This work was supported by the RFBR and by the International Science Foundation.

The authors thank P. Kuchment for useful discussions.

[1] J. D. Joannopoulos, R. D. Meade, and J. N. Winn, *Photonic Crystals* (Princeton University Press, Princeton, 1995), 312 pp.
[2] A. Figotin and P. Kuchment, SIAM (Soc. Ind. Appl. Math.) J. Appl. Math. **58**, 683 (1998).
[3] A. Moroz and A. Tip, Phys. Lett. A **235**, 195 (1997).
[4] J. -M. Combes, in *Abstracts of the International Conference ''Rigorous Results in Quantum Mechanics''*, Prague, Czech Republic, 1998, p. 3.
[5] S. Albeverio, F. Gesztesy, R. Hoegh-Krohn, and H. Holden, *Solvable Models in Quantum Mechanics* (Springer-Verlag, Berlin, 1988), 566 pp.
[6] B. S. Pavlov, Usp. Mat. Nauk **42**(6), 99 (1987).
[7] Yu. E. Karpeshina, Teor. Mat. Fiz. **57**, 414 (1983).
[8] A. Mekis, S. Fan, and J. D. Joannopoulos, Phys. Rev. B **58**, 4809 (1998).
[9] I. Yu. Popov, Rep. Math. Phys. **40**, 521 (1997).
[10] I. Yu. Popov, Pis'ma Zh. Tekh. Fiz. **25**(3), 57 (1999) [Tech. Phys. Lett. **25**, 106 (1999)].

Translated by R. M. Durham

Observation of a long-range action effect in ion-bombarded GaAs transistor structures

S. V. Obolenskiĭ, V. D. Skupov, and A. G. Fefelov

N. I. Lobachevskiĭ State University, Nizhniĭ Novgorod
(Submitted March 11, 1999)
Pis'ma Zh. Tekh. Fiz. **25**, 50–53 (August 26, 1999)

Changes in the carrier concentration and mobility in the active layers of Schottky-barrier field-effect transistors are observed when the structures are bombarded with argon ions on the nonworking side of the GaAs substrate.
[S1063-7850(99)02308-3]

Various aspects of the ''long-range action effect'' observed when solids are bombarded with ions are attracting continued interest. This is not only because, in many respects, the controversial aspects of the mechanism for this have now been resolved, but also because of the search for, and implementation of, specific methods of using this effect in practice to modify the structure-sensitive properties of materials or elements of functionally completed articles, both directly in the implanted zones and at distances considerably greater than the ranges of the implanted ions. Both these lines of study are important for microelectronics where ion implantation has become an integral part of the technology for fabricating modern devices, although its influence on their long-range interaction characteristics is not yet clear. The aim of the present study was to investigate how ion bombardment on the substrate side influences the parameters of the active layers of Schottky-barrier, field-effect transistors fabricated on epitaxial gallium arsenide.

Transistors having a gate length of 0.5 μm were formed by the chloride method on structures consisting of a semi-insulating AGChPKh-8(001) substrate 60 mm in diameter and 400 μm thick, a 1 μm undoped buffer layer, a 0.1 μm Si-doped buffer layer having an electron concentration of $3\times10^{17}\,\mathrm{cm}^{-3}$, and a 0.15 μm n^+-GaAs contact layer having a carrier concentration of $10^{19}\,\mathrm{cm}^{-3}$. The gate and Omhic contacts were vacuum-deposited layers of Au with a Ti sublayer and an Au–Ge eutectic, respectively.[1] The distance between the nearest contact areas of two neighboring transistors was 300 μm. The regions of the structure between the transistors were insulated by proton implantation with the energy being varied in the order 90, 60, 30 eV and the dose at all energies was $3.8\times10^{13}\,\mathrm{cm}^{-2}$. After the transistors had been fabricated, the structures were chemically and mechanically polished on the substrate side to a thickness of 100 μm. Then, half the surface of the wafers on the substrate side was shielded with a metal mask and the other half was bombarded with 90 eV argon ions at various doses and current densities. The temperature of the structures during bombardment did not exceed 310 ± 5 K. The changes in the transistor parameters after bombardment were determined from the current–voltage and capacitance–voltage characteristics under normal conditions and under additional illumination by visible light (incandescent lamp, $W=25$ W), and also by controlling the gate potential of the measured transistor from the contact areas of a neighboring one.

The long-range influence of bombardment on the parameters becomes appreciable at argon ion current densities higher than 0.5 $\mu\mathrm{A/cm}^2$ and doses $\Phi>5\times10^{15}\,\mathrm{cm}^{-2}$. This is observed as an increase in the electron mobility and the formation of a steeper distribution profile of the electron concentration over the thickness of the active layer near the interface with the buffer (Fig. 1). Under the additional illumination, the current–voltage characteristics of these transistors do not depend on whether the current in the channel is controlled by its own an external gate (Fig. 2). The controlled parameters remain stable when the irradiated structures are held under normal conditions for one month, or when annealed in air at 400 K for 1 h.

These results indicate that the impurity-defect composition of the active layers and protonated insulating regions are irreversibly altered when the structures are bombarded on the substrate side. The changes in the transistor parameters suggest that this alteration is predominantly caused by a drop in the concentration of electron scattering centers in the active layer which, for example, may be point defect complexes formed during epitaxy.[2] It is also caused by the partial annealing of the radiation damage responsible for the insulating properties of the protonated regions under the action of an elastic wave field.[3,4] The main sources of elastic waves are the thermal peaks in the ion stopping zone. However, as they

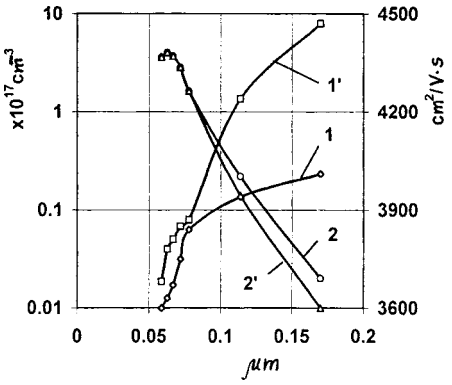

FIG. 1. Depth distribution profiles of the electron mobility (*1*, *1′*) and concentration (*2*, *2′*) before (*1*, *2*) and after (*1′*, *2′*) argon ion bombardment with the dose $\Phi=10^{16}\,\mathrm{cm}^{-2}$.

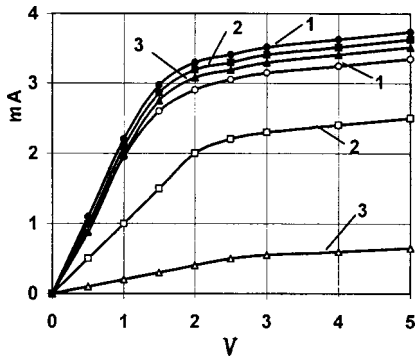

FIG. 2. Current–voltage characteristics of transistors illuminated and controlled from an external electrode (*1* — $V_c = 0$ V, *2* — $V_c = -0.4$ V, *3* — $V_c = -0.8$ V) before (filled symbols) and after (open symbols) argon ion bombardment with the dose $\Phi = 10^{16}\,\mathrm{cm}^{-2}$.

propagate through the entire thickness of the structure, the amplitude of these waves decreases substantially, and estimates made using the results of Ref. 3 show that for our case the pressure drops from $P_{\max} = 1.44$ GPa (near the thermal peak) to 0.34 MPa in the active layer of the transistors. The energy of these waves $E = 10^{-4}$ eV/at is insufficient to directly activate the dissociation of impurity-defect complexes. Thus, their main role is to excite metastable pileups of point defects which is accompanied by the annihilation of components of Frenkel pairs, the drift of these to extended sinks, and the generation of secondary elastic waves.[4,5] These processes are most intense near the outer surface and the internal interfaces between the epitaxial layers where the mechanical stress gradient is greatest, and consequently the concentration of vacancies and interstitial atoms spatially separated by the interface is increased. The incidence of elastic waves at such an interface stimulates the annihilation of unlike point defects and thus results in the formation of secondary waves whose amplitude is equal to the hydrostatic component of the self-field of the elastic stresses of the defects, which is one or two orders of magnitude higher than $P_{\max}$ (Ref. 6). Numerical estimates of the amplitude and energy of the elastic waves propagating through the active layer from the internal interface give values of 46 MPa and 1.3×10^{-2} eV/at, respectively, at the free surface of the structure. These waves can initiate surface sources of point defects[3,7] which activate the transformation of the impurity-defect composition of the layer and annealing of damage in the protonated regions.

[1] S. V. Obolenskiĭ and G. P. Pavlov, Fiz. Tekh. Poluprovodn. **29**, 413 (1995) [Semiconductors **29**, 211 (1995)].
[2] M. G. Mil'vidskiĭ and V. B. Osvenskiĭ, *Structural Defects in Epitaxial Layers of Semiconductors* [in Russian], Metallurgiya, Moscow (1985), 160 pp.
[3] P. V. Pavlov, Yu. A. Semin, V. D. Skupov, and D. I. Tetel'baum, Fiz. Tekh. Poluprovodn. **20**, 503 (1986) [Sov. Phys. Semicond. **20**, 315 (1986)].
[4] P. V. Pavlov, V. D. Skupov, and D. I. Tetel'baum, Fiz. Khim. Obrab. Mater. No. 6, 19 (1987).
[5] V. D. Skupov, D. I. Tetel'baum, and V. G. Shengurov, Pis'ma Zh. Tekh. Fiz. **15**(22), 44 (1989) [Sov. Tech. Phys. Lett. **15**, 890 (1989)].
[6] V. D. Skupov and D. I. Tetel'baum, Fiz. Tekh. Poluprovodn. **21**, 1495 (1987) [Sov. Phys. Semicond. **21**, 910 (1987)].
[7] P. V. Pavlov, V. I. Pashkov, and V. D. Skupov, Élektronnaya Tekhnika Ser. 7 TOPO **6**(103), 24 (1980).

Translated by R. M. Durham

Discrimination of acetone and ammonia vapor using an array of thin-film sensors of the same type

V. V. Kisin, V. V. Sysoev, and S. A. Voroshilov

Saratov State Technical University
(Submitted March 5, 1999)
Pis'ma Zh. Tekh. Fiz. **25**, 54–58 (August 26, 1999)

It is shown that a gas mixture can be discriminated by using an array of thin-film semiconductor sensors having variable internal parameters. It is established that a multisensor system consisting of an array of sensors, fabricated by the same technological process but having a spread of active-layer parameters, can discriminate between ammonia and acetone vapor impurities in air. © *1999 American Institute of Physics.* [S1063-7850(99)02408-8]

It is usually assumed that the low selectivity of semiconductor gas-sensitive materials limits their possible applications in devices for identifying and analyzing gases. Hence, numerous methods have been developed to enhance the sensitivity of gas-sensitive semiconductor layers, including cyclic variation of the operating temperature, doping with various impurities, forming filters on the surface, and so on.[1] However, a semiconductor sensitive to a single gas is fairly rarely achieved. It is generally possible to talk of ''relative'' selectivity, i.e., the sensor responds to the action of a range of gases but the absolute values of the responses to these gases differ considerably. Since some gases cause an increase in the conductivity of the gas-sensitive layers and others cause a decrease, it is not too difficult to identify different types of gases. For gases of the same type, the problem appears at first glance to be insoluble, since a single sensor cannot determine whether a change in the conductivity of the layer has been caused by the type of gas or its quantity (concentration).

This aside, the problem can be solved because, even though not absolutely selective, semiconductor structures satisfy the constraints imposed on sensors in multisensor odor-discrimination systems. These systems identify different gases by analogy with the olfactory system of mammals and they are therefore called[2,3] ''electronic noses.'' There has recently been a tendency to construct multisensor systems using sensors fabricated by a common technology[4] since in principle these be used to produce relatively cheap integrated odor-identification systems in which the sensors and signal processing systems can be formed on the same substrate.

The aim of the present study was to determine whether gases of the same type could be distinguished using a multisensor system comprising an array of gas-sensitive resistors, fabricated in the same technological process, but having some spread of parameters.

Thin semiconducting films of tin oxide were deposited by magnetron sputtering on a polished 15×15 mm substrate and equipped with metallization configured such that after cutting up the wafers, up to 100 chips of triple-electrode resistive gas sensors could be fabricated, each having the topology described in Ref. 5. The dependences of the sensitivity of the active layer to a particular gas on the film parameters (thickness and doping level) had clearly defined maxima.[6] Thus, the sensitivity of the films was optimized for acetone vapor by selecting the deposition conditions using a

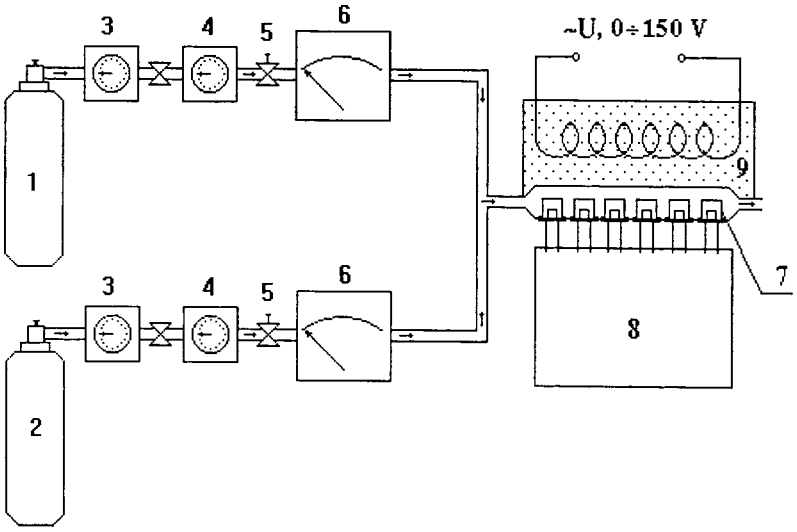

FIG. 1. Schematic of apparatus to study the response of a multisensor system: *1*, *2* — cylinders containing gas mixture and air, *3*, *4* — high and low-pressure reducers, *5* — flow regulator, *6* — flowmeter, *7* — sensor, *8* — measuring unit, and *9* — thermostat.

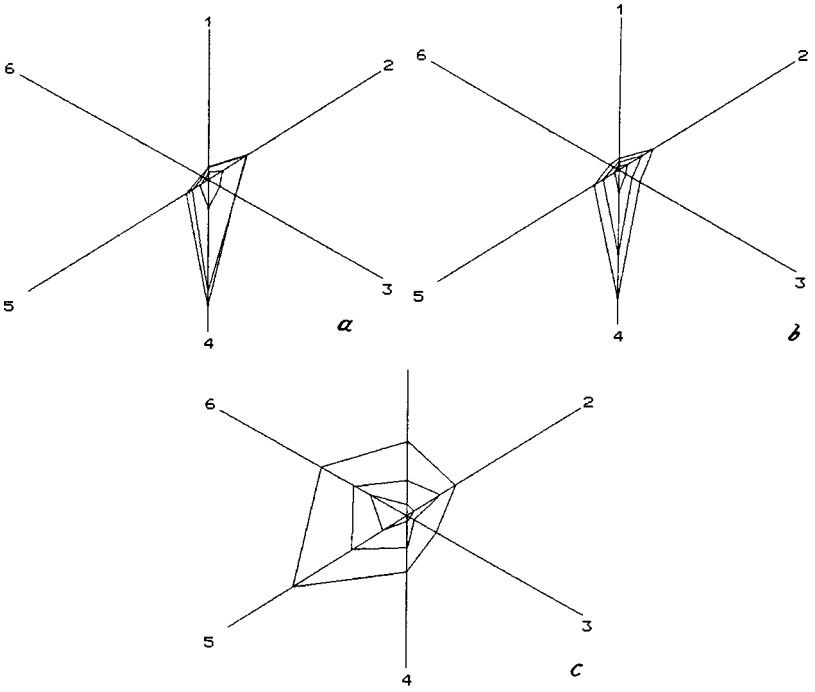

FIG. 2. Normalized signals from sensors forming multisensor system to three impurity concentrations: ethanol (a), acetone (b), and ammonia (c) in air. The signals are normalized to the maximum response of one of the sensors.

method described in Refs. 7 and 8. The gas sensitivity was defined as the degree of change in the conductivity of the layer in a test medium relative to the conductivity in pure air (79% N_2 and 21% O_2).

A schematic diagram of the measuring apparatus is shown in Fig. 1. In order to achieve identical operating conditions for all the sensors in the system, these were inserted in a solid copper thermostat. The operating temperature (around 400°C) was monitored using a chromel–alumel thermocouple and was maintained to within $\pm 2\%$. The response of the system was studied to the action of three gases, ethanol, acetone, and ammonia vapor, over a wide range of concentrations (10^2-10^4 ppm). Gas–air mixtures were prepared by mixing artificial air and saturated gas vapor in different proportions. The gas flow rate was selected so that the actuation times of the sensors in the measuring chamber were fairly short. A typical actuation time determined at 0.9 of the maximum signal did not exceed 3 min.

Sensors whose active layer was formed in the same technological process had a spread of gas sensitivity. In order to form the multisensor system, we selected six sensors from the same batch whose sensitivity differed most strongly. If the signals from the sensors forming the system are represented as a lobe diagram without any significant treatment (Fig. 2), it can be seen that it is impossible to distinguish the response of the system to the action of acetone and ethanol vapor. Conversely, the response of the system to the action of ammonia is quite different and is easily distinguished from the response to acetone or ethanol. An analysis of the response of the multisensor system to the action of gases using a correlation analysis technique described in Ref. 9 shows that the responses of the multisensor system to ethanol and acetone vapor are well correlated (see Table I). The response to the action of ammonia correlates poorly with the response to the action of ethanol and acetone vapor so that these can be reliably distinguished.

Ethanol and acetone clearly react in approximately the same way with the surface of tin oxide, possibly because when they undergo dissociation and oxidation, they form various similar radicals so that they are difficult to distinguish. However, the physical and chemical processes accompanying the interaction between the surface of tin oxide and ammonia differ substantially from those accompanying the interaction of the surface with ethanol and acetone. Thus, an array of sensors whose active layers have a slightly variable ''internal parameter'' can identify these gases as a result of the dependence of the gas-sensitive properties on the film parameters specific to each gas.

To sum up, a difference between the properties of sensors, even when these are fabricated in the same technological process, can be used to identify various gases even when these change the conductivity in the same direction, for example, to distinguish between acetone and ammonia. After

TABLE I. Correlation coefficient between responses of multisensor system to three gas impurities in air.

Gas	Ethanol, ppm			Acetone, ppm			Ammonia, ppm		
	1100	5040	10200	960	5930	9680	100	860	6900
Ethanol	0.99	1	1	1	0.99	0.98	−0.36	−0.31	−0.43
Acetone	0.96	0.99	0.98	0.98	1	1	−0.24	−0.21	−0.32
Ammonia	−0.44	−0.34	−0.39	−0.43	−0.26	−0.24	0.99	0.95	1

the type of gas has been established, it is easy to determine its quantity since the concentration dependence of the sensor sensitivity is usually known for each gas.

[1] B. F. Myasoedov and A. V. Davydov, Zh. Anal. Khim. **45**, 1259 (1990).
[2] K. Persaud and G. Dodd, Nature (London) **299**, 352 (1982).
[3] J. W. Gardner and P. N. Bartlett, Sens. Actuators B **33**, 60 (1996).
[4] I. Lundstrom, R. Erlandsson, U. Frykman *et al.*, Nature (London) **352**, 47 (1991).
[5] V. V. Kisin, S. A. Voroshilov, V. V. Sysoev, and V. V. Simakov, Prib. Tekh. Éksp. No. 5, 178 (1995).
[6] S. A. Voroshilov, Author's abstract of dissertation for Candidate of Physicomathematical Science [in Russian], Saratov State University, Saratov (1998), 18 pp.
[7] V. V. Kisin, S. A. Voroshilov, V. V. Sysoev, and V. V. Simakov, Zh. Tekh. Fiz. **69**(4), 112 (1999) [Tech. Phys. Lett. **44**, 452 (1999)].
[8] V. V. Kisin, V. A. Elistratov, and B. M. Gur'ev, Prib. Tekh. Éksp. No. 5, 244 (1993).
[9] R. Muller, *Multisensor Signal Processing*, in *Sensors, a Comprehensive Survey*, Vol. 1, *Fundamentals and General Aspects*, edited by W. Gopel, J. Hesse, and J. N. Zemel (VCH, Weinheim, 1989), pp. 313–330.

Translated by R. M. Durham

Annealing of aluminum–silicon-dioxide–silicon structures after α-particle bombardment

S. V. Vasin, V. B. Tulvinskiĭ, and É. T. Shipatov

Ulyanovsk State University, Russia
(Submitted March 22, 1999)
Pis'ma Zh. Tekh. Fiz. **25**, 59–62 (August 26, 1999)

An investigation is made of the isochronous annealing of Al–SiO_2–Si structures in the temperature range 20–450 °C after bombardment with α-particles from a Cm^{244} radioisotope source. In this temperature range it is observed that the positive charge in the insulator falls below the initial values. The hypothesis is put forward that this effect may be the result of defect formation and structural rearrangements near the Si/SiO_2 interphase boundary during irradiation and annealing. © *1999 American Institute of Physics.* [S1063-7850(99)02508-2]

Studies of defect generation and annealing processes in MOS structures are highly topical in solid-state electronics. However, despite an appreciable number of experimental and theoretical studies (see, for example, Refs. 1 and 2), some problems have not received due attention in the literature. These must include defect generation and annealing processes in the SiO_2 film and at the Si/SiO_2 interphase boundary, induced by radiation treatment. These processes are studied in the present paper.

Samples of MOS capacitors were fabricated using phosphorus-doped *n*-type silicon having a resistivity of 6.5 $\Omega\cdot$cm. A 100 nm thick oxide layer was grown by thermal oxidation at 1050 °C in a dry oxygen atmosphere with added 3% HCl. Electron beam evaporation was used to deposit an aluminum film on the SiO_2 surface, in which 1.1×1.1 mm contact areas were formed by photolithography. Ohmic contact was provided by depositing a continuous aluminum film on the back of the silicon wafer after etching the oxide. Finally, the structures were annealed in a dry nitrogen atmosphere at 500 °C. The structures were bombarded with α-particles from a Cm^{244} radioisotope source (α-particle energy 4 MeV, fluence 6×10^9 cm^{-2}). After bombardment the samples underwent isochronous annealing ($t=30$ min) in air in the temperature range 20–450 °C. The parameters of the MOS structures were monitored by measuring the rf (1 MHz) capacitance–voltage characteristics from which we determined the charge density at the traps in the insulator Q_{ot} and the density of surface states D_{it} at the Si/SiO_2 interface (Terman method[3]).

The results are plotted in Fig. 1. The ''average'' density $\langle D_{it}\rangle$ in Fig. 1b corresponds to the integral density $D_{it}(E)$ in the silicon band gap E_g in the energy range ±0.2 eV relative to the midgap value E_g at the Si/SiO_2 interface. It can be seen from Fig. 1a that during annealing the charge in the insulator reaches its initial (pre-irradiation) values by ~80 °C and continues to fall up to 250–270 °C, so that the minimum charge density is more than two orders of magnitude lower than that in the unirradiated samples. A further increase in temperature leads to an increase in charge which recovers to its initial level at ~450 °C.

Before irradiation, the surface-states density $D_{it}(E)$ at the Si/SiO_2 interphase boundary within the silicon band gap E_g has a standard U-shaped profile with a broad minimum at midgap. As a result of the α-irradiation, $D_{it}(E)$ increases abruptly over the entire width E_g, keeping the same profile. It can be seen from Fig. 1b that the integral density $\langle D_{it}\rangle$, calculated near the midgap E_g (±0.2 eV), decreases continuously with increasing temperature, with the maximum slope at 250–270 °C which corresponds to the minimum on the $N_{ot}(T)$ curve.

As the temperature increases to ~450 °C, the density of interphase states D_{it} returns to its initial level, like the charge density Q_{ot}, which may indicate that the physical processes determining the relaxation of Q_{ot} and D_{it} under post-irradiation annealing are similar and interrelated.

We postulate that these dependences are mainly a consequence of the intense defect formation in the Si–SiO_2

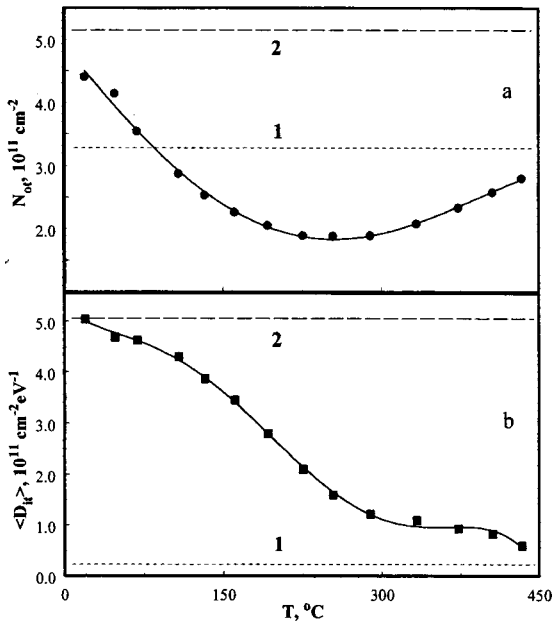

FIG. 1. Curves of isochronous annealing of the fixed charge density in SiO_2 (a) and density of surface states at the Si/SiO_2 interface (b) of irradiated structures. The horizontal line gives the values: *1* — before and *2* — after irradiation.

structure under α-irradiation, which is intensified by the presence of appreciable mechanical stresses at the Si/SiO_2 interface[4] and an increased hydrogen concentration in the SiO_2 near the interface.[5] Radiation-induced defects, i.e., electron traps and holes in SiO_2, are created as a result of atomic displacements and breaking of Si–Si and Si–O bonds, as well as Si–H and Si–OH bonds accompanied by the release of hydrogen atoms which passivated interphase surface states. This results in the formation of P_b centers, which are the main sources of interphase states, and also leads to the generation of Q_{ot}^+ and Q_{ot}^- charges at traps in SiO_2 formed by radiation defects. The positive charge Q_{ot}^+ is made up of the charge of trapped holes and also protons mainly concentrated near the Si/SiO_2 and Al/SiO_2 interfaces.[5] Under annealing, this charge relaxes rapidly as a result of tunneling and thermal emission processes involving valence electrons,[6] initiation of hopping conduction of the holes in SiO_2, retrapping of protons at broken bonds, and annealing of the radiation defects.

As far as the negative charge Q_{ot}^- is concerned, the more mobile electrons in the SiO_2 are trapped in smaller quantities than the holes, which is confirmed by the sign of the sum charge after irradiation. We know from studies of the optical charging of $Si–SiO_2$ structures (see, for example, Ref. 7) that the negative charge in these structures is annealed with an appreciable temperature delay. In *n*-Si as in our case, the delay may be caused by the electrons leaving the traps being compensated by an influx from the silicon conduction band. The necessary n^+ layer at the SiO_2 interface is created by the enhanced phosphorus concentration near this boundary.

If these two curves $Q_{ot}^+(T)$ and $Q_{ot}^-(T)$ are combined, we obtain the sum curve with a minimum, as can be seen from Fig. 1a. Additional measurements of these structures after β-particle bombardment from an $Sr^{90} + Y^{90}$ source yielded similar results which clearly indicate the importance of ionization and below-threshold mechanisms of defect formation, including the generation of defects as a result of relaxation of mechanical stresses in $Si–SiO_2$ (Ref. 4).

[1] R. A. B. Devine, IEEE Trans. Nucl. Sci. **41**, 452 (1994).
[2] T. R. Oldham, F. B. McLean, H. E. Jr. Boesch *et al.*, Semicond. Sci. Technol. **4**, 986 (1989).
[3] P. S. Winokur, J. R. Schwank, P. J. McWhorter *et al.*, IEEE Trans. Nucl. Sci. **31**, 1453 (1984).
[4] V. S. Pershenkov, V. D. Popov, and A. V. Shal'nov, *Surface Radiation Effects in Elements of Integrated Microcircuits* [in Russian], Énergoatomizdat, Moscow (1988), 256 pp.
[5] Yu. V. Gorelkinskiĭ, N. N. Nevinnyĭ, and E. A. Lyuts, Poverkhnost' No. 6, 79 (1994).
[6] P. J. McWhorter, S. L. Miller, and W. M. Miller, IEEE Trans. Nucl. Sci. **37**, 1682 (1990).
[7] V. S. Vavilov, V. F. Kiselev, and B. N. Mukashev, *Defects in Silicon and at its Surface* [in Russian], Nauka, Moscow (1990), 216 pp.

Translated by R. M. Durham

Control of chaos in nonautonomous systems with quasiperiodic excitation

A. Yu. Zhalnin

Institute of Radio Engineering and Electronics, Russian Academy of Sciences (Saratov Branch)
(Submitted January 26, 1999)
Pis'ma Zh. Tekh. Fiz. **25**, 63–70 (August 26, 1999)

A procedure is suggested for controlling chaos in quasiperiodically excited systems by stabilizing an unstable torus, or creating a new one by means of a small action. For this purpose the controlled system is synchronized with one which is similar but in a state of stable quasiperiodic motion. The method is illustrated for a quasiperiodically perturbed logistic mapping and a Duffing oscillator. © *1999 American Institute of Physics.* [S1063-7850(99)02608-7]

1. INTRODUCTION

Controlling chaos is one of the most practically relevant directions in nonlinear physics. The most common method is the Ott–Grebogi–Yorke method of stabilizing unstable periodic orbits[1] and various modifications of this.[2,3] Its efficiency has been demonstrated for many autonomous and periodically excited systems. However, the problem of control in systems exposed to more complex multifrequency action has been left to one side. The present paper is devoted to searching for methods of solving this problem in the simplest case of a biharmonic action with two nonmultiple frequencies.

We shall analyze some characteristic features which are imposed on the control problem by the quasiperiodicity of the action. Primarily, this results in the absence of unstable periodic orbits which could be stabilized. The way out here is to use an unstable torus which can exist in the phase space of these systems. This is created as a result of bifurcations such as ''doubling'' and loss of torus symmetry and after a transition to chaos, is embedded in a chaotic attractor or exists outside it. However, the standard control procedure either requires a knowledge of the orbit being stabilized or the presence of an oscillator which generates a suitable reference signal.[1,2] A torus is a topologically more complex object than a cycle and a model of the global dynamics of the system is required to reconstruct it. The construction of such a model and the search for an unstable torus is in itself a fairly complex problem. Hence it is more productive to search for a suitable reference oscillator. As a reference orbit to stabilize an unstable torus, it seems reasonable *a priori* to use a torus evolutionally coupled with it, which existed in the system for other parameters (before loss of stability). The aim of the present study is to demonstrate the possibility of implementing this idea. A procedure is describing for stabilizing an unstable torus or creating a new orbit in its vicinity by locking the controlled system to one which is similar but in a state of stable quasiperiodic motion. This is illustrated for a quasiperiodically perturbed logistic mapping and a Duffing oscillator.

2. STABILIZATION OF AN UNSTABLE INVARIANT MAPPING CURVE

We shall analyze the two-dimensional mapping

$$x_{n+1}=f(x_n,\theta_n)=\lambda-x_n^2-\varepsilon\cos 2\pi\theta_n,$$
$$\theta_{n+1}=\theta_n+\omega, \bmod 1, \tag{1}$$

where $\omega=(\sqrt{5}-1)/2$ is the ''golden cross section.'' This mapping demonstrates a torus doubling bifurcation and a transition to a strange nonchaotic attractor and chaos. The unstable invariant curve generated by the torus doubling $x=\varphi(\theta)$, $0\leqslant\theta\leqslant 1$ is embedded in a chaotic attractor (Fig. 1a). In order to stabilize the invariant curve, we can model the mapping (1) as follows:

$$x_{n+1}=f(x_n,\theta_n)+g(x_n,\theta_n),$$
$$\theta_{n+1}=\theta_n+\omega, \bmod 1, \tag{2}$$

where the function $g(x,\theta)$ is the control action which must satisfy the following two constraints:

$$g(\varphi(\theta),\theta)=0,$$
$$\int_0^1 \ln|f_x'(\varphi(\theta),\theta)+g_x'(\varphi(\theta),\theta)|\,d\theta<0.$$

The first constraint implies that as the trajectory approaches the invariant curve, the control action tends to zero, while the second implies that the average Lyapunov exponent along the invariant curve is negative and the invariant curve becomes stable. The function $g(x,\theta)$ may be taken in the standard form of a proportional control action

$$g(x,\theta)=C(x-\varphi(\theta)),$$

where C is the coupling parameter. Then, in accordance with the fundamental idea of the method we note that the invariant mapping curves (1) in different regions of parameter space are fairly similar, as we can see from Fig. 1b where the thin line $x(\theta)$ is the unstable torus of the mapping (1) from the chaos region, and $y(\theta)$ is a stable torus from some other region. It is easily seen that the following relation holds:

$$x(\theta)\approx Sy(\theta+\tau)+B,$$

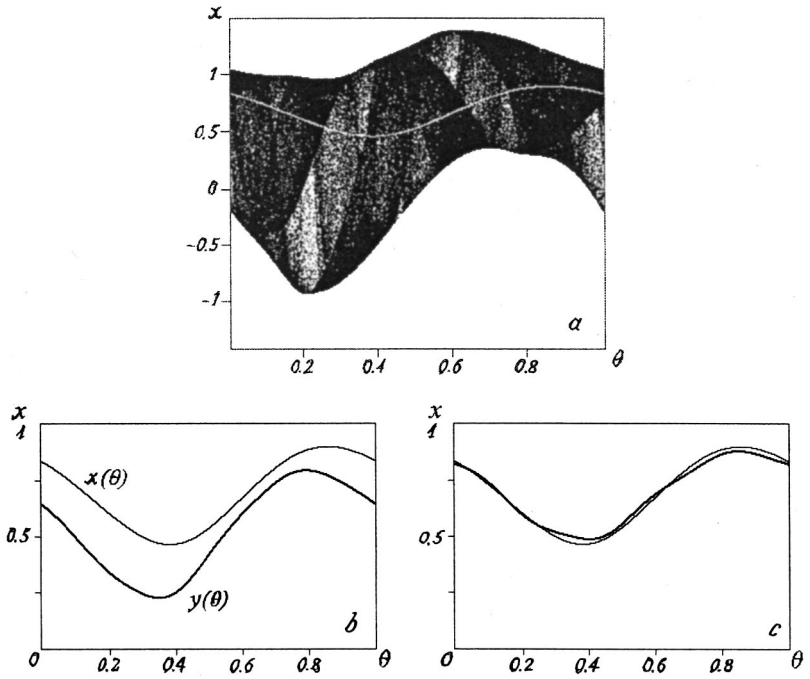

FIG. 1. a — Chaotic attractor and unstable torus of mapping (1) embedded in it (*1*) ($\lambda=1.2$, $\varepsilon=0.2$); b — thin line $x(\theta)$ — unstable torus from region of chaotic dynamics of parameter space being stabilized ($\lambda=1.2$, $\varepsilon=0.2$), thick line $y(\theta)$ — stable torus of mapping (1) used as reference trajectory for control ($\lambda=0.85$, $\varepsilon=0.2$); c — thin line — unstable torus of mapping (1), thick line — torus of mapping (3.1, 3.3) obtained from (1) by using the control procedure (for the same values of the parameters).

and the curve from its region of stability can be reduced to the form of an unstable curve from the chaos region with, a fairly high degree of accuracy, by means of a proportional contraction/expansion along the x axis and a shift parallel to the coordinate axes. The function $g(x,\theta)$ thus has the form

$$g(x_n,\theta_n)=C(x_n-Sy_n(\theta_n+\tau)-B),$$

where the parameters S and B determine the contraction/expansion and the parallel shift of the invariant curve, and τ is the phase shift. Finally, the mapping can be written in the form

$$x_{n+1}=\lambda_1-x_n^2+\varepsilon\cos 2\pi\theta_n+C(x_n-Sy_n-B), \tag{3.1}$$

$$y_{n+1}=\lambda_2-y_n^2+\varepsilon\cos 2\pi(\theta_n+\tau), \tag{3.2}$$

$$\theta_{n+1}=\theta_n+\omega,\ \mathrm{mod}\,1, \tag{3.3}$$

where λ_1 is the value of the parameter for which chaos and an unstable torus exist in the mapping (1), and λ_2 is the value for which a stable torus exists, which is used as the reference trajectory.

The results of applying the stabilization algorithm are plotted in Fig. 1c. The thin line gives the unstable invariant mapping curve (1) and the thick line gives the stable torus obtained as a result of applying the control procedure. These last two lines are almost matched. The accuracy of their matching depends on the successful choice of parameters of the reference mapping (3.2–3.3) and the coupling parameters. The dependence of the controlling action decreases to a level which is no more than 5% of the variation in the parameters needed to transfer the controlled mapping to the region of regular dynamics, which suggests that the control problem has been solved.

3. FLUX MODEL

Since a one-dimensional irreversible logistic mapping is not a Poincaré cross section of any flux, we need to demonstrate separately that the proposed control method can be applied to models in the form of a system of differential equations. As such we take a biharmonically excited Duffing model, which has many physical analogs:

$$\ddot{x}+2\lambda\dot{x}+x+x^3=f_1\cos\omega_1 t+f_2\cos\omega_2 t, \tag{4}$$

where $\omega_1/\omega_2=(\sqrt{5}-1)/2$. Since a Duffing oscillator possess a symmetric potential, the transition to chaos in this system should be preceded by symmetry-loss bifurcations of the torus. The resulting unstable torus is embedded in a chaotic attractor (Fig. 2a). To stabilize this, we modify Eq. (4) by adding a control action in a form known as continuous proportional feedback:[2]

$$\ddot{x}+2\lambda\dot{x}+x+x^3=f_1\cos\omega_1 t+f_2\cos\omega_2 t+g(x,t), \tag{5}$$

$$g(x,t)=C(x-Sy(t)),$$

where $y(t)$ is a reference signal obtained by integrating Eq. (4) numerically for values of the parameters corresponding to the stable symmetric torus regime. These parameters are determined by trial and error: we decrease the amplitude of the fundamental-frequency signal f_1 until we enter the symmetric torus regime, after which finer tuning is achieved by varying the amplitude of f_2. As a result of the symmetry of the system, the parameters B and τ [see Eq. (3)] are zero and because of the low sensitivity of the torus to variations in the parameters, S is close to unity.

The results of applying the control procedure are plotted in Fig. 2b. It can be seen that the torus and reference orbit do not agree at all, However, the control action does not exceed 8% of the variation in the principal control parameter f_1

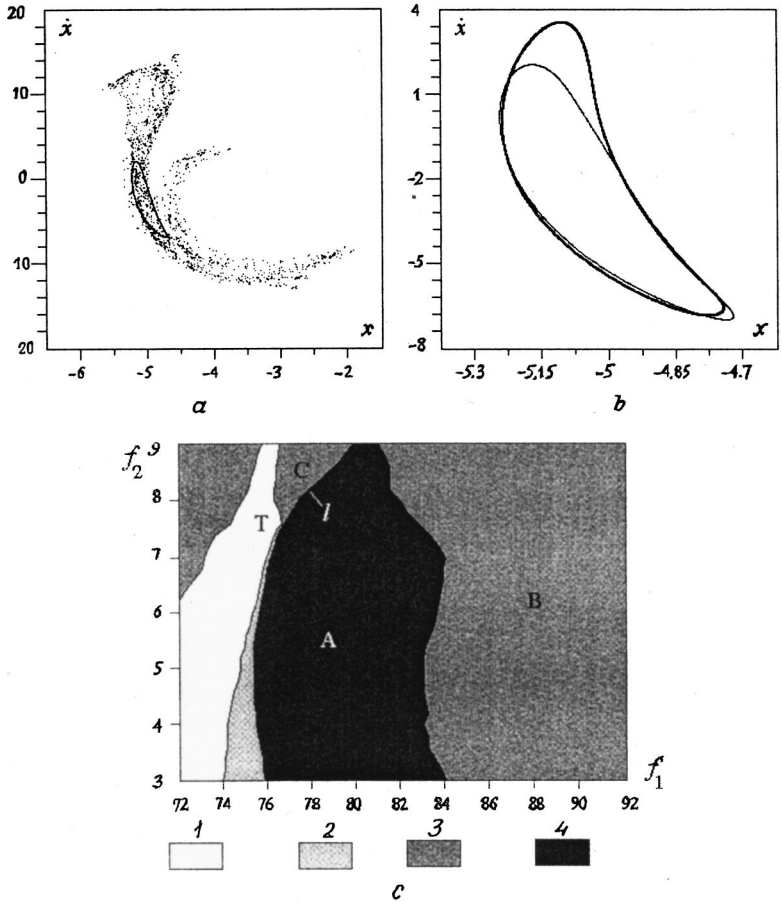

FIG. 2. Cross section of chaotic attractor and unstable torus of biharmonically excited Duffing oscillator($f_1=78$, $f_2=5$, $\lambda=0.1$, $\omega_1=1.5$) (a). Results of applying the control procedure: thin line — cross section of reference torus, thick line — stabilized (for the same parameters as a and b). Fragment of the cross section of the parameter space of a biharmonically excited Duffing oscillator ($\lambda=0.1$, $\omega_1=1.5$) (c). *1* — symmetric torus, *2* — asymmetric torus, *3* — chaos, and *4* — region in which control is possible.

needed to transfer the system to a state with regular dynamics and thus, in this case we can talk of chaos control.

The extent of the region of applicability of the proposed control method can be estimated from Fig. 2c. In region *A* this control procedure can be applied. In region *B* this is impeded by the increasing deformation of the unstable torus, since this region is extremely far from the region of existence of a stable symmetric torus. In region *C*, control cannot be applied because of the device characteristics of the parameter space imposed by the quasiperiodicity of the action. The bifurcation line of the torus symmetry loss truncates at point *T*, which is the critical point of codimensionality 2. Thus, a transition to chaos can take place in the system without loss of symmetry and the creation of an unstable torus (above point *T*). Thus, the region of chaos is divided into two sections: *A*–*B* (with an unstable torus) and *C* (no torus). These sections are divided by the line *l* on which the unstable torus is disrupted by (preferably) internal contact between the chaotic attractor boundaries. Thus, in region *C* there is no object to which the stabilization procedure can be applied.

CONCLUSIONS

These results indicate that the proposed chaos control procedure of stabilizing an unstable torus is effective in systems exposed to a quasiperiodic action.

The proposed method can be used to control chaos in real physical systems because of the universal nature of the structures of bifurcation sets of quasiperiodically excited systems of various types, which was demonstrated in Ref. 4 for a quasiperiodically excited logistic mapping and a diode resonator in the vicinity of the critical end point of the torus doubling bifurcation line. Universality implies the presence of identical regions of existence of regular and chaotic dynamics, unstable orbits, and bifurcation transitions. This means that the method described can be applied to a system of two unidirectionally coupled *LR*-diode circuits.

This work was supported by the Russian Foundation for Basic Research Grant No. 96-02-16755 and also by the ''Integration'' Federal Program, Grant No. 696.3.

[1] E. Ott, C. Grebogi, and J. A. Yorke, Phys. Rev. Lett. **64**, 1196 (1990).
[2] K. Pyragas, Phys. Lett. A **170**, 421 (1992).
[3] V. V. Astakhov, A. N. Sil'chenko, G. I. Strelkova *et al.*, Radiotekh. Elektron. **41**, 1323 (1996).
[4] B. P. Bezruchko, S. P. Kuznetsov, A. S. Pikovskiĭ *et al.*, Izv. Vyssh. Uchebn. Zaved. Prikl. Nelin. Dinam. **5**(6), 3 (1997).

Translated by R. M. Durham

Information transmission using a synchronous chaotic response with filtering in the communication channel

A. S. Dmitriev and L. V. Kuz'min

Institute of Radio Engineering and Electronics, Russian Academy of Sciences, Moscow
(Submitted January 28, 1999)
Pis'ma Zh. Tekh. Fiz. **25**, 71–77 (August 26, 1999)

A principle is proposed for obtaining a chaotic synchronous response in a driven nonlinear oscillatory system under conditions where the signal of the driving chaotic system is filtered by the coupling channel. Music and speech signals are used to demonstrate the efficiency of applying this principle to transmit information through a channel having a limited frequency band. © *1999 American Institute of Physics.* [S1063-7850(99)02708-1]

The use of dynamic chaos to transmit information, particularly confidential information, has attracted close attention among researchers.[1–7] Among the various proposed systems, success was achieved with a system for nonlinear mixing of an information signal with a chaotic one, introduced in Ref. 3 using a ring oscillator[8,9] as the chaos source. This system proved effective for transmitting information in the low-frequency[10] and radio-frequency ranges,[11,12] and was also used in experiments in the optical range,[13] where the chaos source was an oscillator consisting of a laser amplifier and a fiber-optic cable as a delayed-feedback element. However, the system[3] also exhibits fairly high sensitivity to amplitude-frequency distortions of the signal in the channel.

In order to eliminate perturbations associated with amplitude-frequency distortions in the channel, it was logical to use correcting elements in the form of filters with a response the reciprocal of the effective channel filter, at the entrance to the receiving devices. However, studies carried out in Refs. 14 and 15 showed that this approach is ineffective since, for many of the most interesting cases, an exact solution of the correction problem is either lacking or difficult to achieve, and an approximate solution does not give the desired improvement in the quality of the chaotic synchronous response.

In the present paper we propose a new approach to the extraction of information by means of a chaotic synchronous response in a nonlinear oscillatory system in the presence of the filtering properties of the channel, and we report the main results of an investigation of the information extraction process. The idea of the approach is to incorporate elements having filtering properties equivalent to those of the channel in the transmitter (driving chaotic system) and receiver (driven nonlinear oscillatory system).

A functional diagram demonstrating the principle of obtaining a chaotic synchronous response and extracting the information component from the chaotic signal (Fig. 1) consists of a transmitter I, a detector II, and a coupling channel III which filters the incoming chaotic signal from the information component. The transmitter incorporates a nonlinear subsystem *1* consisting of an instantaneous-response nonlinear converter and a first-order low-pass filter (Fig. 1b) and a linear subsystem *2* comprising a second-order low-pass filter (Fig. 1c), a summator and filter *3* (Fig. 1d) whose properties are equivalent to those of the channel filter. The receiver consists of the same elements with the summator replaced by a subtractor. If element *3* is eliminated from the transmitter and receiver, and the coupling channel is considered to be ideal, the system is reduced to that introduced in Ref. 3.

In the presence of a chaotic synchronous signal and the absence of an input information signal, i.e., $S=0$, the signal leaving the subtractor in the detector is $S_f=U-Z_2=0$. If we consider the propagation of an information signal $S\neq 0$ through the circuit elements, we can confirm that the information signal at the detector exit S_f is a copy of the signal S

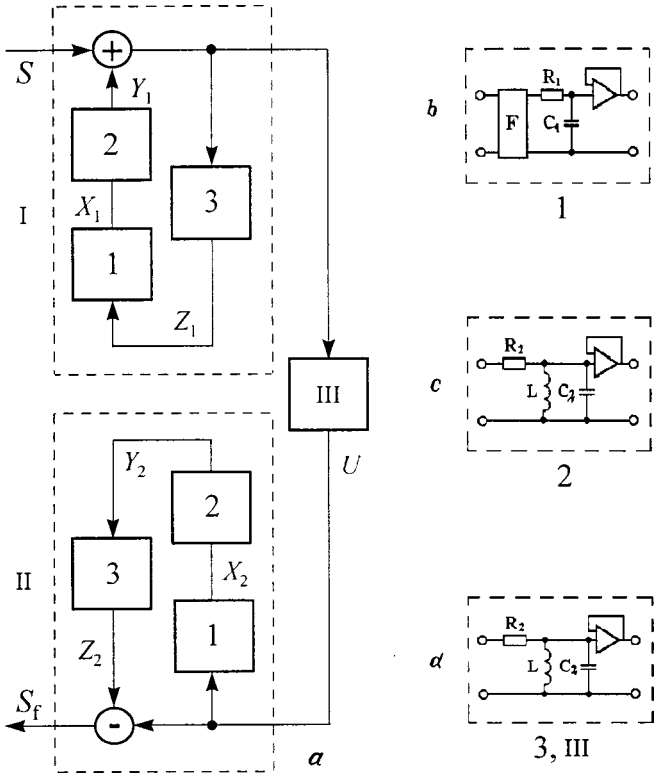

FIG. 1. Schematic of transmission system: I — transmitter, II — receiver, and III — coupling channel.

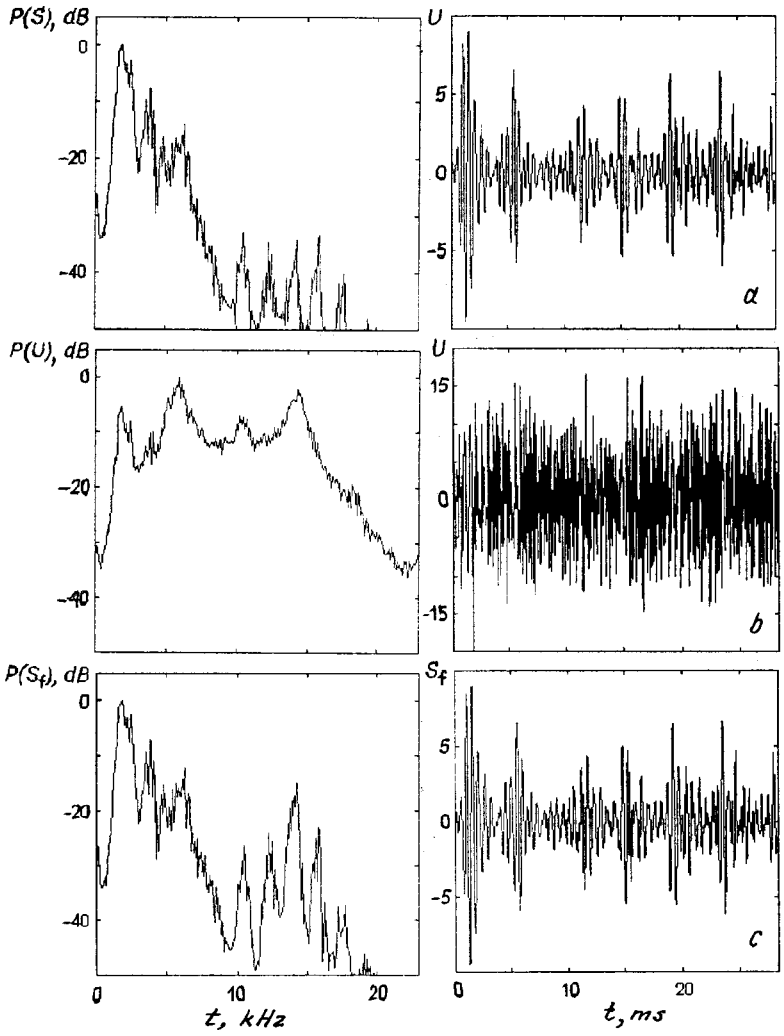

FIG. 2. Power spectra and signal fragments for a signal power/chaos power ratio of −6 dB: a — information signal S, b — sum U of chaotic and information signals after channel filter, and c — information signal S_f.

passed through the filter *3*. It thus remains for us to determine: (a) whether the ring oscillator remains a source of chaos when the additional filter *3* is introduced; (b) whether it will be possible to obtain a chaotic synchronous response in the detector; and (c) whether the chaotic synchronous response is stable in the strong or weak sense (this determines the presence or absence of on–off intermittence[16–18] and also the level of distortions of the information signal in the detector).

Let us assume, to be specific, that III and therefore *3* are second-order bandpass filters. Then, the normalized equations for the information transmission system are:

$$
\begin{aligned}
&T\dot{X}_1+X_1=F(Z_1),\\
&\ddot{Y}_1+\alpha_1\dot{Y}_1+Y_1=X_1,\\
&\ddot{Z}_1+\alpha_2\dot{Z}_1+\omega^2 Z_1=\omega^2(\dot{Y}_1+\dot{S}),\\
&\ddot{U}_1+\alpha_2\dot{U}_1+\omega^2 U_1=\omega^2(\dot{Y}_1+\dot{S}),\\
&T\dot{X}_2+X_2=F(U),\\
&\ddot{Y}_2+\alpha_1\dot{Y}_2+Y_2=X_2,\\
&\ddot{Z}_2+\alpha_2\dot{Z}_2+\omega^2 Z_2=\omega^2\dot{Y}_2.
\end{aligned}
\qquad (1)
$$

The first three equations in (1) describe the transmitter, the fourth describes the channel, and the last three describe the detector. The first equation describes the nonlinear subsystem *1* consisting of a series-connected instantaneous-response nonlinear converter having the characteristic

$$F(U,m)=m[|U+S|-|U-S|+(|U-1|-|U+1|)/2], \qquad (2)$$

where m is a parameter, and a first-order low-pass filter; the next equation describes the linear subsystem comprising a second-order low-pass filter; the third equation describes the second-order bandpass filter of the oscillator; the fourth equation describes the same filter but for the propagation of the signal through the coupling channel, S is the information signal, and Y_1+S is the signal entering the channel and at the entrance of the transmitter bandpass filter.

Thus, the driving system in Fig. 1 is an the oscillator with a first-order low-pass filter, a second-order low-pass filter, and a second-order bandpass filter. We know[19] that in these oscillators there is a region of chaotic oscillations and a region of hyperchaos, so that condition (a) is satisfied.

The system of equations (1) has a solution whose trajectories in twelve-dimensional phase space lie entirely in the seven-dimensional hyperplane determined by the conditions:

$$X_1 = X_2, \quad Y_1 = Y_2, \quad \dot{Y}_1 = \dot{Y}_2, \quad Z_1 = U, \quad \dot{Z}_1 = \dot{U}. \qquad (3)$$

If these solutions are stable under the action of small perturbations, the steady-state oscillations of the driven system induced by the chaotic action of the driving system are a chaotic synchronous response. In order to obtain a chaotic synchronous response and extract information, we used the hyperchaos regime of the transmitter with the parameters $m = 35$, $T = 0.2$, $\alpha_1 = 0.3$, $\alpha_2 = 0.2$, and $\omega = 2.5$. A necessary condition for the existence of a chaotic synchronous response is that the first Lyapunov exponent λ_1^2 of the detector should be negative. Direct calculations show that the necessary condition for locking stability is satisfied, and therefore condition (b) is satisfied. However, this is not sufficient to ensure stability of the chaotic synchronous response in the strong sense: the attractor of the system may have trajectory sections which are unstable in the transversal direction to the hyperplane of the locking attractor, which leads to on–off intermittence, i.e., randomly aperiodic disruptions of the locking regime.

Calculations made using a technique used in Ref. 17 showed that in this case the locking attractor has no sections with local instability transversal to the hyperplane, the synchronous response is stable in the strong sense, and no on–off intermittence occurs.

Computer experiments on information transmission were carried out using music and speech audio signals, and demonstrated the high precision of reconstructing the information component of the signal. Figure 2 shows corresponding power spectra and signal fragments.

To conclude, the proposed principle for obtaining a chaotic synchronous response in the presence of the filtering properties of the channel is effective. The principle has been demonstrated for a transmission system where the information signal is mixed with the chaotic one but it cannot be used in other information transmission systems, using chaos, for example in transmission systems with switching between chaotic regimes.

This work was supported by the Russian Fund for Fundamental Research (Grant No. 97-01-00800).

[1] L. Kocarev, K. S. Halle, K. Eckert *et al.*, Int. J. Bifurcation Chaos Appl. Sci. Eng. **2**, 709 (1992).
[2] K. Cuomo and A. Oppenheim, Phys. Rev. Lett. **71**(1), 65 (1993).
[3] A. R. Volkovskiĭ and N. F. Rul'kov, Pis'ma Zh. Tekh. Fiz. **19**(2), 71 (1993) [Tech. Phys. Lett **19**, 97 (1993)].
[4] Yu. L. Bel'skiĭ and A. S. Dmitriev, Radiotekh. Elektron. **38**, 1310 (1993).
[5] A. K. Kozlov and V. D. Shalfeev, Pis'ma Zh. Tekh. Fiz. **19**(23), 83 (1993) [Tech. Phys. Lett. **19**, 769 (1993)].
[6] M. Hasler, H. Dedieu, M. Kennedy *et al.*, in *Proceedings of International Symposium on Nonlinear Theory and Applications*, Hawaii, USA, 1993, pp. 87–92.
[7] S. Heyes, C. Grebogi, and E. Ott, Phys. Rev. Lett. **70**(20), 87 (1993).
[8] A. S. Dmitriev and V. Ya. Kislov, Radiotekh. Elektron. **29**, 2389 (1984).
[9] A. S. Dmitriev and V. Ya. Kislov, *Stochastic Oscillations in Radio Physics and Electronics* [in Russian], Nauka, Moscow (1989).
[10] A. S. Dmitriev, A. I. Panas, and S. O. Starkov, Int. J. Bifurcation Chaos Appl. Sci. Eng. **5**, 371 (1995).
[11] A. S. Dmitriev, A. I. Panas, S. O. Starkov *et al.*, Int. J. Bifurcation Chaos Appl. Sci. Eng. **7**, 32511 (1997).
[12] A. S. Dmitriev, L. V. Kuz'min, A. I. Panas *et al.*, Radiotekh. Élektron. **43**, 1115 (1998).
[13] G. D. VanWiggeren and R. Roy, Phys. Rev. Lett. **81**, 3547 (1998).
[14] T. L. Carroll, IEEE Trans. Circuits Syst., I: Fundam. Theory Appl. **42**(3), 105 (1995).
[15] T. L. Carroll and G. A. Johnson, Phys. Rev. E **57**, 1555 (1998).
[16] L. V. Kuzmin and A. I. Panas, in *Proceedings of Workshop Nonlinear Dynamics of Electronic Systems, NDES'97*, Moscow, Russia, 1997, pp. 485–490.
[17] E. Ott *et al.*, Phys. Rev. Lett. **71**, 4134 (1993).
[18] A. Chenys and H. Lustfeld, J. Phys. A **29**, 11 (1996).
[19] A. S. Dmitriev, A. I. Panas, and S. O. Starkov, Int. J. Bifurcation Chaos Appl. Sci. Eng. **6**, 851 (1996).

Translated by R. M. Durham

Modulational method of eliminating the zero shift of a fiber ring interferometer induced by polarization nonreciprocity

G. B. Malykin

Institute of Applied Physics, Russian Academy of Sciences, Nizhniĭ Novgorod, Russia
(Submitted January 25, 1999)
Pis'ma Zh. Tekh. Fiz. **25**, 78–82 (August 26, 1999)

A new method is proposed to eliminate the zero shift of a fiber ring interferometer induced by polarization nonreciprocity. This method is based on periodic modulation of the polarization state of nonmonochromatic radiation at the entrance to the interferometer ring system. Numerical estimates are given. © *1999 American Institute of Physics.* [S1063-7850(99)02808-6]

One of the main factors limiting the accuracy of measurements of angular rotation speed using fiber ring interferometers (FRIs) fabricated using single-mode fiber-optic waveguides is the zero shift of the interference between the counterpropagating waves at the FRI exit, caused by the polarization nonreciprocity of the FRI ring system.[1–3] As the fiber temperature of the FRI ring system varies, its length, birefringence, and therefore its polarization nonreciprocity vary, which leads to a change in the zero shift or zero drift.[1,2,4,5] Various methods are used to reduce the zero shift and drift in FRI systems, including polarizers,[1,2,4,5] nonmonochromatic radiation depolarizers,[6–8] or polarizers and depolarizers together.[9–12]

The aim of the present study is to propose a method of eliminating the zero shift of an FRI induced by polarization nonreciprocity which is based on periodic modulation of the polarization state of the nonmonochromatic radiation at the FRI entrance. In this case, no polarizers and depolarizers are required in the FRI system.

Note that these simple FRI systems were considered earlier,[3,13,14] but either the zero shift was estimated[3,14] or it was assumed that there is a zero drift for the linear conversion of the change in the angular velocity into a change in the intensity of the interference signal,[13] but the possibility of eliminating the zero shift of the FRI by polarization modulation was not considered.

We write an expression for the zero shift φ in an FRI system without a polarizer (see Fig. 1) whose ring system is fabricated using a single-mode fiber-optic waveguide of arbitrary birefringence:[3]

$$\varphi = \arctan \frac{\sin(\alpha_1+\alpha_2)\sin 4\chi \cos(\alpha_1-\alpha_2-2\eta)S_l + \sin 2(\alpha_1+\alpha_2)\cos 2\chi S_3}{2[\cos^2(\alpha_1+\alpha_2)+0.5\sin 2(\alpha_1+\alpha_2)\sin 2\chi]}, \quad (1)$$

where χ and $\alpha_{1,2}$ respectively characterize the ellipticity of the natural polarization modes of the FRI ring system and the orientation of the major axes of the ellipse at the ends of the ring system relative to some arbitrarily selected direction, for example, the plane of the end of the ring system, $S_l = \sqrt{S_1^2+S_2^2}$ is the linear component of the polarization of the nonmonochromatic radiation at the FRI entrance, η is the azimuth of S_l relative to a selected direction, and S_3 is the circular component of the polarization of the nonmonochromatic radiation at the FRI entrance (S_i are the components of the Stokes vector of the radiation[15]). Expression (1) is valid when $L \gg l_{\text{dep}}$, where L is the length of the FRI ring system, $l_{\text{dep}} = \lambda^2/\Delta\lambda\Delta n$ is the depolarization length of the nonmonochromatic radiation in the fiber, λ is the average wavelength of the radiation source, $\Delta\lambda$ is its spectral width, and Δn is the refractive index difference in the slow and fast axes of the fiber.

We shall now analyze expression (1). The denominator (1) does not depend on the polarization state at the FRI entrance, whereas the dependence of the numerator is such that if a mutually orthogonal polarization state exists at the FRI entrance rather than some given polarization state, the absolute value of the numerator will remain the same but its sign will be reversed. In fact, the two, generally elliptic, mutually orthogonal polarization states differ by the principal axis of the ellipse η being turned through 90° and by the direction of the ellipse circumference, i.e., by the sign of the circular component of the polarization. Thus, when the polarization state of the radiation changes to the mutually orthogonal state, the first term in the numerator of expression (1) changes sign as a result of a change in the value of 2η by 180° (S_l does not change) while the second term changes sign as a result of a change in the sign of the circular component of the polarization S_3.

Note that the change in the sign of φ and the conservation of its modulus when the polarization state changes to the

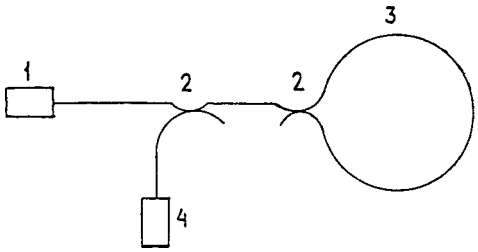

FIG. 1. Schematic of fiber ring interferometer: *1* — radiation source, *2* — beam splitters, *3* — ring system, and *4* — photodetector.

mutually orthogonal state will only take place in an FRI without a polarizer.

If the polarization state is modulated periodically (either harmonically or as a square wave) at the FRI entrance and the output signal is analyzed by averaging over a time considerably greater than the modulation period, the value of φ will only be caused by the Sagnac effect, i.e., by the rotation of the FRI and the contribution of the polarization nonreciprocity is averaged. If some type of modulator of the ring system length is used in the FRI,[16,17] the modulation frequency of the polarization state should be much lower than that of the ring system length.

At present various devices are available for modulating the polarization state of light in a single-mode fiber, whose operating principle is based on the photoelastic effect[18] or the Kerr effect.[19,20] When an integrated-optic phase modulator is used,[20] it is best to use an FRI system with an integrated-optic beam splitter.[21] The modulator should be positioned between the first and second beam splitters in the FRI circuit (see Fig. 1). The ellipticity of the polarization at the modulator exit may be arbitrary but one condition must be satisfied: the axis of the polarization ellipse must be oriented at an angle of 45° to the axes of birefringence of the modulator.

We shall estimate the zero shift and drift in the proposed FRI system assuming that the polarization state at the entrance is not ideally modulated, i.e., the polarization states in different half-periods are not completely orthogonal. We shall assume that at the modulator exit, almost linear polarization ($S_1 \approx 1$, $S_3 \approx 0.01$) with the azimuth $\eta \approx 0° \pm \pi N/2$, where N is an integer, exists in one half-period. In the second half-period the azimuth changes not by 90° but by 85°, while the circular component of the polarization changes its sign and its absolute value changes by 5% (the negligible change in the absolute value of the linear component of the polarization is insignificant in this case). We shall assume that the FRI ring system is 500 m long, the diameter is $D = 10$ cm and the parameters of the radiation source are $\lambda = 0.8\ \mu$m and $\Delta\lambda = 20$ nm. Here we shall consider two types of single-mode fiber in the FRI ring system: fibers having strong birefringence $\Delta n = 3 \times 10^{-4}$, $h = 10^{-5}\ \mathrm{m}^{-1}$ and fibers having weak birefringence $\Delta n = 10^{-6}$, $h = 5 \times 10^{-2}\ \mathrm{m}^{-1}$. For the estimates we shall also assume that the orientation of the intrinsic axes of birefringence of the fiber at the FRI exit is $\alpha_1 = -1°$, $\alpha_2 = 2°$ for the fiber with strong birefringence and $\alpha_1 = -5°$, $\alpha_2 = 10°$ for the fiber with weak birefringence (for these last fibers exact orientation of the axes of birefringence is difficult to achieve). At this point we note that the case $\alpha_1 = \alpha_2$ is the optimum from the point of view of reducing the zero shift.[1,2] The FRI zero shift in units of degrees per hour is related to the interference phase shift of the counterpropagating waves as follows:[2] $\Delta\Omega = (10^5 \Delta\varphi\lambda c)/(\pi L D)$.

We shall estimate χ in expression (1). Using the results of Refs. 2 and 15, we can show that for $hl_{\mathrm{dep}} \ll 1$ (fiber with strong birefringence) $|\chi| \leqslant \sqrt{hl_{\mathrm{dep}}}$ and for $hl_{\mathrm{dep}} \approx 1$ and $hl_{\mathrm{dep}} \gg 1$ (fiber with weak birefringence) we have $|\chi| \leqslant \pi/4$.

Estimates made using expression (1) yield the following results: 1) for a fiber with strong birefringence, the zero shift is 5×10^{-1} deg/h, and the zero drift 10^{-1} deg/h; 2) for a fiber with weak birefringence (in this case it is impossible to isolate the constant zero shift of the FRI) the zero drift is ≈ 40 deg/h. These estimates were made for an isotropic beam splitter at the entrance to the FRI ring system. If the linear dichroism of this beam splitter is 1–2%, the zero shift and drift in both cases may increase by approximately an order of magnitude. The birefringence of the beam splitter may also substantially increase the zero shift and drift of the FRI. In principle, however, it is always possible to select modulation parameters of the polarization state such that at the entrance to the FRI ring system the polarization states in the different half-periods are mutually orthogonal.

This work was supported by RFBR Grant No. 96-15-96742.

[1] S. M. Kozel, V. N. Listvin, S. V. Shatalin, and R. V. Yushkaĭtis, Opt. Spektrosk. **61**, 1295 (1986) [Opt. Spectrosc. **61**, 814 (1986)].
[2] G. B. Malykin, Izv. Vyssh. Uchebn. Zaved. Radiofiz. **34**, 817 (1991).
[3] G. B. Malykin, Opt. Spektrosk. **83**, 1013 (1997) [Opt. Spectrosc. **83**, 937 (1997)].
[4] G. B. Malykin, I. M. Nefedov, and I. A. Shereshevskiĭ, Izv. Vyssh. Uchebn. Zaved. Radiofiz. **37**, 1473 (1994).
[5] G. B. Malykin and V. I. Pozdnyakova, Opt. Spektrosk. **84**, 145 (1998) [Opt. Spectrosc. **84**, 131 (1998)].
[6] S. Tai, Electron. Lett. **22**, 546 (1986).
[7] É. I. Alekseev and E. N. Bazarov, Kvant. Elektron. (Moscow) **19**, 897 (1992).
[8] G. B. Malykin, V. I. Pozdnyakova, and E. L. Pozdnyakov, Izv. Vyssh. Uchebn. Zaved. Radiofiz. **38**, 1293 (1995).
[9] V. N. Listvin and V. N. Logozinskiĭ, Izv. Vyssh. Uchebn. Zaved. Radiofiz. **34**, 1001 (1991).
[10] G. B. Malykin, Izv. Vyssh. Uchebn. Zaved. Radiofiz. **35**(2), 189 (1992).
[11] G. B. Malykin, Opt. Spektrosk. **75**, 1314 (1993) [Opt. Spectrosc. **75**, 775 (1993)].
[12] G. B. Malykin, I. M. Nefedov, V. I. Pozdnyakova, and I. A. Shereshevskiĭ, Izv. Vyssh. Uchebn. Zaved. Radiofiz. **37**, 1567 (1994).
[13] G. B. Malykin, Opt. Spektrosk. **76**, 540 (1994) [Opt. Spectrosc. **76**, 484 (1994)].
[14] I. A. Andronova, G. V. Gelikonov, and V. M. Gelikonov, Izv. Vyssh. Uchebn. Zaved. Radiofiz. **41**, 1461 (1998).
[15] W. A. Shurcliffe, *Polarized Light* (Harvard Univ. Press, Cambridge, MA, 1962, 207 pp; Mir, Moscow, 1965, 264 pp).
[16] R. A. Bergh, H. C. Lefevre, and H. J. Shaw, Opt. Lett. **6**, 502 (1981).
[17] I. L. Bershteĭn, V. M. Gelikonov, and D. P. Stepanov, Izv. Vyssh. Uchebn. Zaved. Radiofiz. **41**, 1461 (1998).
[18] S. L. Galkin, Opt. Zh. **63**(3), 34 (1996) [J. Opt. Technol. **63**, 209 (1996)].
[19] D. J. Welker, Opt. Lett. **23**, 1826 (1998).
[20] S. M. Jakson, J. Lightwave Technol. **16**, 2016 (1998).
[21] R. U. Liu, Proc. SPIE **2837**, 82 (1996).

Translated by R. M. Durham

Interaction of charged dust particles. Debye quasimolecule

S. I. Yakovlenko

Institute of General Physics, Russian Academy of Sciences, Moscow
(Submitted April 13, 1999)
Pis'ma Zh. Tekh. Fiz. **25**, 83–89 (August 26, 1999)

An analysis is made of an electrically neutral system of two small positive charges surrounded by a common cloud of Boltzmann-distributed electrons. This system, which simulates macroparticle interaction in a dusty plasma, is called a Debye quasimolecule. Calculations are made of the force and potential interaction energy of shielded dust particles as a function of the distance between them. It is shown that the electron shells are polarized so that the forces of attraction of the dust particles in a Debye quasimolecule predominate over the forces of repulsion of their like charges. This may occur up to distances equal to the size of the dust particles. It is concluded that metastable dusty liquids and crystals cannot exist when the electron clouds of the charged particles obey a Boltzmann distribution. © *1999 American Institute of Physics.* [S1063-7850(99)02908-0]

INTRODUCTION

A plasma in which charged micron-sized particles play a significant role (a so-called dusty plasma) is interesting for fundamental and applied research.[1–4] In view of the large charge which may be acquired by finely dispersed particles, a dusty plasma becomes essentially nonideal even at comparatively low particle densities. Plasma-dust crystals, droplets, and clouds may form in such a plasma.

In theoretical analyses of a dusty plasma, particular importance should be attached to studying dust particles surrounded by electron clouds. A dust particle surrounded by an electron cloud is an analog of an atom in the kinetics of gases. The shell of such a dusty atoms may be polarized. It follows from general reasoning that at fairly large distances between like-charged particles (nuclei of dusty atoms) the attractive polarization forces should predominate over the repulsive forces. By analogy with the situation encountered in the interaction of normal atoms, it is natural to assume that at short distances, the forces of repulsion of like-charged dust particles begin to predominate. This should result in the existence of stable dust molecules and also liquid and crystalline structures of dust particles surrounded by electron clouds.

Quite clearly, the switch from attraction to repulsion at distances of the order of the Debye length is observed experimentally. Otherwise, dusty structures could not form. However, it is shown in the present study that if the electron distribution in a cloud surrounding dust particles is in thermodynamic equilibrium, the dust particles can only attract. From this it follows that the existence of real dusty structures is caused by the nonequilibrium state of their electron clouds.

A charge surrounded by a cloud of electrons having a Boltzmann distribution was previously described by us as a Debye atom,[5] as opposed to a Thomas–Fermi atom in which the electrons are degenerate. Here we consider a system of two charges surrounded by a common cloud of Boltzmann-distributed electrons. This system could be logically called a diatomic Debye molecule. However, it has been shown that this system is unstable. In atomic physics and atomic collision theory the term quasimolecule is used in these cases. Thus we shall call these dust particles in a cloud of Boltzmann-distributed electrons a Debye quasimolecule.

INITIAL EQUATIONS

The potential φ and field strength E in a Debye atom and a Debye quasimolecule are described by the Poisson equation and the Boltzmann distribution for the electrons $N_e = N_{e0}\exp(\varphi)$. The initial equations then have the form:

$$(\nabla \mathbf{E}) = -\exp(\varphi), \quad \mathbf{E} = -\nabla\varphi, \tag{1}$$

where ∇ is the Hamiltonian vector operator.

Here we use dimensionless quantities: the length is measured in Debye radii $r_D = (T_e/4\pi e^2 N_{e0})^{1/2}$, where N_{e0} is the free electron density in the absence of an external field, e is the electron charge, T_e is the electron temperature, the potential is measured in units of T_e/e, and the field strength is measured in T_e/er_D.

On the basis of the experimental conditions[3] where $N_{e0} = 2.5\times 10^{10}\,\mathrm{cm}^{-3}$, $T_e = 0.146\,\mathrm{eV} = 1700\,\mathrm{K}$, we have for the characteristic values: $r_D = 0.002\,\mathrm{cm}$, $T_e/e = 0.146\,\mathrm{V}$, $T_e/er_D = 80\,\mathrm{V/cm}$. For a dust particle of average radius $r_0 = 0.4\,\mu\mathrm{m}$ ($r_0/r_D = 0.02$) and charge $Z_p e = 500e$ we have the field strength at the particle surface $E_0 = Z_p e/r_0^2 = 4.5\times 10^4\,\mathrm{V/cm}$ ($E_0 e r_D/T_e = 550$).

From the formal point of view, the analysis of a Debye molecule and a Debye quasimolecule only differ in terms of the geometry of the problem. Assuming a spherically symmetric electron cloud, a Debye atom[5] was successfully analyzed by solving the one-dimensional Poisson equation (1). In order to analyze a Debye quasimolecule, we shall assume that the problem is symmetric relative to the z axis connecting the nuclei. It is then sufficient to analyze the two-dimensional equation (1).

We also note that the main aim of analyzing the Debye molecule is to find the dependence of the resultant electrostatic force acting on the dust particles on the distance between them.

METHOD OF SOLUTION

The two-dimensional Poisson equation (1) was solved using the POTENTsIAL program package, developed for laser isotope separation[6,7] to model the extraction of ions from a plasma via the electrode system (see also Ref. 8). In particular, these programs calculate the spatial distribution of the potential φ, the electron density N_e, and the electric field **E** for given positions and potentials of arbitrarily distributed conducting electrodes of rectangular cross section. The Poisson equation is solved by a method of iteration in a form similar to that described in Ref. 9. For the analysis of a Debye molecule, the program package was modified so that the Poisson equation could be solved not only in planar but also in cylindrical geometry.

For the analysis of a Debye molecule the charged dust particles were simulated by small cylindrical conducting electrodes. The boundary conditions were set by the potential φ_0 at these cylinders. In addition, zero potential was at a surface some distance from the electrodes simulating the dust particles.

After determining the spatial distribution of the potential and the field, the results were processed using Mathcad. The aim of this processing was to find the charge at the electrode Z_p and the electrostatic force $F(d)$ acting on the electrode, where d is the distance between the centers of the electrodes. The potential interaction energy of the electrodes (i.e., the term of the Debye quasimolecule) was determined by integrating over $U(d)=\int_d^\infty F(x)dx$. The electrode charge was calculated using the Gauss theorem, as the vector of the field intensity flux across the electrode surface. The force of the electric field acting on the electrode was determined by integrating the electric pressure $E^2/8\pi$ on the surface of the conductor.

RESULTS

A cylindrical region of radius $4r_D$ and $8r_D$ was specifically analyzed in the calculations discussed below. The diameter and height of the electrodes simulating the dust particles were taken to be equal to some value r_0, where r_0 was fairly small $r_D/r_0=50$. The distance between the electrodes was varied in the range $d=2r_0-1.5r_D$. The results of the calculations are given for large electrode charges $Z_p \gg 10$.

The distribution of the potential φ and the electron density $n_e \equiv \exp(\varphi)$ have a form which can be guessed qualitatively beforehand. The electrons are concentrated at the surface of the electrodes, to a considerable extent shielding their charge. However, a significant fraction of the electrons builds up at the center of the axis of the Debye quasimolecule. This is responsible for the effective attraction of the dust-particle nuclei. It is found that attraction occurs over the entire range of states considered.

The calculations showed that the electrode charges Z_p are proportional to the potential φ_0 at them and the total force acting on the electrode from the other electrode and the electron cloud is proportional to the square of the voltage and thus the charge: $F(r)\propto\varphi_0^2\propto Z_p^2$. This allowed the force and the interaction energy of the nuclei to be expressed in terms of certain universal functions:

$$F(d)=f(d/r_D)(Z_p e/r_D)^2, \quad U(D)=u(d/r_D)(Z_p^2 e^2/r_D).$$

The universal functions $f(x)$ and $u(x)$ are plotted in Fig. 1. The factors $(Z_p e/r_D)^2$ and $Z_p^2 e^2/r_D$ determine the force and potential interaction energy of the point defects at a distance equal to the Debye length.

CONCLUSIONS

The results of tabulating the force and the interaction energy of dust particles in a Debye quasimolecule are universal for fairly large distances between them: $d>5r_0$. For shorter distances, the results depend on the specific shape of the electrodes. In addition, at short distances the polarization of the charge at the electrode becomes substantial. However, we are specifically interested in large distances between the nuclei $d \gg 2r_0$, which are found in the experimentally observed dusty structures.

The results of the calculations indicate that at least for distances substantially larger than the sizes of the dust particles, attractive forces predominate. This has a logical explanation. The electron density of a Debye atom increases abruptly on approaching its nucleus (for further details see Ref. 5). Thus, as the nuclei come closer, an increasing number of electrons accumulate at the center of the molecule. The force of attraction of the nuclei to these electrons accumulated on the axis of the molecule predominates over the Coulomb repulsion force of the nuclei. Note that this fundamentally distinguishes a Debye quasimolecule from an ordinary molecule in which the electron motion is described by quantum laws rather than by classical ones. This is because by virtue of the quantum-mechanical uncertainty principle, the electron density in real atoms does not increase without bound near an atomic nucleus. In particular, if we use a Thomas-Fermi electron distribution rather than a Boltzmann one, the forces of attraction at short distances between the nuclei are replaced by forces of repulsion.

Estimates show that in dusty structures the quantum-mechanical effects for the electrons are very weak. Hence under equilibrium conditions, dusty structures would not be stable. As a result of the collision between two Debye atoms with an impact distance shorter than the Debye length, these atoms should undergo mutual trapping followed by spiral motion until the nuclei collide. In atomic collision theory this effect is known as orbiting. Thus, the characteristic decay time of a dusty plasma consisting of Debye atoms would be $\tau=(\pi r_D^2 v_p N_p)^{-1}$, where v_p and N_p are the characteristic velocity and density of the dust particles. Under the experimental conditions[3] we have $m_p\sim 2\times 10^{-12}$ g, $v_p \sim (2T_e/m_p)^{1/2}\sim 0.5$ cm/s, and $N_p\sim 5\times 10^{-7}\text{cm}^{-3}$, from which it follows that $\tau\sim 4\times 10^{-3}$ s.

Since in practice dust droplets and crystals are long-lived, it must be assumed that the electron clouds around the dust particles in these experiments do not obey a Boltzmann

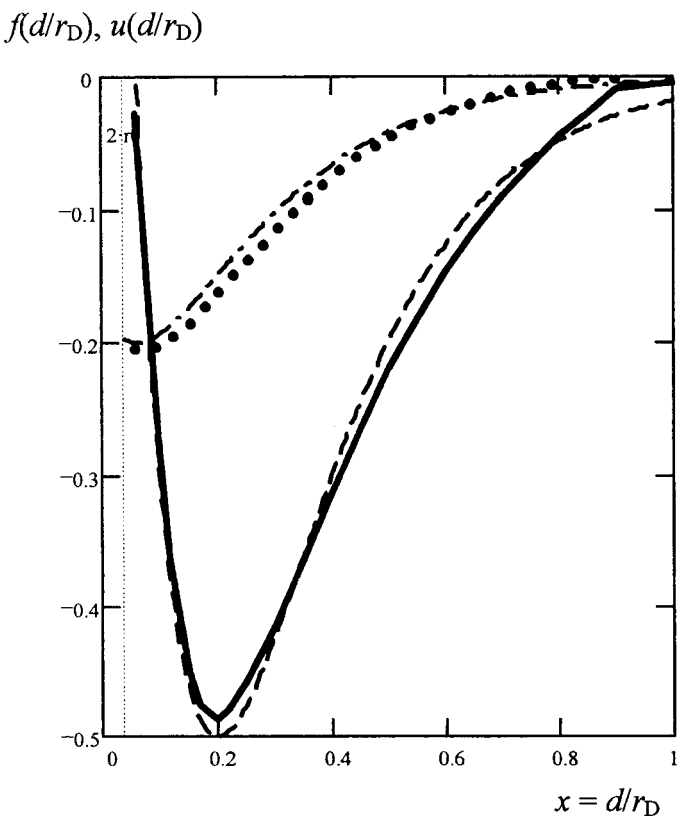

FIG. 1. Universal functions characterizing the dependence of the force (solid curve) and the potential energy (dashed curve) of the interaction between the nuclei of a Debye quasimolecule as a function of the distance between them $x=d/r_D$. The dotted curve corresponds to the function $0.5[\exp(-10\cdot(x-0.2))-2\exp(-5\cdot(x-0.2))]$, which approximates this force. The dot-dash curve corresponds to the function $0.05[\exp(-10\cdot(x-0.2)) \quad -4\cdot\exp(-5\cdot(x-0.2))]$, which approximates the potential energy (term).

distribution, i.e., the electrons are thermodynamically nonequilibrium. In other words, there must be anomalously few electrons having a high absolute negative energy. Note that this behavior is obtained for the metastable distribution obtained by modeling the dynamics of many Coulomb particles.[5,10–12]

The authors thank Yu. I. Syts'ko for modifying the POTENTsIAL program package.

[1] V. E. Fortov and I. T. Yakubov, *Nonideal Plasmas* [in Russian] (Énergoatomizdat, Moscow, 1994).
[2] N. N. Tsytovich, Usp. Fiz. Nauk **167**(1), 57 (1997).
[3] V. E. Fortov, A. P. Nefedov, O. F. Petrov, A. A. Samaryan, and A. V. Chernyshev, Zh. Éksp. Teor. Fiz. **111**, 467 (1997) [JETP **84**, 256 (1997)].
[4] V. E. Fortov, V. S. Filinov, A. P. Nefedov, O. F. Petrov, A. A. Samaryan, and A. M. Lipaev, Zh. Éksp. Teor. Fiz. **111**, 889 (1997) [JETP **84**, 489 (1997)].
[5] A. N. Tkachev and S. I. Yakovlenko, Preprint No. 8 [in Russian] (IOFAN, 1997), 20 pp.; Zh. Tekh. Fiz. **69**(1), 53 (1999) [Tech. Phys. **44**, 48 (1999)].
[6] R. I. Golyatina, Yu. I. Syts'ko, and S. I. Yakovlenko, Kratk. Soobshch. Fiz. No. 7, 3 (1997).
[7] R. I. Golyatina, Yu. I. Syts'ko, and S. I. Yakovlenko, Laser Phys. No. 4, 860 (1998).
[8] S. I. Yakovlenko, Kvantovaya Élektron. (Moscow) **25**, 971 (1998); Laser Part. Beams No. 4, 541 (1998).
[9] Yu. I. Syts'ko and S. I. Yakovlenko, Laser Phys. **6**, 989 (1996).
[10] S. A. Maĭorov, A. N. Tkachev, and S. I. Yakovlenko, Usp. Fiz. Nauk **164**(3), 297 (1994).
[11] S. A. Mayorov, A. N. Tkachev, and S. I. Yakovlenko, Physica Scripta **51**, 498 (1995).
[12] A. N. Tkachev and S. I. Yakovlenko, Izv. Vyssh. Uchebn. Zaved. Fiz. **41**(1), 47 (1998).

Translated by R. M. Durham

Isolated concentration waves of point defects under pulsed laser irradiation

F. Mirzoev and L. A. Shelepin

P. N. Lebedev Physics Institute, Russian Academy of Sciences, Moscow
Institute of Problems of Laser and Information Technologies, Russian Academy of Sciences, Moscow
(Submitted April 13, 1999)
Pis'ma Zh. Tekh. Fiz. **25**, 90–94 (August 26, 1999)

A model is proposed for the first time for the propagation of an isolated (soliton-like) concentration wave of point defects in a crystal exposed to laser pulses. It is shown that this isolated concentration wave is formed as a result of a nonlinear concentration dependence of the defect source function which is caused by a reduction in the activation energy for defect formation near clusters when the elastic stress field is taken into account. Conditions for the excitation of an isolated concentration wave, its profile, and propagation velocity are determined. © *1999 American Institute of Physics.* [S1063-7850(99)03008-6]

We know that the action of high-power laser pulses on a solid may lead to the generation of point defects (vacancies and interstitial sites) whose density is considerably higher than the thermodynamic equilibrium level. It was shown in Refs. 1–4 that under certain critical conditions, the point defect concentration may undergo complex dynamic changes which result in various types of self-organization of localized structures: point-defect clusters or point-defect density superlattices (and also static deformation of the lattice). In an ensemble of defects with fairly high density, as a result of the nonlinear concentration (s-shaped) dependence of the point-defect generation function from crystal-lattice sites, it may be possible to observe the propagation of a defect-density switching wave which transfers the system from a state having some minimum density $n_{\min}$ to a state having a maximum density $n_{\max}$ (Refs. 3 and 4). Concepts of the bistable behavior of a point-defect system have been used to interpret the phase transition from the crystalline to the amorphous state under the action of laser pulses which do not cause melting of the lattice (solid-state amorphization).[3,4]

In the present paper we propose a model for the excitation of isolated concentration waves of point defects in a crystal initially containing point-defect clusters. Critical conditions for the excitation of a density wave are determined and its profile and propagation velocity are estimated.

We shall make a theoretical analysis of the excitation of an isolated concentration wave, using a nonlinear system of equations which describes the joint dynamics of point defects and clusters. Assuming that the main processes controlling the time behavior of the defect density are generation, diffusion, and recombination, we have in the one-dimensional case (for simplicity):

$$\frac{\partial n}{\partial t}=\mu\alpha Rn-\frac{n}{\tau}+D\frac{\partial^2 n}{\partial x^2}. \tag{1}$$

In Eq. (1) the first term allows for the strain-stimulated generation of point defects by spherical clusters, where R is the cluster radius, $\mu=4\pi N_0\Omega_0^{-1}$, N_0 is the cluster density, Ω_0 is the atomic volume, $\alpha=K\Omega^2 D/kT$, K is the elastic modulus, Ω is the activation volume for point-defect formation, D is the diffusion coefficient of the point defects, k is the Boltzmann constant, and T is the temperature. The second term describes recombination at centers (recombination velocity: $\beta=\beta_0\exp(-W/kT)=\tau^{-1}$, $\beta_0=\rho\nu d_0^2$, τ is the point defect lifetime, ρ is the density of recombination centers, ν is the Debye frequency, d_0 is the lattice period, and W is the activation energy for defect diffusion) and the third term describes their spatial diffusion.

The equation describing the dynamics of the time variation of the cluster sizes as they undergo ''deformation evaporation'' is given in the form:

$$\frac{\partial R}{\partial t}=-\frac{\alpha n}{R}+D_R\frac{\partial^2 R}{\partial x^2}, \tag{2}$$

where D_R is the cluster diffusion coefficient. Since $D_R \ll D$, we shall subsequently neglect the mobility of the clusters.

Converting in Eqs. (1) and (2) to the self-similar variable $\xi=x+\nu t$, we obtain

$$\nu\frac{\partial R}{\partial \xi}=-\frac{\alpha n}{R}, \tag{3}$$

$$\nu\frac{\partial n}{\partial \xi}-D\frac{\partial^2 n}{\partial \xi^2}=\mu\alpha Rn-\beta n. \tag{4}$$

Integrating Eq. (4) and introducing the function $\eta(\xi)=\int_{-\infty}^{\xi} n\,d\xi$, we obtain:

$$\nu\frac{\partial \eta}{\partial \xi}-D\frac{\partial^2 \eta}{\partial \xi^2}=\mu\alpha\int_{-\infty}^{\xi} R(\xi)n(\xi)\,d\xi-\beta\eta. \tag{5}$$

From Eq. (3) we have

$$\alpha\int_{-\infty}^{\xi} Rn\,d\xi=\frac{\nu}{3}[R^3(-\infty)-R^3(\xi)]=\frac{\nu}{3}[R_0^3-R^3(\xi)]. \tag{6}$$

Substituting Eq. (6) into Eq. (5) gives

$$\nu\frac{\partial\eta}{\partial\xi}=D\frac{\partial^2\eta}{\partial\xi^2}+\varphi(R,\eta), \tag{7}$$

where $\varphi(R,\eta)=\mu\nu(R_0^3-R^3(\xi))-\beta\eta$.

For the derivative φ'_η we have $\varphi'_\eta=3\mu\alpha R-\beta$. Quite clearly we have $\varphi'_\eta(0)=3\mu\alpha R_0-\beta>0$, if $\alpha R_0>\beta/3\mu$. Bearing in mind that the function $R(\eta,\nu,R_0)$ decreases with increasing η, we have $\varphi'_\eta(\eta)<\varphi'_\eta(0)$. From this it follows that there is a single value $\eta_*>0$ such that $\varphi(\eta_*)=0$.

Thus, we have reduced the problem (1) and (2) to the Kolmogorov–Petrovskiĭ–Piskunov problem.[5] By analogy with this problem, we can confirm that in the system of clusters and point defects, a wave may be excited whose velocity has the lower limit

$$\nu_0=2\sqrt{D(3\mu\alpha R_0-\beta)}. \tag{8}$$

Since $d\eta/d\xi=n(\xi)$ and for $\xi\to\mp\infty$ $d\eta/d\xi\to0$, the point-defect density wave is an isolated (soliton-like) wave propagating at the minimum velocity (8).

It follows from formula (8) that $3\mu\alpha R_0>\beta$. Thus, in order for an isolated defect concentration wave to be excited in the crystal, the initial cluster size must exceed some critical level: $R_0>R_*$, where $R_*=\beta/3\mu\alpha$.

We shall now determine the profile of the isolated concentration wave. From Eq. (3) we have $R^2=R_0^2-2\alpha\eta/\nu$. We then express $R(\eta)$ in the form of an expansion $R\approx R_0-\alpha\eta/\nu R_0+\ldots$ and substitute into Eq. (7). Retaining terms of the order of α^2, we obtain the following wave equation:

$$\nu\frac{d\psi}{d\xi}=D\frac{d^2\psi}{d\xi^2}+\mu\alpha(R_0-R_*)\psi(1-\psi),$$

where $\psi=\alpha\eta/\nu R_0(R_0-R_*)$.

The exact solution of this equation has the form:

$$\psi(\xi)=[1+(\sqrt{2}-1)\exp(-\xi/\delta)]^{-2}. \tag{9}$$

Returning to the variable $n(\xi)$, we finally obtain for the profile of the isolated concentration wave

$$n(\xi)=A\exp(-\xi/\delta)[1+(\sqrt{2}-1)\exp(-\xi/\delta)]^{-3}, \tag{10}$$

where $A=20\pi(\sqrt{2}-1)(N_0R_0^3/d_0^3)(1-R_*/R_0)^2$ and $\delta=\sqrt{6D/\mu\alpha(R_0-R_*)}$ is the width of the isolated concentration wave. Quite clearly we have $n(\xi)\to0$ for $\xi\to\mp\infty$.

For the velocity corresponding to the wave equation (10), we obtain:

$$\nu=5\sqrt{\mu\alpha(R_0-R_*)D/2}. \tag{11}$$

It follows from Eqs. (7) and (11) that $\nu=\nu_0(1+\Delta)$, $\Delta\ll1$. This confirms that formula (10) satisfactorily describes the profile of the isolated concentration wave.

On analyzing formulas (10) and (11), we note that the conditions for the formation of an isolated defect concentration wave, its profile, and propagation velocity depend strongly on the initial cluster sizes. When the initial cluster radius is larger, the defect density wave propagates at a higher velocity and has a steeper maximum than a wave propagating in a medium with a smaller initial cluster radius.

In conclusion, we note that an isolated concentration wave can also propagate in the model

$$\frac{\partial R}{\partial t}=-F(R,M)n+D_R\frac{\partial^2R}{\partial x^2},$$

$$\frac{\partial n}{\partial t}=S(R)F(R,M)n-\frac{n}{\tau}+D\frac{\partial^2n}{\partial x^2},$$

which is a generalization of the model (1) and (2).

Here $F(R,M)$ is a monotonic function of R, $\{M\}$ is a set of parameters characterizing the medium, and $S(R)$ is the cluster surface area.

It has thus been shown that isolated concentration waves of point defects can propagate in a system of point defects and clusters described by Eqs. (1) and (2). The phenomenon is a threshold process and takes place when the initial cluster size in the irradiated crystal exceeds a certain critical value which is determined by the density of recombination centers, the elastic modulus, the dilatational volume of the point defects, and the temperature of the medium. For values of the parameters typical of vacancy-type point defects $kT=0.04$ eV, $D=10^{-6}\,\mathrm{cm^2\cdot s^{-1}}$, $K\Omega=5$ eV, $N_0=10^{14}\,\mathrm{cm^{-3}}$, and $\rho=10^{10}\,\mathrm{cm^{-2}}$, the critical cluster radius and the wave propagation velocity are $R_*=3\times10^{-7}$ cm and $\nu=0.6$ cm/s, respectively. The quantitative conclusions of the present study can be used to plan experiments on controlling the defect buildup process in materials exposed to high-intensity laser irradiation.

[1] V. I. Boĭko, B. S. Luk'yanchuk, and E. Tsarev, Tr. IOFAN. **30**, 6 (1991).
[2] F. Kh. Mirzoev, V. Ya. Panchenko, and L. A. Shelepin, Usp. Fiz. Nauk **165**(1), 3 (1996).
[3] F. Kh. Mirzoev and L. A. Shelepin, Pis'ma Zh. Tekh. Fiz. **22**(13), 28 (1996) [Tech. Phys. Lett. **22**, 531 (1996)].
[4] F. Kh. Mirzoev, Zh. Tekh. Fiz. **68**(8), 73 (1998) [Tech. Phys. **43**, 943 (1998)].
[5] A. N. Kolmogorov, I. G. Petrovskiĭ, and N. S. Piskunov, Byul. Mosk. Gos. Univ. Ser. Mat. Mekh. **1**(6), 1 (1937).

Translated by R. M. Durham